Durham E-Theses

Image sharpening metrics and search strategies for indirect adaptive optics

Doble, Nathan

How to cite:

Doble, Nathan (2000) *Image sharpening metrics and search strategies for indirect adaptive optics*, Durham theses, Durham University. Available at Durham E-Theses Online: http://etheses.dur.ac.uk/4359/

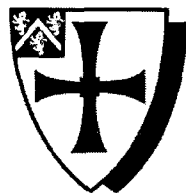# Image Sharpening Metrics and Search Strategies for Indirect Adaptive Optics

by

Nathan Doble M.Sci. M.Sc.

A Thesis Submitted to the University of Durham for the
Degree of Doctor of Philosophy.

May 2000
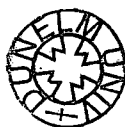
1 4 NOV 2000

Preface

The author declares that the work reported in this thesis has not been submitted previously for a degree to Durham or any other university. Unless otherwise explicitly indicated the work is the authors own. It is acknowledged that the development and design of ELECTRA system formed no part of the author's work.

The work with the ELECTRA system has been published in the following proceedings:

- N. P. Doble, D. F. Buscher, G. D. Love, R. M. Myers, Correction of non-common path errors in an adaptive optics system. In Proc. of the 2nd International Workshop on Adaptive Optics for Industry and Medicine. World Scientific Publishing. Editor G. D. Love. July 1999.

- N. P. Doble, G. D. Love, D. F. Buscher, R. M. Myers and A. Purvis, Use of image quality metrics for correction of non-common path errors in the ELECTRA adaptive optics system. In Proc. SPIE Vol. 3749, p. 785-786, 18th Congress of the International Commission for Optics, Editors: A. J. Glass, J. W. Goodman, M. Chang, A. H. Guenther; T. Asakura. August 1999.

Abstract

Adaptive optics is concerned with the correction of turbulence induced aberrations and mis-alignments in optical systems. It is an expensive and complicated technology which has been developed for astronomy and defence applications. Recently, it has found a role within industry and medicine. This thesis deals with a simplified mechanism for adaptive feedback based on the analysis of distorted images, and an iterative feedback process. Simplification is achieved at the expense of speed, but there are particular applications where this technique is suitable. The one considered here is the removal of so-called non-common path errors in a traditional adaptive optics system, which can otherwise degrade the system performance.

Acknowledgements

Contents

List of Tables

List of Figures

Chapter 1

Introduction

Adaptive optics (AO) is a technique used to ameliorate aberrations in optical systems. The technology was developed primarily for the removal of aberrations induced by atmospheric turbulence, which affects both the resolution of ground based astronomical telescopes, and the propagation of laser beams through the atmosphere. Adaptive optics began to be developed in the 1970s, mainly by the United States Airforce (USAF), and then later by the astronomical community. It was only towards the end of the 1990s that the technology began to mature, and most large astronomical telescopes now incorporate some kind of adaptive optics system. Nevertheless, adaptive optics is still an expensive and complicated technology.

An AO system contains the three classic components of any feedback system, *viz.* a controller (usually a deformable mirror), an error sensor (called a wavefront sensor, WFS), and a feedback/control loop. There is then an output channel which normally contains the camera where the final corrected image is formed. The work presented here describes a simplified feedback mechanism based on indirect adaptive optics. The wavefront sensor is omitted, and the distorted image is analysed to give a measure of the 'quality' of the image, i.e. its freedom from aberrations, or otherwise. The wavefront controller is then modified, in a quasi-random fashion, to produce a new distorted image, which is then analysed to determine if the image quality has increased or not. The measure of the image quality is called an 'Image Metric' or 'Merit Function', and the space of possible corrections is then searched to find the optimum. Hence the title of this thesis.

The technique described, which although unlikely to find use as the main corrective scheme in atmospheric AO does lend itself to certain applications. The first of these is the use of AO in industrial and medical applications. These include correction of aberrations in high power lasers and high resolution imaging of the human retina. Many of these applications have timescales which are longer than
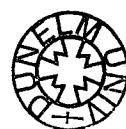
those of atmospheric turbulence and so image sharpening may be an attractive technology.

The application investigated in this thesis is the correction of non-common path errors (NCPE) in a conventional AO system. Usually a plane wavefront is fed into an AO system in order to calibrate the WFS. Such a method will not correct any system errors present both before and in the output channel. This thesis proposes a method whereby it is the image at the science camera that is optimised and the subsequent WFS settings are then taken to be the null position. In such a role, the method described is an 'AO system within an AO system' and has been installed on the ELECTRA instrument[1] at University of Durham.

The use of image sharpening metrics is not new, indeed some of the first published work on AO incorporated a similar technique. However, image sharpening has generally been ignored by the AO community. Only recently has it been rekindled and this is due to several reasons; the realisation that NCPE in AO systems are important and the development of genetic algorithms are two such reasons. The research described in this thesis contains the following novel results:

1. An analysis of wavefront correction using a variety of image quality metrics and search algorithms is presented, using both simulation and experimental results.

2. A simple, low cost adaptive optics system based on a liquid crystal spatial light modulator (LC-SLM) is described.

3. A non-common path corrector which has been incorporated into the ELEC-TRA AO system is presented.

Adaptive and active optics

Before proceeding it is necessary to differentiate between two common terms used within the AO community. The term *adaptive optics* is used when talking about the temporal aberrations caused by the Earth's atmosphere, and generally has a bandwidth in the KiloHertz region. *Active optics* on the otherhand has a much slower timescale (of the order of a few Hertz or less). Such active errors arise due to the gravitational, thermal and mechanical stresses on large telescope structures and subsystems and occasionally do not lend themselves to conventional adaptive correction techniques.

---

[1] Described in detail in Chapter 6

Throughout this thesis both terms are classed together under the heading adaptive optics. The actual regime will be apparent from the temporal aspects of the aberration when the situation is described.

1.1 Direct and indirect adaptive optics

As the field of AO has progressed, different techniques have been investigated to achieve the final goal of a diffraction limited image. Two broad classifications of methods [2] have been generally accepted and are shown in Fig. 1.1.

- *Direct* techniques use measures of the wavefront such as the phase, tilt or curvature and generally reconstruct the incident wavefront. These are the basis for virtually all the AO systems used on the World's telescopes.

- *Indirect* schemes never directly measure wavefront properties but use information related to it to provide the signal to the corrective element without reconstruction. Indirect methods usually incorporate more novel schemes such as non-linear optics. The image sharpening technique used in this work is an example of an indirect method.

(a) Direct wavefront tilt AO

(b) Indirect AO using intensity measurement
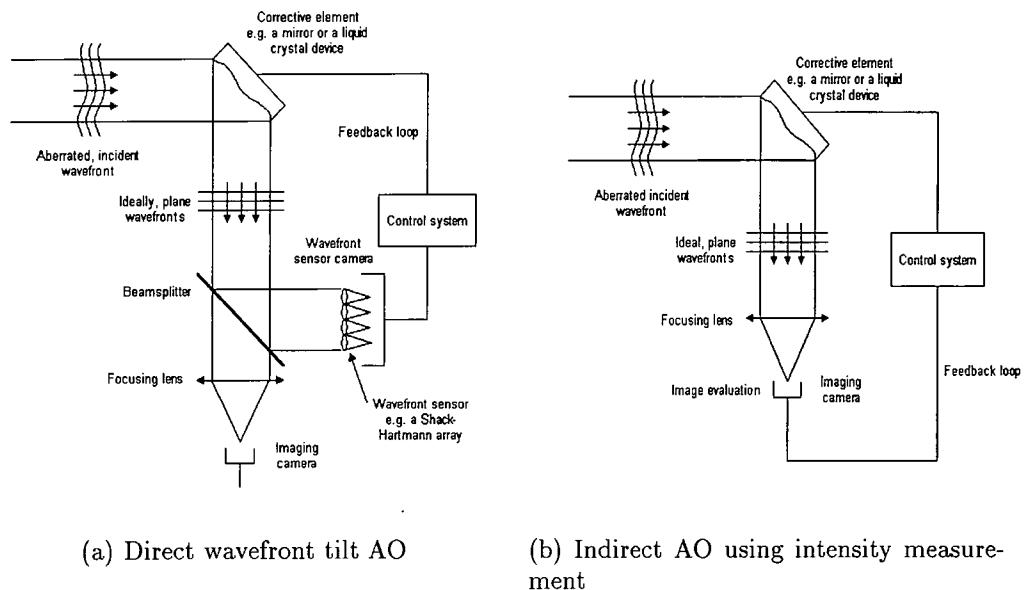
Figure 1.1: Basic Direct and Indirect AO arrangements.

One benefit of using an intensity scheme such as image sharpening should be readily apparent, namely the lack of non-common paths as compared to the direct

---

[2]Some authors define an AO system as direct only if the actual phase map is calculated in the feedback process. The term is used slightly more generally here.

case. It is this property that is exploited in later chapters. A drawback to such a technique however, is that the characterisation of the exact phase correction needed for the wavefront corrector is impossible as this information has been irretrievably lost in forming the image. Several measurements are therefore needed to drive the correcting element to the conjugate state. One of the reasons why it is not used in atmospheric correction methods is due to this inherent decrease in bandwidth. Methods by which the correction is measured and the physics of the device used to provide the correction are wide ranging. Various schemes are described briefly in Chapter 2.

1.2 Project aims

This thesis is concerned with the implementation of an AO system using intensity measurement through the use of 'image sharpening and image metrics'. The ideas are developed and the results presented in the following way:

- Chapter 2 describes the general principles behind AO, namely wavefront sensing and details of corrective devices. AO systems in use on the World's telescopes are briefly detailed and schemes to correct quasi-static telescope aberrations are included.

- Chapter 3 details the relevant diffraction theory. Using these equations the ideas and history of image sharpening metrics are introduced.

- Chapter 4 discusses various strategies for searching large correction spaces when using image sharpening. The use of such algorithms was required when working with the ELECTRA system.

- Chapter 5 contains both the theoretical and experimental results of using a pixelated LC-SLM to correct for static aberrations. System performance with both point and extended sources is detailed.

- Chapter 6 details the theoretical results of various search algorithms using a simulated mirror array. The problem of NCPE is explained.

- Chapter 7 describes the system improvement when the NCPE in the ELECTRA system is corrected. Improvement was observed for both monochromatic and white light sources.

- Chapter 8 summarises the work and talks about future possible investigations and implementation of image sharpening metrics for other applications.

Chapter 2

Adaptive/active optics

2.1 Introduction and brief history

This chapter details some of the concepts and principles behind adaptive optics. It is not meant to be exhaustive and the reader is directed to the references for further details. Its purpose is to provide a link to some of the concepts detailed in later chapters.

AO was first developed as a means of overcoming the image degradation observed when viewing stellar images through the Earth's atmosphere. A way to circumvent this is to launch telescopes into space and indeed this has been achieved with the Hubble Space Telescope (HST). An obvious drawback is the enormous cost involved and the general limit on the size of the telescope aperture. The use of active, folding, lightweight mirrors [1, 2] may go some way to overcoming this limitation.

Another solution to the problem of atmospheric turbulence is to provide a correction which varies with the same spatial and temporal characteristics as the atmosphere. A simple calculation shows the potential benefit to ground based astronomy if this could be realised. The resolution, $\Delta\theta$ of a telescope with diameter D at a wavelength λ is given by

$$\Delta\theta = \frac{1.22\lambda}{D} \quad (x206265) \quad \text{arcsecs.} \quad (2.1)$$

For a terrestrial telescope e.g. the Keck telescope with D=10m, λ=0.55μm would have a diffraction limited resolution of $\Delta\theta$=0.014 arcsecs. The HST with a mirror diameter of 2.4m has $\Delta\theta$=0.057 arcsecs. As can be seen there is a potential improvement by a factor of 4. If the effects of the atmosphere are now included the effective diameter, D is reduced to 0.1-0.2m. Applying the same calculation results in a resolution of 1.38 arcsecs hence there is a potential gain of a factor

100 if AO can be implemented. For infrared wavelengths the improvement is less than 20 and is easier to achieve with current AO systems.

To achieve this improvement in the visible requires system bandwidths of the order of a KHz and places a huge burden on the controlling electronics and the correction technology. As alluded to in the introduction, the available technology can be the limiting factor.

Basic system requirements

An AO system can be broken down into three subsystems namely:

- A means of measuring the aberrations i.e. wavefront sensing.

- An element to provide the correction usually in the form of a deformable mirror.

- A control system to interface the above.

How these are realised has been the focus of ongoing research over the past 30 years. Although the idea was first proposed as far back as 1953 by Babcock [3], Labeyrie's paper [4] in 1970 on speckle interferometry was the first to provide a means of overcoming the effects of refractive index variations in the Earth's atmosphere.

2.2 Causes of image degradation

There are several factors which lead to the broadening of an image beyond the diffraction limit of the telescope. The design and location of the telescope are key in trying to reduce their influence.

1) *Atmospheric turbulence or 'seeing'*

Tatarski [5] then Kolmogorov [6] derived a model whereby the phase changes caused by thermal effects in the air could be described. These fluctuations give rise to turbulent eddies which have a finite dimension. The size of these eddies range from a few millimeters to several metres, although these are still open to debate. The scale of these eddies decreases with height above sea level. The atmosphere can then be thought of as a series of layers each having a characteristic eddy scale. Fried [7] was the first to define a single number denoted by r_0, which

characterised the turbulence. Generally speaking, good sites will have a value in the region of 10$< r_0 <$20cm and are found on the top of mountains.

In other words, for large aperture telescopes the effect of 'seeing' is to restrict their resolution to that of a diffraction limited telescope of diameter r_0. The term D in Eq. 2.1 being replaced by r_0.

2) *Dome seeing*

The location of the telescope is also important. Smooth laminar flow of air is broken by groundbased objects, another reason for locating telescopes on the top of mountains (there is also a reduction in the light contamination).

The actual thermodynamics of the dome is another critical factor. Unless the air in the dome is in equilibrium with the air outside thermal eddies will be induced. Another requirement is to keep the mirror temperatures the same as the surrounding air. The hole in the primary is of particular concern as this can give rise to a plume of warmer air. The use of an AO system induces another problem namely, the heating effect due to the power supplies for the mirror actuators.

3) *Optical alignment*

Large aperture telescopes are generally heavy instruments and hence are subject to gravitational and mechanical stresses. On the Hobby-Eberly and Keck telescopes a segmented primary is used to provide active correction. This is discussed further in Section 2.5.

AO systems themselves are complex optical instruments consisting of numerous components which require alignment. This is the main thrust of the work described in Chapters 5, 6, 7 and will be discussed in due course.

Other sources of error lie in the telescope drive mechanics and wind buffeting [8] of the telescope itself and are usually taken out by the use of a fast tracking mirror operating in the 10Hz regime.

2.3   Adaptive wavefront sensing and correction techniques

This part attempts to describe some of the methods employed for wavefront sensing and the devices used to provide the correction. In no way is this exhaustive and the reader is directed to the monographs by Tyson [9, 10].

For the conjugate correction to be applied the form of the aberration present must be measured. The means by which this is determined and the type of

corrective device are closely linked. For example, if the wavefront curvature is measured then the special form of the output signal would imply use of a membrane or bimorph mirror (this is elaborated on later). The main methods by which the system aberrations are sensed and the means of correction are detailed in the following subsections.

2.3.1 Direct Wavefront Sensing

A wavefront sensor (WFS) measures the system aberrations in the exit pupil. With astronomy, light fluences are very low and one does not want a wavefront sensor which is photon intensive. From Fig. 1.1.a, the incoming wavefront in a direct scheme is split into two paths, one to the wavefront sensor, the other to the science camera. This division is very delicate and one wants to use the minimum number of photons for the WFS allowing for the observations of fainter objects. For the indirect case Fig. 1.1.b, all the available photons are used as a measure of the image itself is used to provide the correction signal. For a comparison of WFS techniques the reader is directed to Geary [11].

One of the first WFS methods employed was that of interferometry. Hardy [12] used a shearing interferometer in conjunction with a 21 actuator mirror for astronomical AO. Whenever two coherent wavefronts combine an interferogram will be formed, the fringes indicate areas of constant optical path difference (OPD = nd where n is the refractive index and d is the distance) i.e. an integer number of wavelengths, $m\lambda$.

Shearing interferometry

Several variations exist all have the advantage in that they are self-referencing. The differences lie in the way the shear is produced.

- *Lateral* [9] - If in a Mach-Zehnder arrangement, one of the mirrors is tilted then one of the beams will be laterally shifted and the recombined beams do not fully overlap. Interference fringes will be formed in the region of overlap. The fringes are directly proportional to the wavefront tilt.

- *Rotational* [13] - This involves rotating one of the beams through 180^0 and then recombining.

- *Radial* [9] - Again a Mach-Zehnder arrangement is used. In one of the arms the wavefront is minified and in the other it is magnified. The expanded beam is taken to be the reference over the diameter of the compressed beam.

On recombination interference fringes will be observed over the area of the minified beam.

The Smartt Point Diffraction Interferometer (PDI)

The PDI is not widely used in the astronomical community due to its high light loss although Birch *et al.* [14] have employed it for LC-AO. It consists of a semi-transparent screen with a clear pinhole at the centre [15] shown in Fig. 2.1.
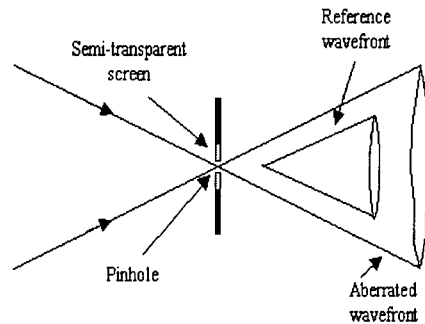
Figure 2.1: The Smartt point diffraction interferometer.

The incident beam is focused down to the pinhole. Most of the light will pass through the screen, some however, will be diffracted into a spherical reference wavefront by the pinhole. Fringes will then be observed between the aberrated and reference wavefronts.

The Shack-Hartmann WFS

This device is probably the most widely used WFS for AO in use today. It consists of an array of microlenses which sense the local wavefront tilt, Fig. 2.2.
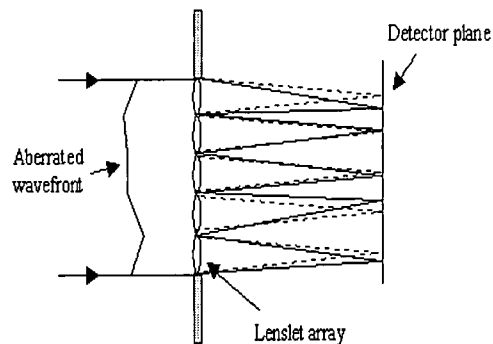
Figure 2.2: The Shack-Hartmann WFS. The dotted lines indicate the spot positions for the reference wavefront.

The manufacture of the microlenses is a science in itself and are they usually taken to have a diameter $d = r_0 m$ where r_0 is Fried's parameter and m is the exit pupil demagnification. There is generally one Shack-Hartmann subaperture per mirror corrective segment, with the lenslet focal length matched to the CCD pixel dimensions, the wavefront being reconstructed from the wavefront tilts.

Curvature Sensing

Roddier [16, 17] has demonstrated a technique which measures the wavefront curvature (the second derivative of the wavefront polynomial). If the intensity is compared either side of focus then the wavefront curvature can be determined. An unaberrated wavefront would have the same intensity profile at equally spaced points either side of focus. One advantage is that the generated signal is directly applicable to the form of certain corrective elements such as membrane or bimorph mirrors - see Section 2.3.3 and hence does not require full wavefront reconstruction.

2.3.2   Indirect Wavefront Sensing

So far only WFS which utilise a measure of the wavefront have been discussed. Another approach is the use of the intensity profile in or around the image plane.

Use of axial intensity

If the axial intensity of a spherically aberrated (SA) system is examined it can be observed that the intensity is zero at a distance of λ either side of focus. The distance between one of these planes and the focal point is a measure of the SA present. Gong [18] shows the possible extension of this to form a complete WFS.

Phase retrieval and diversity

Southwell [19] showed a method whereby the intensity in the exit pupil is compared to that in the far field. It proceeds by making a guess for the Zernike amplitudes and then theoretically combines this with the exit pupil intensity profile and then propagates this to the far-field. Depending on the comparison, a new set of modal amplitudes is tried and the system should move towards the actual system aberration. As can be inferred, this is a highly mathematical technique and the question of uniqueness has not been fully resolved [20].

A similar method termed 'phase diversity' is to use two images, one with a

known amount of 'diversity'. This diversity can either be a phase or wavelength change. Taking this diversity and the two images, with and without this change the wavefront can be corrected [21].

Image Sharpening metrics

The science image is characterised by a single number, the procedure is to then optimise this measure. This is the AO method utilised in this thesis and is explained fully in Chapter 5.

2.3.3 Means of applying the wavefront correction

Once the system aberrations have been sensed a method of applying the correction is required. These devices can either be reflective e.g. a mirror or transmissive such as a liquid crystal spatial light modulator (LC-SLM). If light levels are extremely high such as in laser cavities a phase conjugate mirror may be applicable.

For astronomical optics the two main forms of correction are through the use of segmented or continuous facesheet mirrors although bimorph mirrors with a curvature sensor are in use [16, 22]. This section briefly details some of these devices.

Deformable mirrors

These have a continuous or segmented surface and are deformed by the use of electro-mechanical actuators fixed to the back of the structure Fig. 2.3.

(a) Continuous facesheet mirror   (b) Segmented mirror
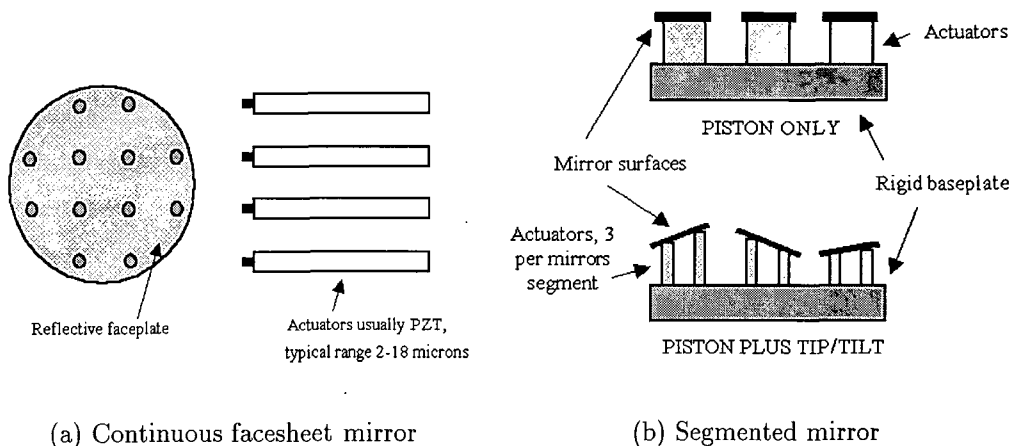
Figure 2.3: Basic form of deformable and segmented mirrors.

The form of the actuators varies, the different materials used have different voltage, hysteresis and temperature dependencies. Continuous facesheet mirrors [1] have been constructed and used on several AO systems, refer to Table 2.1. The positioning of the actuators is important to reduce the crosstalk between neighbouring modes.

Segmented Mirrors use an array of individual mirrors each having tip, tilt and piston control, Fig. 2.3.b. Both SMs and DMs have their relative 'pros and cons'. With a DM it is important for the segments to cophased. Any modulo-λ errors would result in serious image degradation. Segmented mirrors are used in the NAOMI system [23] and also at the Steward Observatory [24]. Manufacturers are the ThermoTrex Corporation[2] and the University of Illinois.

Bimorph technologies

Bimorphs are another form of continuous facesheet mirror consisting of a sheet of piezoelectric material sandwiched between one common electrode and a series of individual ones on the other side. The whole assembly is attached to the reflective surface shown in Fig. 2.4.a. An applied voltage then causes localised mirror deformation. As stated before these are used primarily in conjunction with curvature sensors but do suffer from not having the degrees for freedom for high modal correction.

(a) Bimorph design   (b) Membrane mirror
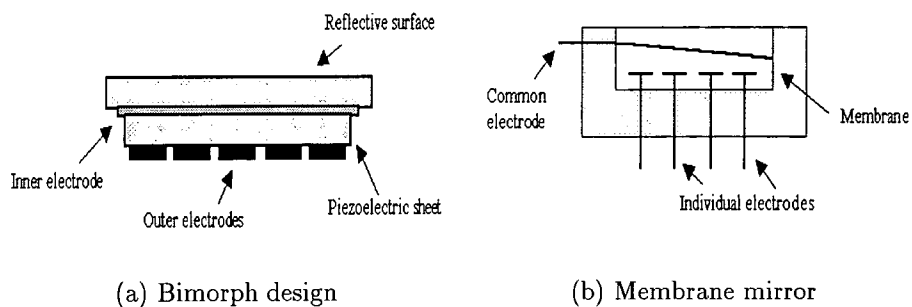
Figure 2.4: Form of bimorph and membrane mirrors

Membrane mirrors

These are possibly the solution for low cost AO. They consist of a membrane arranged between a common transparent top electrode with individual electrodes

---

[1]Xinetics Inc., Fort Devens, MA 01433, USA
[2]ThermoTrex Corporation, 9550 Distribution Avenue, San Diego, CA 92121, USA

at the rear, Fig. 2.4.b. An applied voltage causes an electrostatic attraction between the electrodes. For fuller details see Tyson [10], Chapter 7.

Liquid crystal spatial light modulators

Another low cost option is the use of LC-SLMs. Previous mirror methods relied on changing the OPD by altering the distance component, d, LCs change the refractive index, n. Details of the LC-SLM used in this thesis given in Appendix A and are more extensively discussed in Tyson [10], Chapter 9.

2.4 AO systems in use today

One of the first AO systems to be installed was the RTAC ('*Real Time Atmospheric Compensation*') system in operation in Maui [25] by the USAF. Most of the early systems have largely been superseded, Table 2.1 details the current state of AO systems around the world.

2.5 Active optics

As mentioned before there are slowly varying errors due to the telescope itself. Large aperture telescopes generally have extremely heavy primary mirrors which warp when the telescope tracks. There is also a limit to the size of monolithic primaries, blanks do not exist for mirror diameters exceeding approximately 8m. Recently, the use of segmented primaries have been used, such as in the two 10 Keck mirrors [26] and the new 9.2m Hobby-Eberly telescope (HET) at Mt. Fowkles, Texas [40]. Of course, such mirrors require constant monitoring to maintain segment alignment, something addressed in the references [41, 42, 43, 44].

To correct for mirror misalignments, the secondary mirror is often made the 'active' element. This can be achieved by mounting it on a hexapod system [45]. Focusing errors can then be corrected by a linear translation or coma by addition of a mirror tilt.

The problems of error correction within the AO system themselves are addressed in Chapter 7.

Telescope	Mirror Specification	Operating wavelength	Wavefront Sensor	Guide Star	Detector	Date	Ref.
Keck Observatory (2x10m), Mauna Kea	349 actuator Xinetics DM	IR	241 SH	Sodium	64x64 CCD array @ 2kHz	1998-2000	[26]
Subaru (8.3m), Mauna Kea	36 element bimorph	IR	36 CS	Natural	APD	1998	[22]
Gemini (8m), Mauna Kea	DM	IR	64 SH	Sodium	80x80 CCD array	1998	[27, 28]
MMT upgrade (6.5m), Mt. Hopkins, AZ	324 adaptive secondary	IR	150 SH	Sodium	80x80 CCD array	1998	[24]
Mt. Palomar (5m)	349 actuator Xinetics DM	IR	256 SH	Sodium	64x64 CCD array @ 1kHz	1998	[29]
WHT (4.2m), La Palma	76 SM (228 actuators)	Visible/IR	72 SH	Natural	EEV CCD39 80x80 array	1999-2000	[23]
ESO (ADONIS) (3.6m), La Silla, Chile	52 actuator DM	IR	32 SH	Natural	CCD array		[30, 31]
PUEO (3.6m) Mauna Kea	19 element bimorph	Visible/IR	19 CS	Natural	APD	1996	[32]
Starfire Optical Range (3.5m), New Mexico	941 actuator Xinetics DM	Visible	700 SH	Rayleigh		Online	[33, 34]
Calar-Alto (3.5m), Spain	97 actuator DM	Near IR	SH	Sodium	CCD array	2000	[35]
Lick Observatory (3m), California	127 actuator DM	IR	37 SH	Sodium	64x64 CCD array @ 2kHz	1996-97	[36, 37]
Mt. Wilson (2.5m), UnISIS	177 actuator Xinetics DM	IR	SH	Rayleigh	64x64 CCD array	1998	[38]
Yunnan Obs. (1.2m), China	61 element DM	IR	SH	Rayleigh	Dalsa CCD array	2000	[39]

CS - Curvature Sensor   SH - Shack-Hartmann

Table 2.1: Astronomical AO systems in use or in development for terrestrial ground based telescopes.

Chapter 3

Aberration theory and Image Sharpening

3.1 Introduction

The following two chapters detail the necessary theory required in this thesis. For image sharpening to work, characterisation of the image's intensity profile by use of an image metric is required as is a strategy for searching the correction space. Although intrinsically linked they are the focus of separate chapters.

3.2 Diffraction and Image Formation

As it is the intensity in the image plane that is of prime importance, a necessary aside is needed to explain the form of the observed diffraction pattern. This section describes the mathematics behind diffraction theory and explains optical aberrations in terms of Zernike polynomials. This is then further extended to include a discussion of aberrated point spread functions (PSFs) and to the concepts of the modulation and optical transfer functions, MTF and OTF respectively.

Numerous texts have been written about the theory of diffraction and further information can be found in the references [46, 47, 48].

3.2.1 Kirchoff Diffraction Theory

Christiaan Huygens in 1678 was the first to propose an explanation for the phenomenon of diffraction. His work led to the theorem that

> 'Each element of a wavefront may be regarded a secondary source
> of wavelets whose envelope forms the profile of the wavefront as it

advances'

If plane wavefronts are incident on an aperture then every point in the aperture is a source of secondary wavelets the superposition of which results in the observed diffraction pattern, Fig. 3.1.
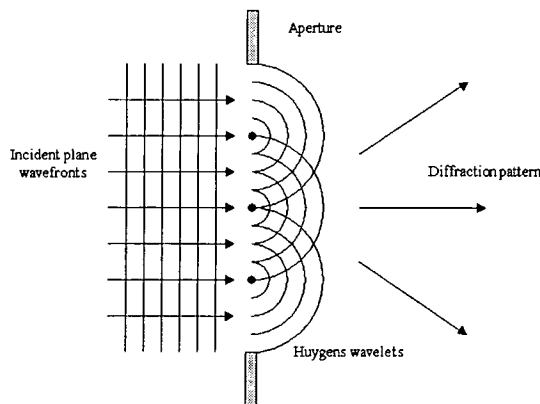
Figure 3.1: Huygens theory of wavefront propagation. Every point of the wavefront incident on the slit is treated as a source of secondary wavelets.

However, there was a need for correction. A point source would, of course, emit a spherical wave. This is not shown in Fig. 3.1 and would lead to the formation of a backwards travelling wave i.e. towards the source. This combined with the inability to explain detailed diffraction effects required reformulation by Fresnel and Kirchhoff.

Fresnel took Huygen's work further and was able to explain the dependance on the wavelength of the light. The Huygens-Fresnel approach still has its problems, for example, the backwards travelling wave. Kirchoff restated this approach in a mathematical form and in doing so removed some of these deficiencies.

The derivation of the Fresnel-Kirchoff diffraction integral is somewhat involved. For the situation depicted in Fig. 3.2 the form of the final equation can be written as follows:

$$U(P) = const \int \int_A e^{+ik(r+s)} dS \qquad (3.1)$$

where $U(P)$ is the amplitude of the disturbance at the point, P and k is the wave vector.
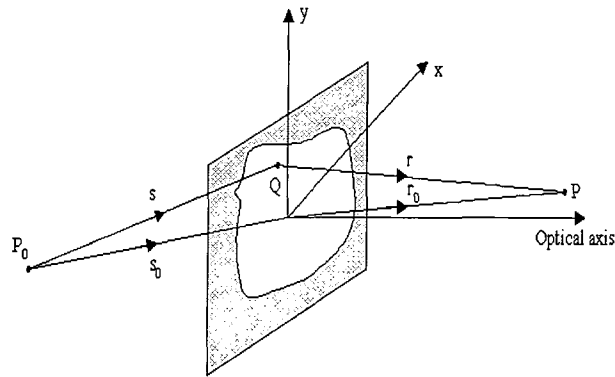
Figure 3.2: Co-ordinate system for the Fresnel-Kirchoff integral.

3.2.2   Aberrations and the use of Zernike polynomials

Optical aberration is measured as the difference in optical path length between an aberrated and a reference wavefront. An unaberrated, converging wavefront will focus to the Gaussian image point and any aberration present will cause a deviation from this. The construction for the aberrated diffraction calculation is shown in Fig. 3.3.
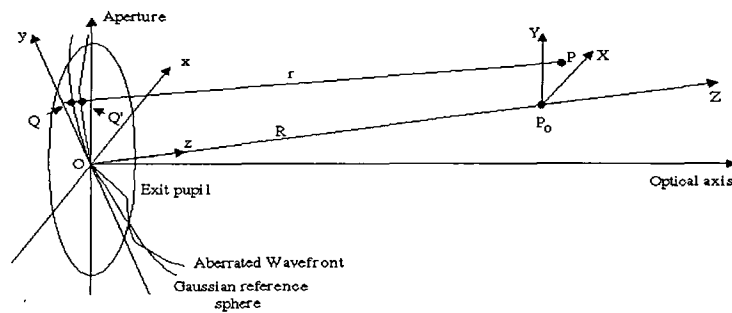
Figure 3.3: Construction of the diffraction integral in the presence of aberrations.

In the absence of aberrations the wavefront would converge to P_0 however, due to aberration the focal point is located at P.

To include the effect of aberrations, s contained by the exponential term in Eq. 3.1 can be replaced by $-(R + W)$ where W is the difference in path length due to the aberration i.e. $Q'Q$. From the geometry can also write

$$r^2 = (X - x)^2 + (Y - y)^2 + (R - z + Z)^2 \qquad (3.2)$$

and

$$R^2 = x^2 + y^2 + (R - z)^2. \tag{3.3}$$

Combining the previous two equations, binomially expanding and neglecting terms such as Z^2 etc, Eq. 3.1 can be recast as

$$U(P) = const \int \int_A e^{-ik\left(\frac{Xx+Yy}{R} + \frac{(x^2+y^2)Z}{2R^2} + W(x,y)\right)} dxdy. \tag{3.4}$$

The first exponential term represents transverse shifts, the second is a defocus term and the third describes the higher order aberrations. The aberration may be expressed in numerous ways, for this thesis Zernike modes are used - see the following subsection.

The full expression for the Fourier amplitude, $U(P)$ for a positive lens of focal length, F at a wavelength λ under plane wave illumination is given by [49]

$$U(P) = \frac{1}{iF\lambda} e^{i\frac{\pi}{F\lambda}\left(1-\frac{d}{F}\right)(X^2+Y^2)} \int \int_A A(x,y) e^{-ik\left(\frac{Xx+Yy}{F} + W(x,y)\right)} dxdy \tag{3.5}$$

where d is the distance in the object space and $A(x,y)$ is the aperture function

$$A(x,y) = \begin{cases} 1 & \text{Inside pupil} \\ 0 & \text{Outside pupil} \end{cases}$$

The defocus expression being absorbed into the term for the aberration.

Zernike polynomials

Throughout this thesis, aberrations are expressed in terms of Zernike modes. This set introduced by Zernike in 1934, is one of many ways of expressing aberrations. They have particular attraction, however, due to several of their properties:

- Perhaps the most important is their orthogonality over the unit circle.

- They are balanced, in that their variance over the pupil is minimised.

Zernike polynomials have been used in a variety of applications. They provide a useful method of representing Kolmogorov turbulence [7, 50, 51], from which the amount of correction can be determined. Bradley *et al.* [52] used Zernike polynomials in calculating the phase disturbance when focusing high power laser

beams. Wang *et al.* [53] show how the Zernike coefficients may be determined from wavefront phase measurements.

Any wavefront (in polar coordinates ρ, θ) can be represented as a summation of angular and radial polynomials as follows [54, 55]:

$$W(\rho, \theta) = \sum_{n=0}^{q} \sum_{l=-n}^{n} C_{nl} R_n^{|l|} e^{il\theta}. \tag{3.6}$$

Where q is the radial degree of the polynomial and l is the angular dependance. Eq. 3.6 can be written in a more manageable form as

$$W(\rho, \theta) = \sum_{n=0}^{q} \sum_{m=0}^{n} A_{nm} R_n^{n-2m} \begin{pmatrix} sin \\ cos \end{pmatrix} (n - 2m)\theta. \tag{3.7}$$

where the sine function is used for $n - 2m > 0$ and the cosine function for $n - 2m \leq 0$. Also m is defined as $m = (n - l)/2$ and note that $(n - l)$ is always even and $n \geq l$.

The radial polynomials can be determined from the following formula

$$R_n^{n-2m}(\rho) = \sum_{s=0}^{m} (-1)^s \frac{(n - s)!}{s!(m - s)!(n - m - s)!} \rho^{n-2s}. \tag{3.8}$$

The first 11 Zernike polynomials [1] are shown in Table 3.1. As can be seen the terms are balanced, for example, coma has its variance minimised by the addition of tip/tilt and spherical aberration is balanced with defocus.

Zernike term	$|l|$	n	Polynomial	Description
0	0	0	1	Piston
1	1	1	$2\rho \cos \theta$	Tip
2	1	1	$2\rho \sin \theta$	Tilt
3	2	0	$\sqrt{3}(2\rho^2\text{-}1)$	Defocus
4	2	2	$\sqrt{6}\rho^2 \cos 2\theta$	Astigmatism
5	2	2	$\sqrt{6}\rho^2 \sin 2\theta$	Astigmatism
6	3	1	$\sqrt{8}(3\rho^2 - 2)\rho \cos \theta$	Coma
7	3	1	$\sqrt{8}(3\rho^2 - 2)\rho \sin \theta$	Coma
8	3	3	$\sqrt{8}\rho^3 \cos 3\theta$	Trefoil
9	3	3	$\sqrt{8}\rho^3 \sin 3\theta$	Trefoil
10	4	0	$\sqrt{5}(6\rho^4 - 6\rho^2 + 1)$	Spherical

Table 3.1: The first 11 Zernike modes.

[1]These expressions are sometime ordered differently

To ease visualisation the Zernike modes were plotted in Matlab © and are shown in Table 3.2. The phase profiles across the pupil are shown.

3.2.3   Strehl Ratio

The Strehl Ratio (SR) of a system is defined as the ratio of the maximum intensity in the aberrated diffraction pattern to that of the unaberrated case. From Eq. 3.5 with $d = F$ we can write the transverse shift terms being absorbed into the expression denoted by $W(x,y)$.

$$SR = \frac{I(0)}{I_0(0)} = \left|\frac{U(0)}{U_0(0)}\right|^2 = \left|\frac{const \int \int_A e^{-ikW(x,y)} dx dy}{const \int \int_A dx dy}\right|^2 \tag{3.9}$$

Binomially expanding the exponential and neglecting the higher order terms, the above equation can be simplified to

$$SR = 1 - k^2[< W^2 > - < W >^2]. \tag{3.10}$$

The term in the square brackets is the variance of the aberration function.

The commonly seen forms for the SR seen in the literature are given by

$$\begin{aligned} SR &= 1 - \delta_{ph}^2 \\ &= \exp(-\delta_{ph}^2) \end{aligned} \tag{3.11}$$

where δ_{ph}^2 is the phase variance. The second expression is more commonly used and is known as the Márechal approximation (valid for wavefront deformations less than $\lambda/14$).

3.2.4   PSFs in the presence of aberrations

The squared modulus of the Fourier transform of the complex pupil function gives the intensity distribution in the image plane. If the object is a point source then this intensity distribution is called the point spread function (PSF). It is useful to know how the form of the PSF varies with applied aberration. Again, a simple program was written to model the behaviour with coma. Several curves are shown in Fig. 3.4 each varying from the other in the size of the applied aberration. The values of the aberration are in waves.
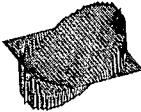
Radial degree, n	Azimuthal frequency, $|l|$			
	0	1	2	3
0	Z_0 Piston			
1		Z_1 Tip Z_2 Tilt		
2	Z_3 Defocus		Z_4 Astigmatism Z_5 Astigmatism	
3		Z_6 Coma Z_7 Coma		Z_8 Trefoil Z_9 Trefoil
4	Z_{10} Spherical		Z_{11}	

Table 3.2: The first 12 Zernike modes (including piston).
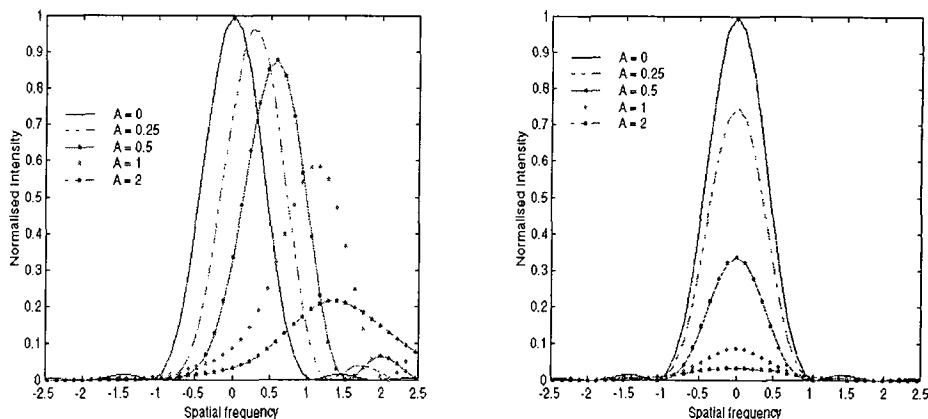
(a) Cross section of the comatic PSF at
0^0

(b) Cross section at $+90^0$

Figure 3.4: Form of the PSF as a function of the coma amplitude.

Table 3.3 shows how the PSF varies when the magnitude of the aberration is increased. For high values the PSF takes on its characteristic 'comet' like appearance.

3.2.5   Optical Transfer Functions

Fourier optics provides an elegant way of describing an optical system's performance. In the previous section, the concept of the PSF was introduced which is the system's response to a point stimulus. This section extends this to the concept of the OTF and hence the MTF. The OTF describes how the spatial frequency content of an image is transferred to the image plane and hence is a useful means of characterising an AO system using image sharpening.

Fourier Optics is more completely summarised in the following diagram, Fig. 3.5. NOTE: This diagram holds for incoherent light, when dealing with coherent light the situation is different and it is necessary to deal with the amplitude of the wavefront.

The OTF is normalised to be 1 at its maximum i.e. perfect resolution. A value of 0 represents the fact that the spatial frequency is not resolved by the system. An object having a sinusoidal profile, for example, would have an OTF of 1 (at that particular frequency) if there was perfect imaging, whereas 0 would indicate a continuous grey tone, the frequency being 'washed' out although light is still present.
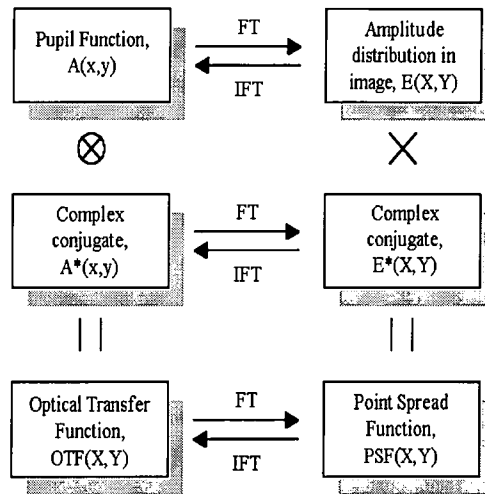
Figure 3.5: Fraunhofer diffraction introducing the concept of the OTF. The $\otimes$ denotes convolution and the $\times$ being multiplication. *FT* and *IFT* denote the Fourier transforms.

Using these concepts one can view image formation by one of two routes. Firstly, the object can be thought of as consisting of a series of discrete points each of varying intensity whereby the use of the PSF allows determination of the image. The other viewpoint is to consider the object as a set of varying spatial frequencies and to use the OTF. The routes are summarised in Fig. 3.6
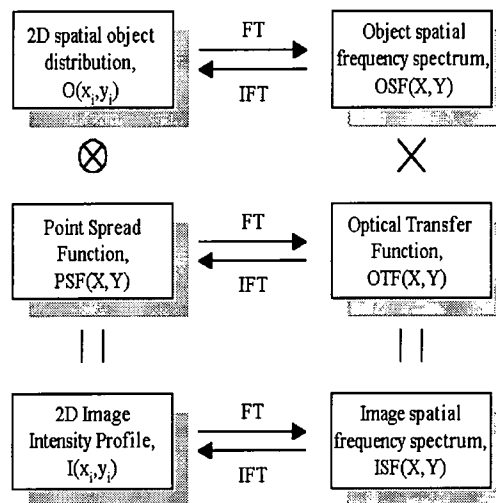
Figure 3.6: Image formation with incoherent light.

To see the effect of system aberration on the form of the OTF, calculations were performed with the same initial conditions as used in the calculation of Fig. 3.4 and Table 3.3. Aberrations will not affect the limiting spatial cutoff frequency of the system as that is defined by the aperture stop of the system but will affect

the modulation depth at lower frequencies.

If the complex pupil function of a comatic wavefront is known then the autocorrelation of this will give the system OTF. The same amplitudes were used as in the previous calculations in this section, the results shown in Fig. 3.7. The negative value for some spatial frequencies implies a contrast reversal i.e. black to white and vice-versa.
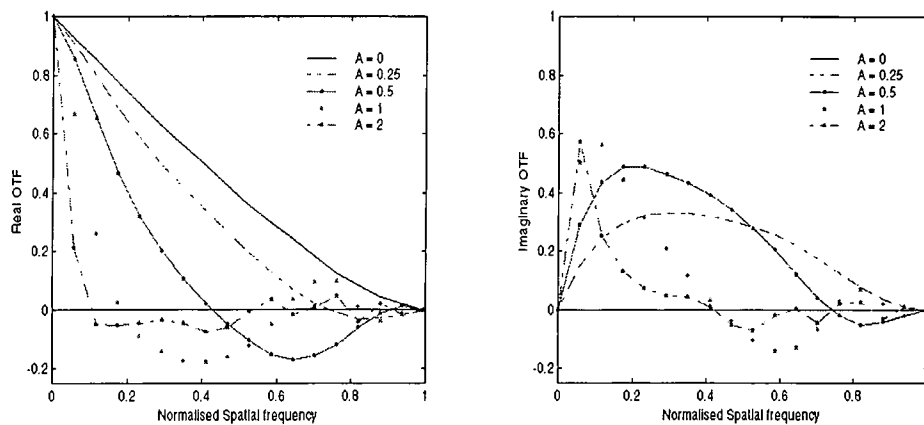
(a) Real part of the comatic OTF at 0^0

(b) Imaginary part at 0^0
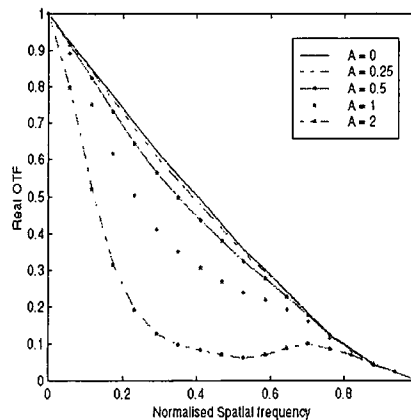
(c) The comatic OTF at $+90^0$

Figure 3.7: Shape of the OTF as a function of the coma amplitude.

The OTF can be expressed as the modulus of the MTF multiplied by the exponential of the phase transfer function (PTF). Namely,

$$OTF = |MTF|exp^{iPTF}. \tag{3.12}$$

The MTF plots as shown in the following diagram - Fig. 3.8

(a) Comatic MTF at 0^0 (b) Comatic MTF at $+90^0$
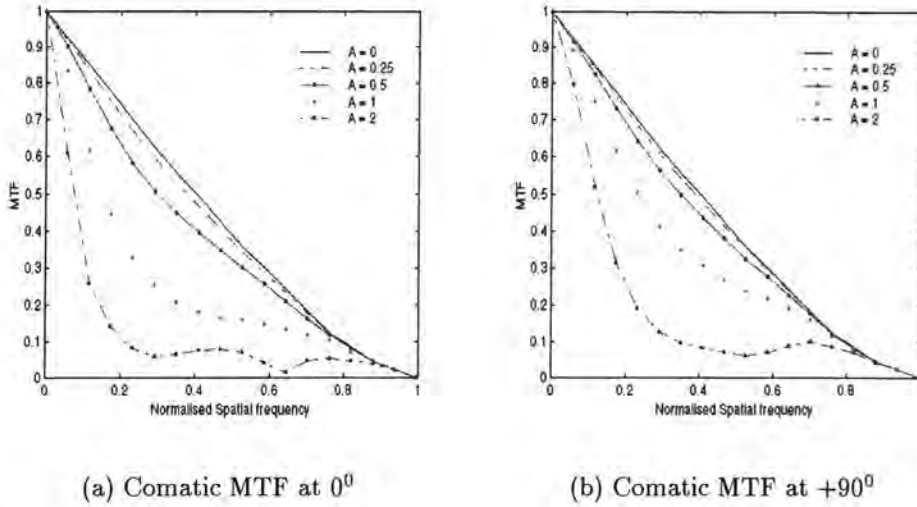
Figure 3.8: Shape of the MTF in the two orthogonal directions.

The 3 dimensional plots are shown in Fig. 3.9. The profile for the case of no aberration is included as a comparison to the aberrated case.

(a) MTF for no aberration   (b) Aberrated MTF
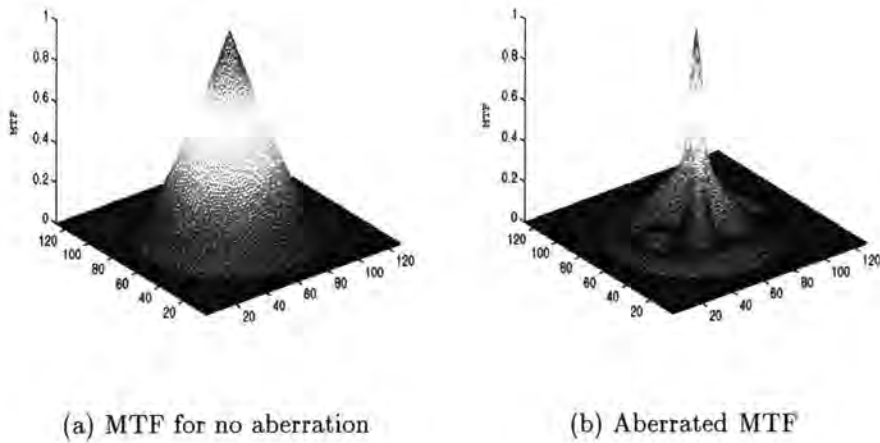
Figure 3.9: The unaberrated and the aberrated 3-dimensional MTFs (for 2λ of coma).

The theory detailed in this section is used in the determination of image quality and, when providing an adaptive correction, a means of quantifying the improvement.

3.3 The Image Sharpening Technique

In direct measurement systems it is the phase, tilt or curvature of the wavefront that is determined and the appropriate conjugate correction is then applied. In an indirect adaptive optics system this measurement is replaced by an image metric. This metric is sensitive to the wavefront phase, although is not a direct measure of it. The metric will give a numerical value called the merit function (MF). Generally, the higher the MF the better the image quality. A trial phase correction is then applied and the effect on the MF noted. If the correction results in a higher value of the MF then the amplitude of the correction is increased. Conversely, a corresponding decrease in the MF means the phase correction is incorrect and another is tried.

For an image sharpening AO system there are two major requirements:

- An image metric should reach its extremum only when the system is aberration free. Ideally, only one maximum (or minimum) should occur even in the presence of noise.

- Merit functions need to be calculated in a time period that is shorter than the temporal evolution of the aberration. For quasi-static system errors this requirement is not difficult to satisfy.

Muller and Buffington [56] were the first to introduce the concept of image sharpness. They defined several metrics and showed that these had their maximum values in the absence of aberrations (for an alternative proof see Hamaker [57]). They envisaged their system as a means of providing full AO correction i.e. for example, replacing the role of a Shack-Hartmann lenslet array. Their correction device consisted of a segmented piezoelectric mirror with six correction elements working in piston only. They demonstrated the technique in the laboratory [58] by correcting the turbulence across a 250 metre gap using both white light and laser sources. Subsequently, astronomical measurements were made at both the Leuschner and Lick observatories in California [59]. Even using a six element mirror, real time atmospheric correction only produced a benefit in the best of 'seeing' conditions, a typical cycling through the mirrors taking approximately 30 ms.

O'Meara [60] describes a similar technique which he terms multi-dithering. The paper describes how the power of a distant detector can be optimised. Each of the correction elements is 'dithered' at a different frequency and the resultant image is examined by a filter bank each tuned to a specific dither frequency. The effect is that there will be an amplitude modulation if the system is not

optimised. The output of the filters is essentially a measure of the phase error at that frequency. The filter output is then the control signal for the mirror i.e. a hill climbing loop has been formed which tries to minimise this signal. He points out that such a system is only really applicable to short range imaging due to the low signal to noise ratio. Also when dealing with a large number of correction elements the bandwidth becomes prohibitively large due to each requiring its own dither response.

More recently, Vorontsov *et al.* [61, 62] has applied the technique to imaging extended objects. A coherent optical processor was used in which the signal from the imaging camera is used to control a SLM illuminated by a coherent wavefront. The output from the SLM will then be spatially modulated depending on the camera signal. If this is then focused onto a rotating frosted glass plate a characteristic speckle pattern will be observed. The smaller the speckle scale, the higher the spatial frequency content of the image. The system is then driven to minimise the speckle size.

Brigantic *et al.* [63] detail other metrics which are measures of the system's spatial frequency response, namely the MTF and cutoff frequency.

Jacobsen [64, 65] talks about the use of image metrics in relation to the human visual perception of an image and it's quality.

3.4 Image Sharpening Metrics

As stated in the introduction, there are two major properties that are required of an image metric. In addition, the type of object to be imaged and ease of implementation are also important considerations. Several metrics [56] are listed below.

$$S_1 = I_{max}, \tag{3.13}$$

i.e. this is similar but not equal to the Strehl Ratio (SR). This can be at the centre of the image whereby tip/tilt is corrected for or determined anywhere in the image plane.

The next MF was used in a system described by O'Meara [60].

$$S_2 = \int |I(x,y)M(x,y)| \, dx \, dy, \tag{3.14}$$

where $M(x,y)$ is a mask function. This mask should be the theoretical PSF in the absence of any aberrations. For a point source this would correspond to a

pinhole with a diameter equal to the size of the diffraction limited image.

$$S_3 = \int |I(x,y) - I_0(x,y)|^n \, dx \, dy, \tag{3.15}$$

i.e. a defect metric where $I_0(x,y)$ is the unaberrated intensity profile. This metric needs to be minimised.

$$S_4 = \int I^n \, dx \, dy, \tag{3.16}$$

where $n = 2, 3, 4$. S_4 with $n = 2$ was used as a selection criterion for choosing the best subset of frames in a postdetection approach developed by Roggemann *et al.* [66].

$$S_5 = -\int I \ln I \, dx \, dy, \tag{3.17}$$

i.e. a measure of the entropy of the image.

Another simple measure is the sum of the pixel intensities in some region of the image space usually termed a 'bucket'.

$$S_6 = \int_{bucket} I \, dx \, dy. \tag{3.18}$$

Metric S_2 would be appropriate for imaging point objects e.g. stars where the mask would correspond to a circular aperture. For extended objects, this image metric would not be appropriate as *a priori* information about the object is required. A similar problem exists with metric S_3 which relies on having a diffraction limited image available, $I_0(x,y)$. It is necessary to choose the correct metric depending on the application. With a pixelated CCD camera array the determination of these integrals is relatively straightforward.

To see how these vary with applied aberration the values were simulated for a system suffering from various amounts of coma. The results are shown in Table 3.3. Below the PSF images are the MF values. All are calculated from the intensity values not the wavefront variance as could be the case for the SR. For all MFs, a trend can be seen towards either a maximum or minimum as the amplitude is increased. For example, minimising the value of I^n would drive the system towards its aberration free state.
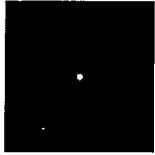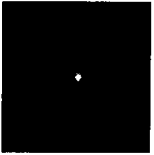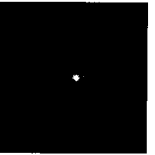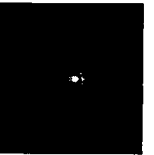
Amplitude	0λ	0.25λ	0.5λ	1λ	2λ
Merit Function Evaluation					
SR	1	0.95	0.87	0.57	0.20
I^2	$6.4e^{-3}$	$6.0e^{-3}$	$5.8e^{-3}$	$5.7e^{-3}$	$2.0e^{-3}$
I^3	$6.1e^{-5}$	$5.6e^{-5}$	$4.1e^{-5}$	$1.2e^{-5}$	$1.1e^{-5}$
I^4	$6.6e^{-7}$	$5.7e^{-7}$	$3.8e^{-7}$	$3.4e^{-7}$	$2.3e^{-7}$
$I\,log_e I$	5.9	6.0	6.3	7.0	7.9
$I - I_0$	0	0.68	1.13	1.54	1.70

Table 3.3: PSF plots for coma. For each value of the aberration amplitude various MF determinations are given.

3.5 Summary

This chapter introduced the idea of image sharpening and the use of a MF to characterise the optical image. This value for the image quality is then optimised by applying a phase correction. This can be in the form of a modal correction (i.e. applying Zernike modes) or could be zonal, namely the adjustment of a single correction segment.

In addition the relevant diffraction theory and the concepts of the OTF and MTF were presented. This theory is utilised in Chapter 5 when the experimental results of AO utilising image sharpening are presented.

Chapter 4

Search algorithm theory

4.1 Introduction

The image sharpening routine requires some means of generating the corrections depending on the value of the merit function. The correction being performed by the LC-SLM or the ELECTRA mirror. How the correction is determined depends on the size of the search space. The search space being related to the number of degrees of freedom (DoF) of the system.

For the work with the LC-SLM the DoF was comparatively small, 13 modes with 21 amplitude settings for each mode. The extension to ELECTRA however, results in a vast increase in the size of the correction space. What is required is a method of efficiently generating the conjugate form of the corrective element when the number of possible configurations for this element is very large. Each possible setting for the mirror segments or Zernike mode is termed a *node*.

It was therefore necessary to look into the application of search algorithms (SA) and several are described in this chapter.

Brief history

The field of search algorithms and optimisation is very large and is constantly expanding and the reader is directed to one of the many texts on the subject [67, 68, 69] for a comprehensive discussion. It is a relatively new field, only really seeing rapid development during the Second World War where the logistical problems of transporting men and equipment were immense. Nowadays, the use of search algorithms and optimisation routines has found many applications, for example, in electronics where the ordering of thousands of components is optimised on a silicon wafer through to chemistry and the determination of reactant quantities and concentrations. The famous optimisation problem of the travelling

salesman has been solved by use of a simulated annealing routine.

4.2 Classification of search algorithms

In Chapter 5, the search space is examined by going through the individual modes and stepping through their respective amplitudes. In the case of Zernike polynomials the modes were assumed to be orthogonal (although this was not the case when the LC-SLM was used - refer to Section 5.2) and the application of one mode should not affect the other. Such a strategy will find the minimum of the system albeit possibly after a couple of cycles. For zonal correction however, this is not the case. For the work with the ELECTRA mirror (detailed in Chapter 6) modal correction is not applied. Instead, individual mirror elements are adjusted for tip, tilt and piston. With a system having a large number of degrees of freedom the search space is vast. This is where the use of a search algorithm is extremely useful.

Broadly speaking, the means by which the solution space is searched can be broken down into two classes, systematic and non-systematic. Table 4.1 explains and contrasts the two schemes. These rules are very general and there are exceptions and these will be mentioned as they arise.

Systematic	*Non-systematic*
Traverses the whole search space visiting every node	Chooses the best node and disregards the rest
Visits every node once and once only	They do not remember where they have been and may trace the same path again
Generally requires more memory and time due to the requirement to visit and remember every node	Maximum amount of freedom, they do not stick to a unpromising route
	Generally their performance decreases when the solution density is low and may not find a solution
Becomes cumbersome in systems with numerous DoF	Better for large search spaces but termination criteria need to be specified else the algorithm will not stop
Examples: Depth or breadth first	*Examples*: Simplex, simulated annealing, genetic or evolutionary routines

Table 4.1: Comparison of systematic and non-systematic search strategies.

The choice of search algorithm is purely application dependant, there is not

one particular algorithm which is optimum for all situations. Considerations can be the solution density, the number of localised minima or the ease of first derivative calculation etc.

4.3 Systematic search strategies

With reference to Chapter 5 where the use of the LC-SLM is described, a depth first search strategy was used, Fig. 4.1. The correction amplitude of each Zernike mode is optimised in turn before moving to the next one. A breadth first routine on the otherhand would vary each mode by one increment then move to the next one, cycling through all modes several times, each time varying the amplitude by one step.

This assumes that the Zernike modes are orthogonal with respect to their effect on the merit function, i.e. the correction of one mode will not affect the value of the previously set mode. This is only approximately true as will be seen later.
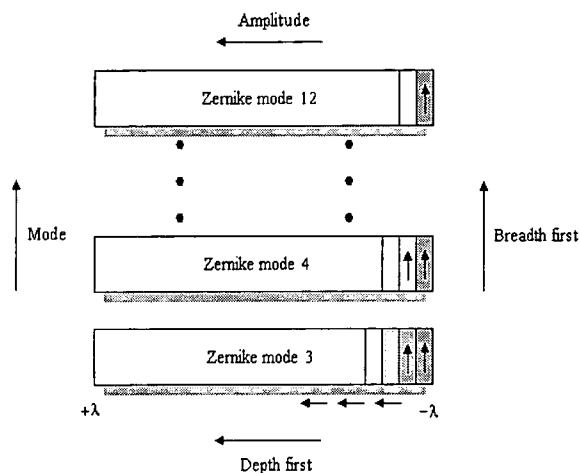
Figure 4.1: Breadth and depth first search strategies with reference to the Meadowlark LC-SLM experiment.

Ideally, when using a search algorithm routine the *global* minimum is the final state i.e. the true minimum of the system. This is very difficult to find for systems having a large number of DoF, the probability of falling into *local* minima is greatly increased. For multi-dimensional optimisation this is a real problem and provides a gauge of the effectiveness of a particular algorithm. For complicated optimisation problems, non-systematic search routines will give the best solution.

For image sharpening applications the functions to be minimised are usually well behaved - see Section 3.4. The problem however, is the vastness of the search space. For example, the ELECTRA mirror has 76 segments each having three degrees of freedom. If just piston is considered, dividing the full range of travel into 100 increments would results in 100^{76} possible combinations. The addition of tip and tilt increases this number still further. The actual end to end piston is 6μm with 6 nm resolution, it is not hard to see that a systematic search would be unfeasible.

4.4 Non-systematic search strategies

Within the non-systematic class there exists further subdivisions. Most use some form of line minimisation (explained shortly). This may be achieved by using explicit function evaluations or derivatives. Indeed routines exist which use both, switching between schemes as conditions permit.

1-D line minimisation

Take for example, 1-dimensional minimisation - Fig. 4.2. If the minimum is bracketed by the interval $(a < b < c)$ then if a trial point x is tried and the function evaluated then the search space can be reduced to either the interval $(a < b < x)$ or $(b < x < c)$. For the case shown, the former interval would be applicable. How the trial points are evaluated is an open question. For example, the golden search proceeds by reducing the interval by a preset ratio - the golden ratio, hence the name. Other routines rely on inverse parabolic interpolation whereby a parabola is fitted between three points a, b and c and the minimum of this is then found. Golden search routines generally expect the worst and are used to 'get things moving' towards the minimum and as the minimum is approached parabolic interpolation can then be used. Other algorithms use the function gradient to provide a means of obtaining the next trial point.

In one dimension, bracketing the minimum is relatively straightforward. This is not the case with multidimensional problems. Algorithms to solve these rely on utilising a carefully selected set of 1-D line minimisations. A few algorithms exist which assume no *a priori* information about the system. Simplex and simulated annealing routines fall in to this category. The following few sections detail several algorithms which have been tested, theoretical and experimental results are given in the later chapters.
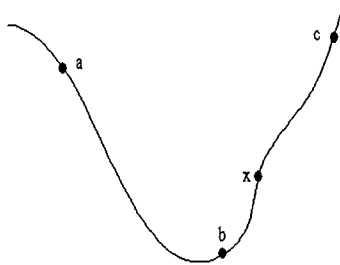
Figure 4.2: 1-dimensional minimisation, the minima is bracketed by the set of points $(a < b < c)$, x is the trial point.

4.4.1 The downhill simplex method

One of the most well known optimisation programs, the simplex algorithm was originally developed by Dantzig in 1947. The method used here is the modified version of Nelder and Mead [70]. It is a very elegant method and is robust although it does require many iterations.

A simplex is a geometrical figure consisting of $N+1$ vertices where N is the number of degrees of freedom. In two dimensions the simplex would be a triangle and in three would be a tetrahedron etc. For the ELECTRA mirror having 76 actuators (each having tip, tilt and piston adjustment) the number of DoF is $N = 228$. The algorithm is started with $N+1$ points defining an initial simplex. If an initial point is called P_0 then the other N points are given by

$$P_i = P_0 + \lambda n_i \tag{4.1}$$

where n_i are N unit vectors and the λ is a constant, the size of which is dependant on the problem.

For an image sharpening system the function to be minimised is the merit function, MF. The value of the MF is of course dependant on the mirror figure. If nothing is known about the system aberrations then a logical place to start would be around a flat mirror and the initial $N+1$ vertices are then generated around this using the values for the mirror tip/tilt and piston. The algorithm then attempts to improve the worst vertex that it encounters by moving to a different position in doing forming a new simplex, and the process then repeats in an iterative manner. Moving away from the worst vertex has the benefit that it better explores the search space but with an increase in the number of iterations required. The simplex can perform one of several manipulations to improve the merit function as illustrated in Fig. 4.3.
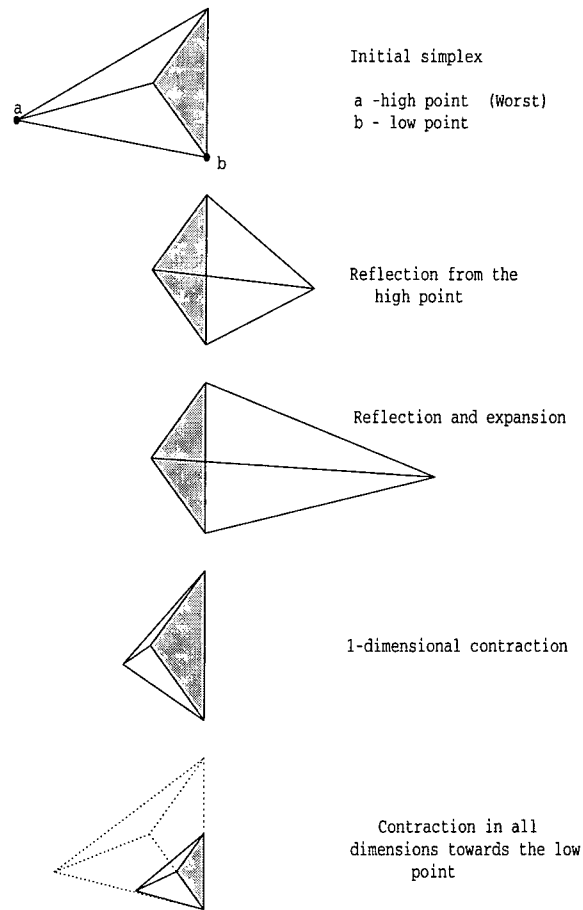
Figure 4.3: Possible simplex manipulations.

The algorithm is summarised in Fig. 4.4. Three values of the MF are needed namely the highest MF(hi) - which is the worst vertex (the function is being minimised), the second highest MF($2nd\,hi$) and the best MF(lo).

Two points are worth noting:

- The generation of the initial simplex requires careful consideration. If it is too small the simplex search everywhere and see the same value and exit. If the simplex is too large then the possibility of falling into a false minimum is increased and it may take a long time to converge.

- Termination criteria can either be specified by performing a certain number of transformations or by specifying some function tolerance condition (FTOL) such that if the simplex is manipulated by a distance smaller than this then the program exits.

The first of these points is highlighted by the following simple example. Consider finding the minimum of the equation,
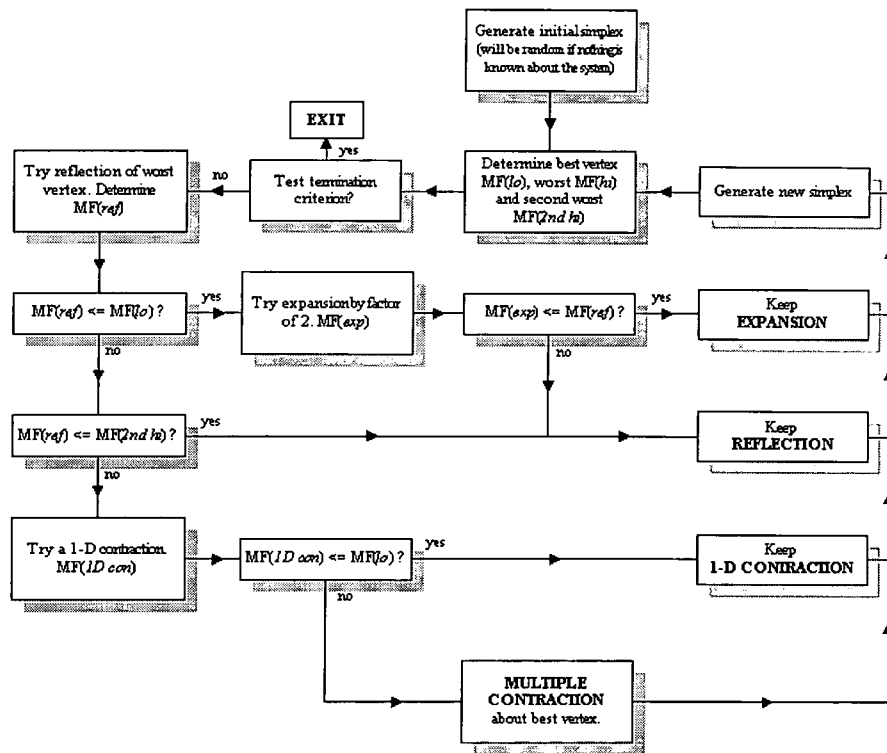
Figure 4.4: Flow diagram for the downhill simplex routine.

$$f(x, y) = x^2 + y^2 \qquad (4.2)$$

with an initial simplex generated by the points

$$\left\{ (1,1), \quad (1,-1), \quad (-1,1) \right\}. \qquad (4.3)$$

The minimum of this equation is obviously at $(0,0)$ but the vertices of the initial simplex are equidistant and return the same value. The simplex can therefore not determine the worst or best point and exits.

Another possibility worth considering is restarting the routine after it has initially converged. It may be the case that the simplex has become trapped in a localised minima and the use of a 'nudge' is sometimes beneficial. The hard work has already been done in the first cycle so the increase in the number of iterations will not be great.

The simplex algorithm has found several applications in the optical field. Arnold [71] describes the use of the algorithm in optimising the support locations for thin mirror telescopes. Mehta [72] was one of the first to use it for adaptive correction.

4.4.2 The simulated annealing algorithm

Akin to genetic algorithms the theory behind simulated annealing has its basis in a natural process. It is known from the study of thermodynamics that if a substance, for example, a liquid, is cooled fast i.e. quenched then the final energy state is likely to be amorphous in nature and will not be a minimum. However, if the metal is cooled slowly and allowed to reach equilibrium at a specific temperature then the final state will be crystalline and the energy state is likely to be the global minimum.

To explain the process it is necessary to detail some of the mathematics underlying the Boltzmann distribution of molecular energies within a thermodynamic system. For a state, s there exists an associated energy, $E(s)$, so for a particular temperature, T the probability, $P(s)$ of the system being in that state is given by,

$$P(s) = \frac{e^{\frac{-E(s)}{kT}}}{\sum_{i=1}^{S} e^{\frac{-E(i)}{kT}}} \tag{4.4}$$

where S is the total number of states and k is the Boltzmann constant.

So even at a low temperature there is a probability that some of the molecules have a high energy. It is this property of the algorithm that is particularly appealing as it provides a way for the routine to get out of a local minimum, although the possibility of this decreases with a corresponding decrease in temperature. In other words, the system will sometimes take a step towards a worse state in order to give it a chance of going on to find a better one. In the regime of low temperatures the algorithm mirrors that of conventional hill-climbing routines.

Metropolis [73] then incorporated this into a scheme whereby the system reaches thermal equilibrium for a given temperature, T. If E_1 denotes the initial energy and the perturbed value given by E_2 then the probability of accepting the new state is

$$P(accept) = e^{\frac{-(E_2-E_1)}{kT}}. \tag{4.5}$$

If $E_1 > E_2$ then $P(accept) > 1$ and the new solution is accepted otherwise the probability of acceptance is given by Eq. 4.5.

Two other parameters need to be set in order for the implementation of the algorithm, namely:

- A method of generating the new energy states E_2

• An annealing schedule to reduce T

Press *et al.* [74] believe that previous methods of generating the new random trial points at a temperature T is inefficient and incorporate a simplex approach. Kirkpatrick [75] describes how the problem of setting the annealing schedule can be overcome. Using the technique described in [74] the following flowchart, Fig. 4.5 describes the implementation.
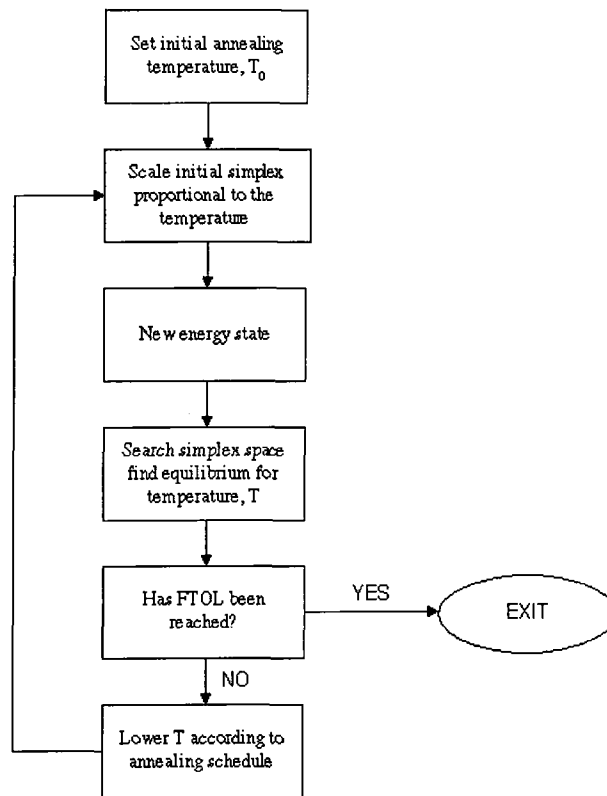
Figure 4.5: Flow diagram of the simulated annealing routine.

The overall process is governed by an annealing schedule, for a value of T the simplex scales itself to this temperature. Random temperature perturbations are then added to the vertices of the simplex and minimisation performed. It is the addition of these random temperature perturbations which is the key to the success of the algorithm and mimic random Brownian motion. As $T \to 0$ the algorithm should tend towards the global minimum.

Simulated annealing has found a 'niche' in problems where there are lots of localised minima and also where the search space has a discrete set of values (combinatorial optimisation). For example, when minimising a function of two variables, the search space is continuous i.e. altering one variable does not preclude changing the other. For discrete problems, the situation is slightly different,

finding a downhill path and keeping on it is not possible due to the fixed nature of the variables.

One famous problem that simulated annealing overcame was that of the travelling salesman. The problem consists of a salesperson wanting to visit N cities once and once only and in doing so taking the shortest route. The problem increases rapidly in complexity as N increases and is subject to numerous local minima.

The situation can be further complicated by the addition of a river dividing the cities. If there is a penalty incurred crossing it then the annealing algorithm will first determine the situations which cause the greatest change in the energy states. In other words at high values of T the algorithm will try to minimise the number of river crossings. As T decreases more emphasis is placed on finding the best path on each side of the river.

As the simulating annealing algorithm is relatively new its use in optics has been limited.

4.4.3 Powell's direction set - the use of conjugate directions

As alluded to earlier, another way of achieving multi-dimensional minimisation is to treat the problem as a set of 1-D line minimisations. An algorithm can be envisaged whereby the system is moved along the first direction to its minimum, from there along the second direction to its extremum and so on. The difficulty with this approach is finding suitable directions in which to proceed.

Powell devised a scheme where minimisation along one direction does not affect the outcome of subsequent ones. The set of directions having this property are known as 'conjugate directions'. Such a set will avoid repeated cycling through the directions. In theory a function should be minimised after N such line minimisations. Strictly, this only holds for functions having a quadratic dependance but even close approximations will converge.

Given a starting point P_0 and an initial set of directions, u_i where $i = 1 \rightarrow n$, repeat the following procedure:

- Minimise in turn along the directions u_i.

- Determine the direction from P_0 to the last point P_N.

- Minimise along that direction and take the minimum as the new starting point, P_0.

- Replace the direction which resulted in the largest function decrease with the new direction. This ensures that the whole space is searched and not just a subspace but does give up the condition for conjugate directions.

This procedure is shown graphically in Fig. 4.6.
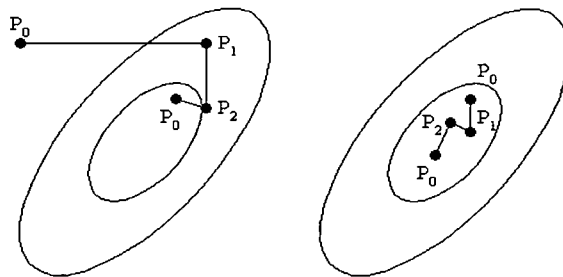
Figure 4.6: Implementation of Powell's method.

Other conditions are tested to ensure the new direction will lead somewhere. Powell's algorithm generally converges more quickly then either the simplex or simulated annealing routines. The drawback being the information about the system is required i.e. in the bracketing of the line minima.

4.4.4 Application of the search algorithms to the ELECTRA mirror

This section attempts to clarify the means by which the mirror parameters are related to the input values for the search strategies. In essence, to achieve a corrected image the corrective element is controlled by one of the described SAs. The aim being to drive it to the form that gives the maximum value for the MF in the far field.

For the downhill simplex and simulated annealing routines each vertex of the simplex corresponds to the MF value for a different, initially, random [1] mirror configuration. These vertices are then manipulated around the centroid of the simplex, always moving towards a configuration that gives a higher MF. The size of these steps will be some integer multiple of the minimum mirror translation governed by the actuator properties (approximately 6nm).

For Powell's method the situation is slightly different. Again, random mirror arrays are generated but this time each mirror form specifies a particular direction

---

[1]By random it is implied that small perturbation voltages are added to the actual mirror voltages to form an initial search space

along which the MF is optimised. Repeated minimisation will move the system towards towards the conjugate state.

With all three algorithms the values for the initial tip, tilt and piston are simply the actuator voltages read from the mirror control system. Occasionally, a small perturbation voltage is then applied to knock the system out of any localised minimum. It should be borne in mind that at no time is the aberration sensed directly, the only values the SAs have are the actuator drive voltages and the MF. The next mirror state being generated on the outcome of the MF determination which is in turn dependant on both the mirror figure and the aberration present.

The algorithm on completion will have as it's output the 228 mirror values which correspond to the highest, achieved MF. The system is then deemed corrected.

4.5 Conclusions

Several search algorithms have been described. In the next chapter they were tested to see their performance when flattening an initially distorted mirror. At the start of an evening's observations the optics will have its highest misalignment. It is envisaged that subsequent corrections will require less time as the already corrected system (albeit drifted) could be used as the starting point.

The final, achieved state and the number of iterations required are therefore important considerations. All have relatively light computational overhead and are fairly robust. The next chapter describes the implementation of these search strategies.

Chapter 5

Simulation and experimental testing of image quality metrics

5.1 Introduction

In the Chapter 3 the relevant diffraction theory was explained and the concept of image quality metrics or merit functions introduced. This section details both simulation and experimental work using such metrics. Only static aberration correction was examined and the corrective device used was a Meadowlark Hex-69 LC-SLM (see Appendix A) driven in both the modal and zonal regimes. Both a point and extended object correction was investigated and their performance with various image metrics detailed.

5.2 Simulation of various image metrics

To look at the behaviour of various metrics, a computer simulation was written using Matlab ©. The first was to simulate the effect on the value of various MFs for a system suffering from spherical aberration (SA). To do this the amount of SA was varied from $+1\lambda$ to -1λ in incremental steps (λ - wavelength) with the MF determined at each step. The Zernike representation was used throughout in forming the phase screens.

Fig. 5.1 shows the behaviour of several metrics listed in Section 3.4. NOTE: All the metrics were divided by the sum of the pixel intensities, the only exception being S_1 which was divided by the maximum pixel intensity for the diffraction limited case. Normalisation to one for Fig. 5.1.a was achieved by dividing by the peak value for each metric.
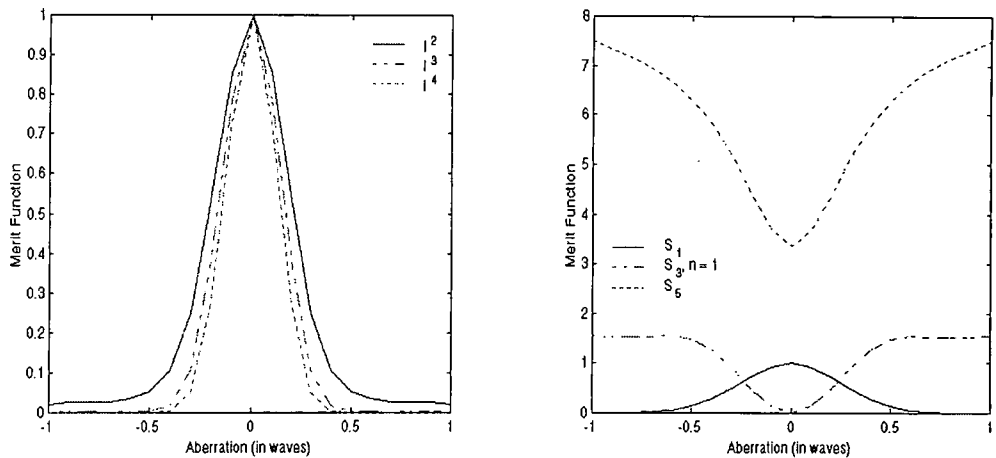
(a) Metric: $S_4 = I^n, n = 2, 3$ and 4.   (b) Metrics: $S_1 = I_{max}$, $S_3 = \int |I(x,y) - I_0(x,y)|^n \, dx \, dy$ and $S_5 = -\int I \ln I \, dx \, dy$.

Figure 5.1: Behaviour of various image metrics when SA is present.

As can be seen, for all the metrics there exists a maximum or minimum at zero aberration. Ideally, the gradient of the metric should change rapidly when the system reaches optimum (zero aberration) in this way any effect of noise will be reduced.

Next, the whole system was simulated for a particular metric. An incident wavefront was represented by a summation of the first 13 Zernike terms with random amplitudes excluding tip/tilt. The correction was simulated by generating a phase screen and subtracting this from the incoming phasefront. This was then Fourier transformed to give the resulting PSF. Each Zernike mode was stepped through, varying the amplitude from $+1\lambda$ to -1λ in 0.1λ steps and then noting the effect on the PSF and the corresponding value of the MF.

Fig. 5.2 shows the unaberrated PSF and the aperture function. The pupil had a value of 1 inside the pupil and zero anywhere else. It is difficult to simulate a truly circular aperture as shown by the 'rough' edges of the aperture. Decreasing the sample spacing across the aperture improves this but at a cost in processing speed.

Introducing random Zernike amplitudes resulted in the PSF and phase screen shown in Fig. 5.3. The merit function used was S_4 with $n = 2$. The setting for one particular mode was held at the amplitude which gave the maximum value for the MF, the next Zernike mode was then stepped through. The mode order was from 3 through to 15.
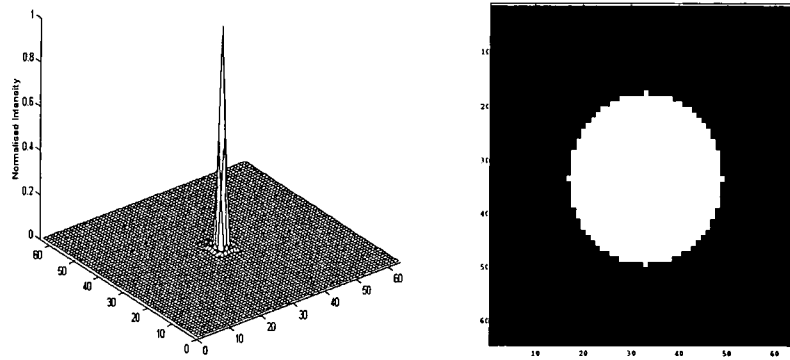
Figure 5.2: The initial, unaberrated point spread function and pupil function, SR = 1, MF = 0.0894.

The initial SR was 3.3% with an rms. error (in waves) of 0.294. The legend for the aperture subplot is in waves. All intensities were normalised allowing for easier comparison between images.
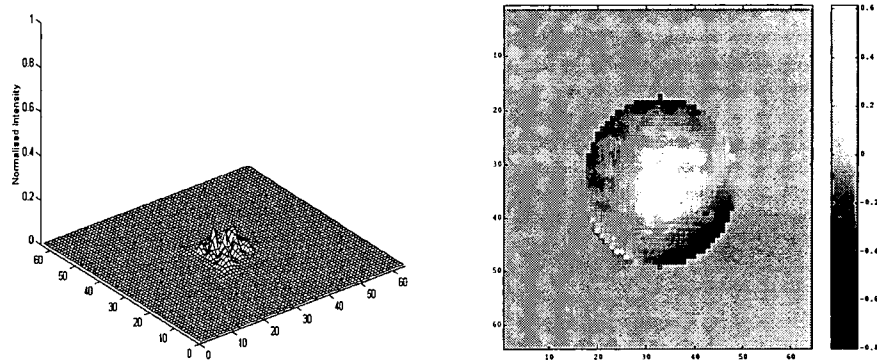
Figure 5.3: The aberrated point spread function and aperture phase screen, MF = 0.0078, rms. =0.294, SR = 3.3%. The legend is in waves.

After correction the PSF has the following form shown in Fig. 5.4, as can be seen the phase variation across the aperture is much reduced. The MF has also increased as expected. The modal amplitudes for S_4 with $n = 2$ are given in Table 5.1, with the figures in fractions of a wave. The resultant rms. error is 0.103 with a corresponding Strehl ratio of 73.8%. Only one cycling through the 13 modes was performed.
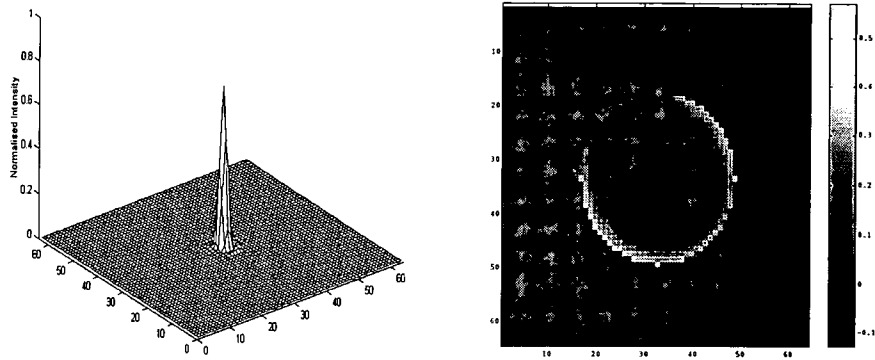
Figure 5.4: The corrected PSF and aperture function for 15 Zernike modes after 1 iteration, MF = 0.0562, rms. = 0.103, SR = 73.8%.

Zernike mode	3	4	5	6	7	8	9	10	11	12	13	14	15
Aberrated wave	-0.4	0.1	-0.3	-0.1	0	0.2	0.2	0	0.1	-0.1	0	0.1	0
Corrected wave	-0.5	0.1	-0.2	-0.1	-0.1	0.1	0.2	0	0.1	0	0	0	-0.1

Table 5.1: Aberrated and corrected amplitudes (in terms of λ) for S_4 with $n = 2$ for one cycling through the modes.

Effect of a second iteration

To investigate effect of a second iteration, the correction cycle was repeated. If no improvement was seen on the second pass then the amplitude was kept at the modal amplitude value given by the first cycle. As can be seen in Table 5.2, it is theoretically possible to achieve 100% correction. It has to be remembered that this is not unexpected as Zernike modes are being used to correct for an aberration given by Zernike modes and no fitting error has therefore been assumed. In addition, there is no noise contribution.

Zernike mode	3	4	5	6	7	8	9	10	11	12	13	14	15
Aberrated wave	-0.4	0.1	-0.3	-0.1	0	0.2	0.2	0	0.1	-0.1	0	0.1	0
Corrected wave	-0.4	0.1	-0.3	-0.1	0	0.2	0.2	0	0.1	-0.1	0	0.1	0

Table 5.2: Effect of a second iteration through the search space.

The improvement after the correction of each mode is shown in Fig. 5.5. The second cycle starts with the modal values given by the first complete iteration.
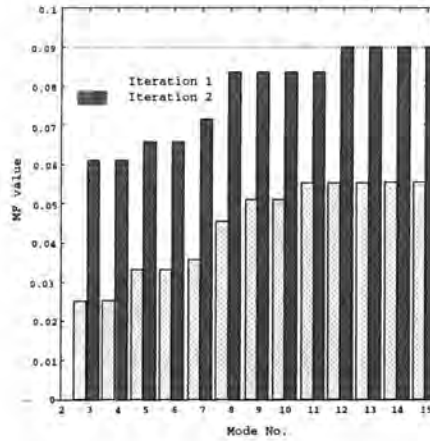
Figure 5.5: MF values after 1 and then 2 iterations. The diffraction limited MF is given by the dotted line at MF value = 0.0894.

The next graph, Fig. 5.6 shows the forms of the MTF at various stages through the correction procedure. As expected the cut-off frequency is not affected but the modulation is improved at the lower spatial frequencies. The MTF in the third subplot being that for an unaberrated, circular pupil.
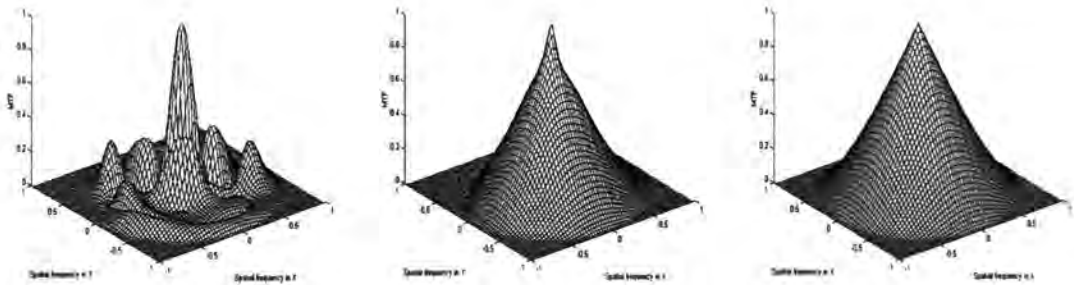
Figure 5.6: The MTF, initial, after 1 iteration and then 2 iterations.

5.3 Experimental Testing with the LC-SLM

In order to test the metrics described in the previous section an experiment was devised to correct for the static aberration introduced by a piece of glass. Two sets of experiments were performed, one with a point source with laser illumination and another with an extended source under white light illumination.
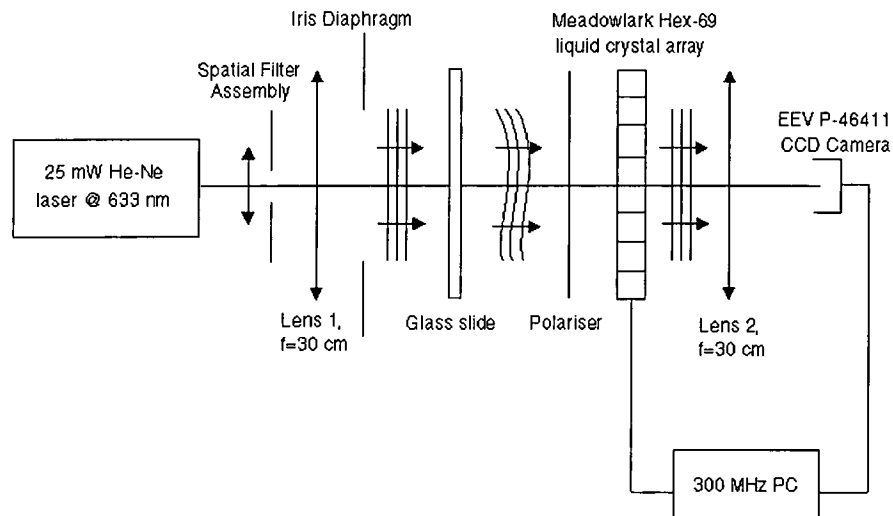
Figure 5.7: The experimental set-up for testing image metrics under static correction.

Fig. 5.7 shows the experimental set-up for the point source, the output from the laser is spatially filtered and then collimated by lens 1. The diameter of the collimated beam can be controlled by the iris. The glass slide producing the aberration. The distorted beam then passes through a polariser with the transmission axis vertical and then goes through the LC-SLM. Lens 2 focuses the beam onto the CCD camera which records the image.

The camera and the LC-SLM were controlled by a single PC running Lab-Windows/CVI. This allowed for the writing of programs in C which could control the hardware through the use of a graphical user interface (GUI). A flow chart representing the experiment is shown in Fig. 5.8.

Modal and zonal correction

As the Meadowlark LC-SLM is a pixelated device it is possible to apply the correction by either altering the phase of a single pixel (zonal) or applying a phase screen to the whole array (modal). Both methods were tested and the modal approach found to be the more favourable. This was due to the higher speed
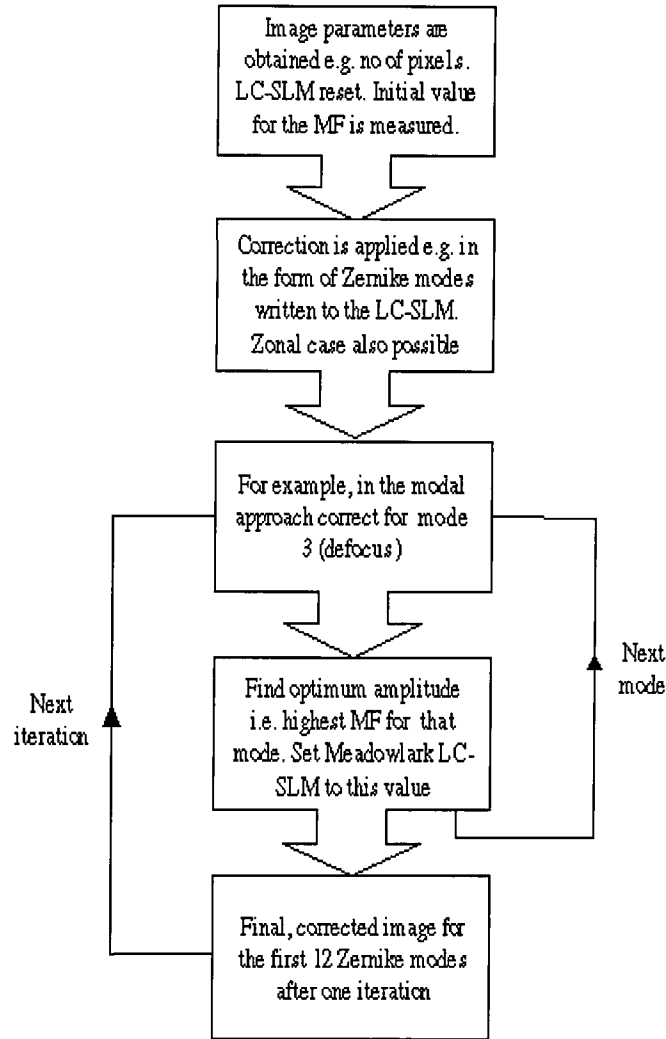
Figure 5.8: Flow diagram showing the correction routine.

of application and less susceptibility to noise and camera sensitivity. Results for both schemes are presented.

5.3.1 Experimental results for the point source

The set-up in Fig. 5.7 essentially images the pinhole of the spatial filter assembly onto the camera. The lenses 1 and 2 provide a 1:1 magnification. The wavefronts were assumed to be planar between lenses 1 and 2 and divergence was therefore ignored. The collimated beam diameter was set to be fractionally larger than the active area on the LC-SLM i.e. $D=\sim15$mm. The expected spot diameter, d at the focus of lens 2 was calculated from Eq. 5.1

$$d = 2.44 \, \lambda \, f_{no} \qquad (5.1)$$

where λ is the wavelength (633nm) and f_{no} is the ratio of focal length to the lens diameter.

Thus d=30μm. This was magnified using a x10 microscope objective with a tube length of 100 mm which gave an image diameter of 30x5.5=166μm. The 5.5 coming from 10x100/180 (x10 magnification for a nominal tube length of 180 mm). To verify that the system was well aligned, a typical unaberrated spot had a diameter of 17 pixels with each pixel being 10 μm in length.

The computer program was not optimised for speed as only a static aberration was being corrected for. Each time the optimum amplitude for a particular mode was found the image was 'grabbed' and stored. The series of graphs, Fig. 5.9 shows the evolution of the correction for I^2. Results for S_4 for where n=2, 3 and 4 and also for S_1, S_5 and S_6 were recorded in one experimental session so that the results are directly comparable.

5.3.2 Modal results for various merit functions

The system was initially tested without the glass slide present. One advantage of using this technique is that any system aberrations are also corrected for. Some improvement was observed, typically a defocus error in the positioning of the camera. The system was held in this corrected state and the modal amplitudes used as an offset for the LC-SLM.

The image was then captured when there is no aberration present, with the aberration added and then after each subsequent correction of a Zernike mode. Both a 3-D and a contour plot are given.

Evolution of the correction under $S_4 = I^n$ with $n = 2$

Fig. 5.9 show the evolution of the PSF after applying the individual Zernike modes. The rms. wavefront error was calculated from the Strehl ratio (SR) using Eq. 3.11.

The figure given for the intensity is the grayscale level from the 8-bit camera which has a range of 0 to 256. The laser was attenuated so that the maximum intensity for the unaberrated case was at the top end of this range, the introduction of the aberration will, of course lower the intensity level. At each correction stage several frames were recorded and averaged to give the mean MF.

The set of graphs, Fig. 5.9 show the increase in image quality after correction for the individual Zernike modes. The correction amplitude was from -1λ through to +1λ in 0.1λ steps. The whole correction process took about 90 seconds for one iteration. Investigation using a Zygo [1] phase shifting interferometer showed that only the first ten Zernike modes need be considered - see Section 5.3.2. Tip/tilt was ignored and the rms. error is in waves. NB: The rms. error was calculated from the SR using the Márechal approximation not the pupil variance.
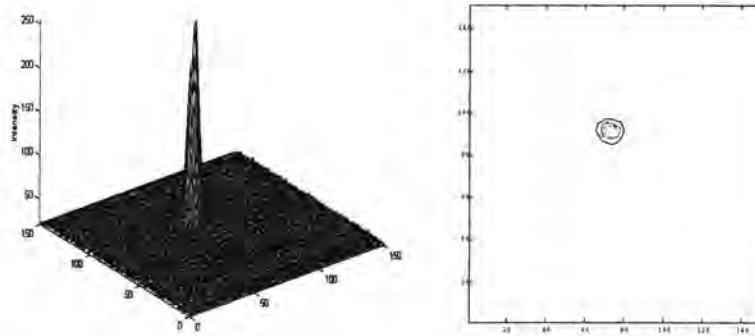
a) Unaberrated PSF. MF = 0.4870, Maximum intensity = 254.
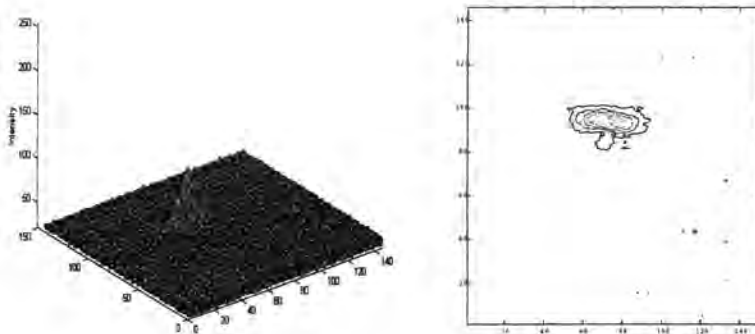
b) Initial, aberrated PSF. MF = 0.4550, rms. error = 0.171, SR = 0.36.

---

[1]Zygo, Laurel Brook Road, Middlefield, Connecticut, 06455-0448 USA
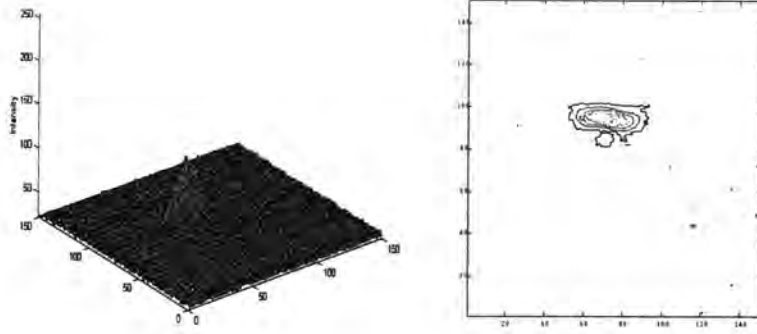
c) PSF after correction for mode 3. MF = 0.4651, rms. error = 0.170, SR = 0.37.
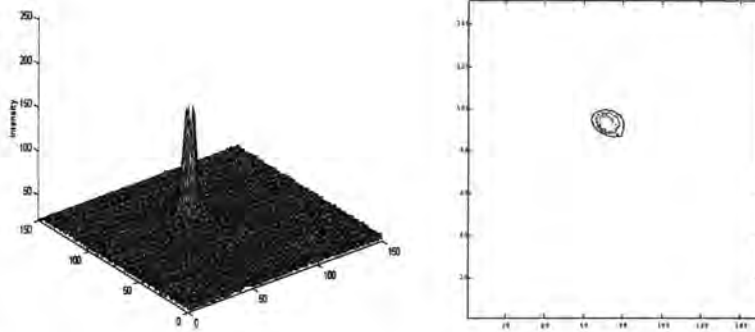
d) PSF after correction for mode 4. MF = 0.4717, rms. error = 0.114, SR = 0.60.
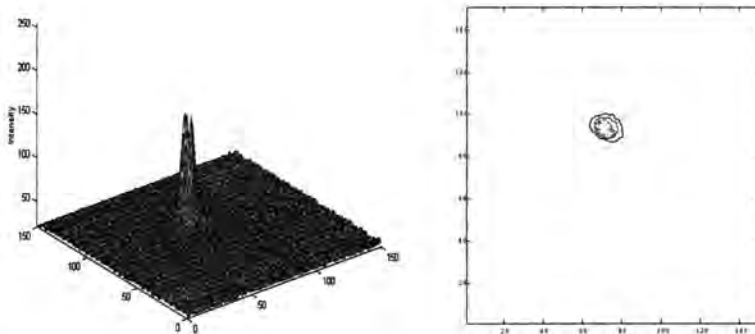
e) PSF after correction for mode 5. MF = 0.4719, rms. error = 0.113, SR = 0.60.
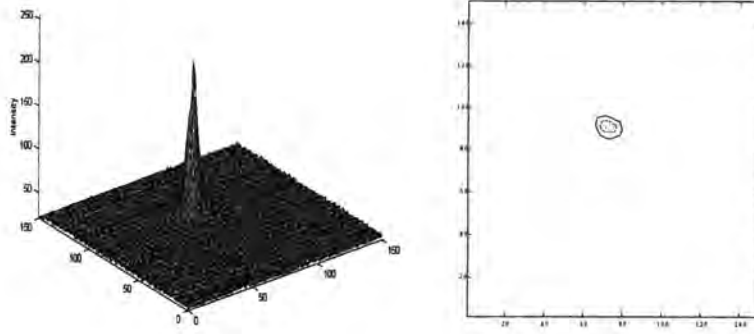
f) PSF after correction for mode 6. MF = 0.4759, rms. error = 0.078, SR = 0.80.
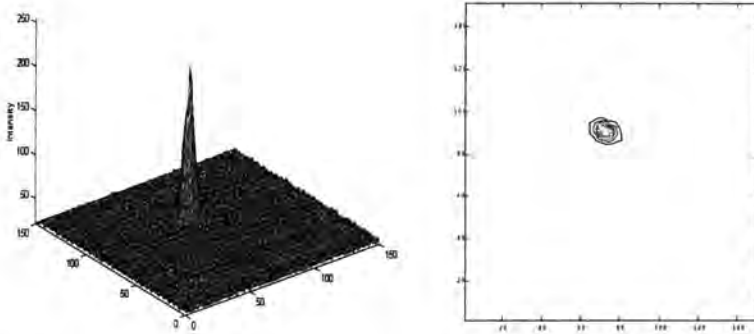
g) PSF after correction for mode 7. MF = 0.4760, rms. error = 0.078, SR = 0.80.
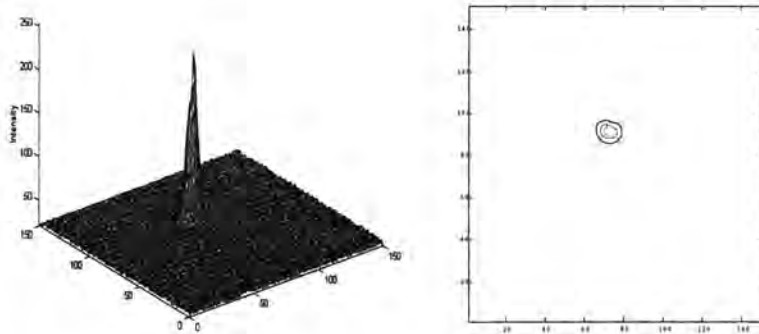
h) PSF after correction for mode 8. MF = 0.7979, rms. error = 0.058, SR = 0.87.
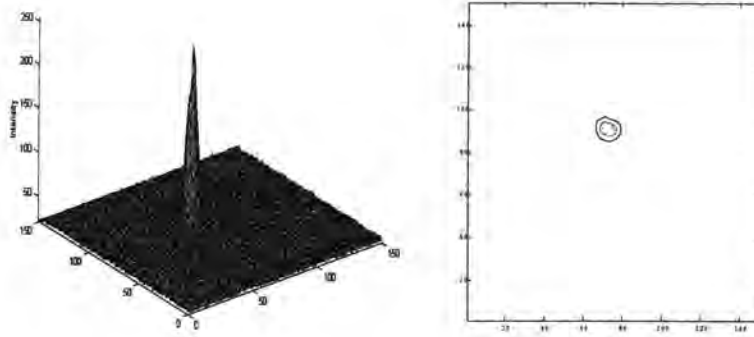
i) PSF after correction for mode 9. MF = 0.4802, rms. error = 0.058, SR = 0.88.
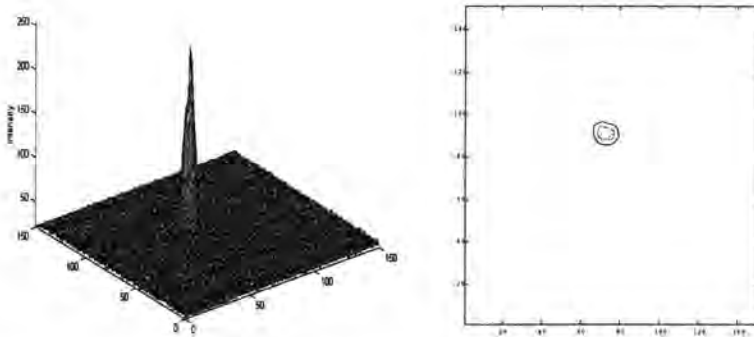
j) PSF after correction for mode 10. MF = 0.4808, rms. error = 0.053, SR = 0.89.

Figure 5.9: The evolution of the correction for the first 10 Zernike modes.

The improvement in image quality is clearly apparent with approximately a 63% increase in the Strehl ratio after the first iteration. The second iteration gives a further 3% increase in the Strehl. The final PSF on a second cycling had the form shown in Fig. 5.10.

The aberrated PSF had a FWHM of 2.4" by 0.96", after correction the FWHM had decreased to 0.96" by 0.84".
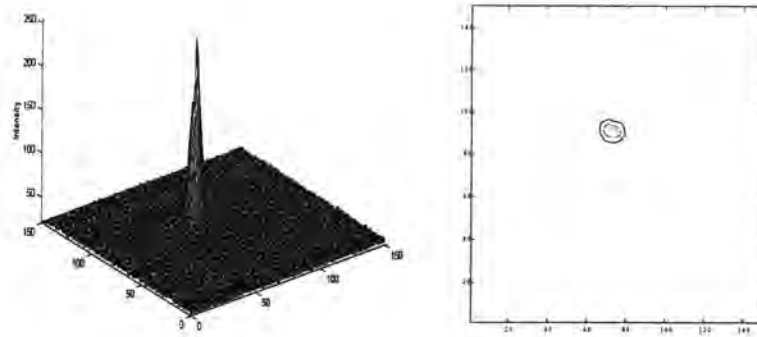
Figure 5.10: The PSF after the second iteration. MF = 0.4815, rms. error = 0.045, SR = 0.92.

Fig. 5.11 shows how the MF value varies over the two cycles. The MF can be observed to rise to a maximum then fall away over the period of one mode. The reason why there are more points for some modes than compared to others is due to the fact that sometimes high modal amplitudes were outside the experimental range of the LC-SLM and the MF was then set to zero. The required amplitude for defocus took up most of the correction range of the LC.
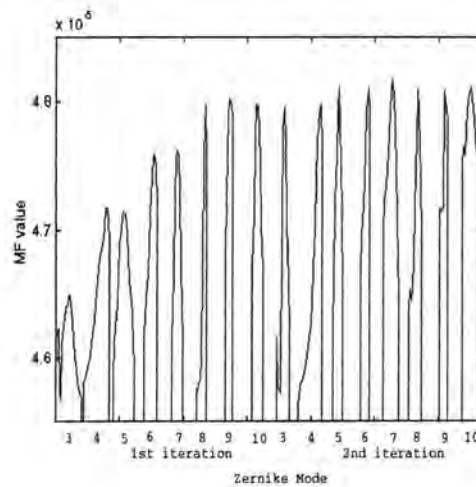
Figure 5.11: Evolution of the correction over two cycles.

Noise was a problem resulting in a trade off between sensitivity and noise reduction. Increasing the camera threshold results in a reduction in the effect of noise but may lead to an inaccurate determination of the MF when the PSF is severely blurred. A high modal amplitude can cause some of the camera pixels to have a value below that of the threshold value.

Results for I^3 and I^4

For the following results all experimental parameters were kept the same except for the MF. As can be seen the improvement is close to that observed under I^2. For brevity only the final state is given in each case. For I^3 the result is shown in Fig. 5.12.
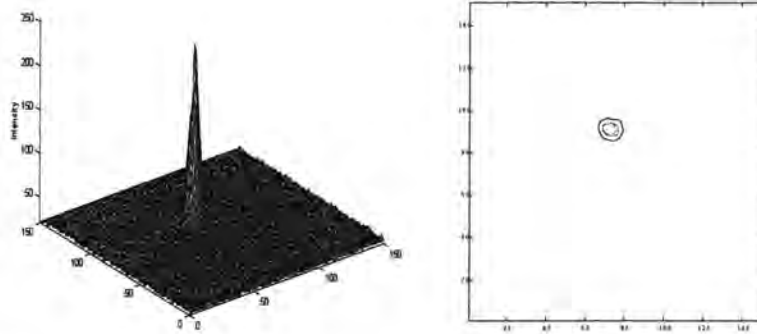
Figure 5.12: Result for modal correction under I^3. MF = 0.2968, rms. error = 0.054, SR = 0.89.

Similarly for I^4 the corrected PSF had the following form, Fig. 5.13. All results are for two complete cycles.
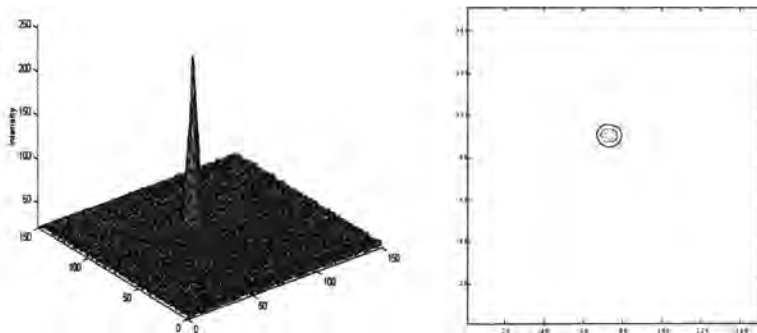
Figure 5.13: Correction for I^4. MF = 0.14973, rms. error = 0.057, SR = 0.87.

Result for $S_1 = I_{max}$

The experiment was repeated for $S_1 = I_{max}$. This MF proved to be noisier than previous ones. Only the PSF after correction is given, Fig. 5.14.
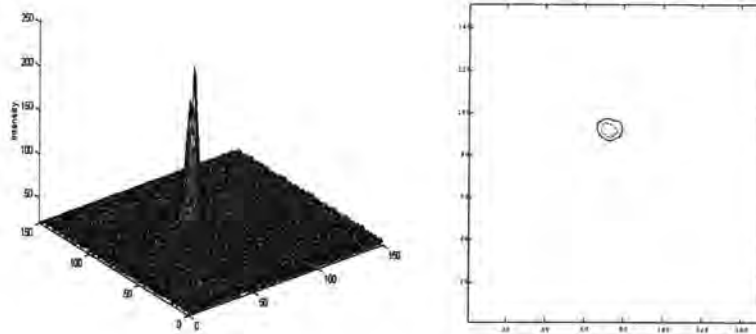
Figure 5.14: Result for correction under S_1. MF = 204, rms. error = 0.077, SR = 0.80.

Result for S_6 (bucket)

The same procedure again but this time with a 5 by 5 pixel bucket defined around the maximum intensity. The PSF after correction is given, Fig. 5.15.
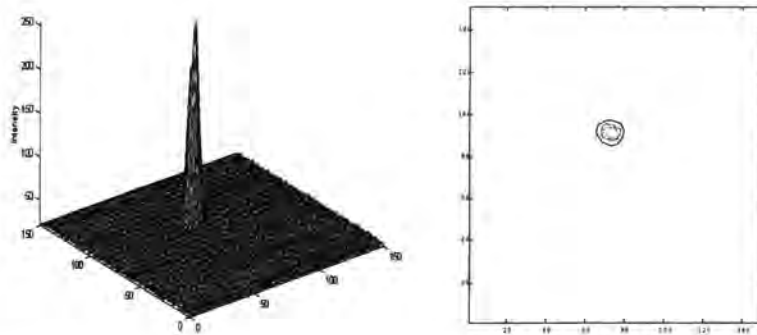
Figure 5.15: Result for correction under S_6. MF = 0.0378, rms. error = 0.027, SR = 0.93.

Choice of Merit Function

To check the validity of the experiment, the glass plate was tested in a Zygo interferometer. The measured Zygo modal amplitudes could then be compared with those determined in the experiment, the results are presented in Table 5.3.

Zernike mode	I	I^2	I^3	I^4	Bucket	Zygo amplitude
3	-0.2	-0.03	0	0	-0.2	-0.2
4	0.8	0.76	0.76	0.76	0.73	0.75
5	0.16	0.03	0	0	0.1	0.11
6	0.3	0.3	0.3	0.36	0.2	0.18
7	0	0	0	0	0.03	0.01
8	0.03	0.06	0.1	0.1	0	0.05
9	0	0	-0.13	-0.06	0	0
10	0	0	-0.06	-0.06	-0.06	0

Table 5.3: Modal amplitudes for each MF.

Table 5.4 is a summary of the final rms. and SRs for the various MFs. In addition the MFs S_3 and S_5 were tried but proved to be poor. Some improvement was observed but the system did not converge to a satisfactory final state.

Merit function	I	I^2	I^3	I^4	Bucket
Rms. error (waves)	0.077	0.045	0.054	0.057	0.027
Strehl ratio	0.8	0.92	0.89	0.87	0.93

Table 5.4: Residual rms. wavefront errors and Strehl ratios for each MF after two cycles.

5.3.3 Zonal results for the merit function I^2

Instead of writing a modal correction to the LC-SLM, the phase of an individual pixel was varied. This method proved to be very susceptible to noise. The change in MF of varying one LC-SLM pixel had much less effect than applying a modal correction. This can be explained through the use of a relatively insensitive camera. NOTE: the results were obtained with a different glass slide.

There is a slight improvement in the shape of the PSF although there is little increase in peak intensity. Fig. 5.16 shows the PSF before and after correction. Zonal correction was used in the work with the ELECTRA system - see Chapter 7.
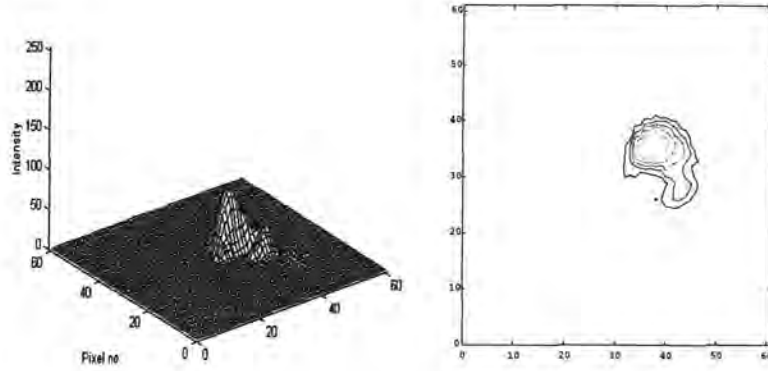
a) Initial, aberrated PSF. MF = 0.0072, SR = 0.28.
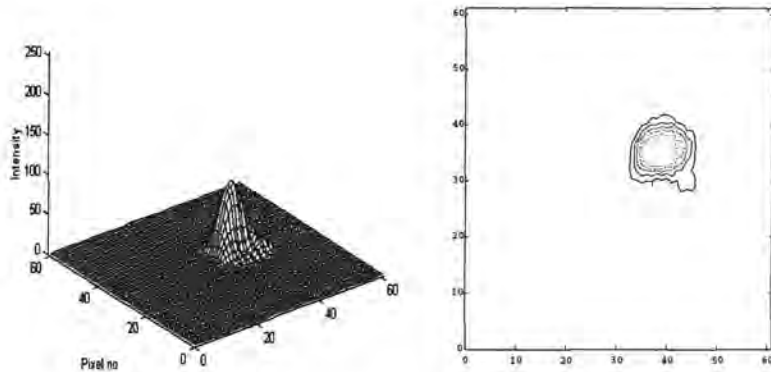
b) PSF after adjusting all the pixels. MF = 0.0087, SR = 0.32.

Figure 5.16: Results for zonal correction under the merit function, I^2.

5.4 Simulation of modal correction with an extended object

The logical progression was to then test the various metrics with an extended source. The system was modelled in more detail with the LC-SLM represented by an array of 69 hexagonal pixels.

Geometrically defining the LC-SLM is not a simple task. Instead, the array was generated by placing the Meadowlark device under the Zygo interferometer and then activating each of the pixels. This would show one of the pixels on a blank background, the whole pixelated array was then the summation of 69 such files and the result is shown in Fig. 5.17.

Each pixel was assigned a value from 1 to 69. A subroutine was then written which calculated the Zernike phase for each of the pixels, an array could then be
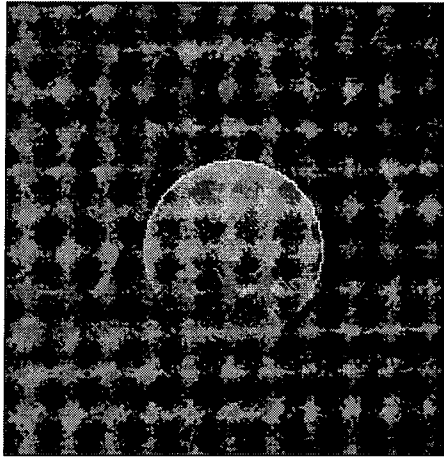
Figure 5.17: The pixelated Meadowlark LC-SLM array used in the extended source simulation.

formed which represented the simulated phase across the LC-SLM. The limiting experimental correcting range (approximately 2 waves) of the device was adhered to in the program.

The aberrated wavefront was again represented by the summation of the first 13 Zernike modes as used in the point source simulation. This time however, the correcting phase screen is not continuous but pixelated. As expected when the program was run with the Meadowlark phase screen the point source results were inferior to those obtained with a continuous, corrective phase screen.

The image used was part of the familiar BBC testcard chosen due to the fact of the varying spatial frequencies. Unfortunately however, the whole image was too large to be used in the program so only the central part was utilised. The image was approximately 200 pixels square and this was convolved with the PSF from the aperture phase screen with a diameter of around 50 pixels. Each Zernike mode was stepped through and the amplitude held at the optimum.

Effect of sample size

With an extended image the question arises as to what part of the image should the MF be determined over. It was found in this simulation that this was not an important factor. The only benefit of using a smaller sample size was the increase in the speed of MF computation.

5.4.1   Extended source results with the MF, S_4 with $n = 2$

For the following results, the metric used was S_4 with $n = 2$ summed over the whole image space. The initial object and diffraction limited image are shown in Fig. 5.18.

(a) The original image   (b) The diffraction limited image
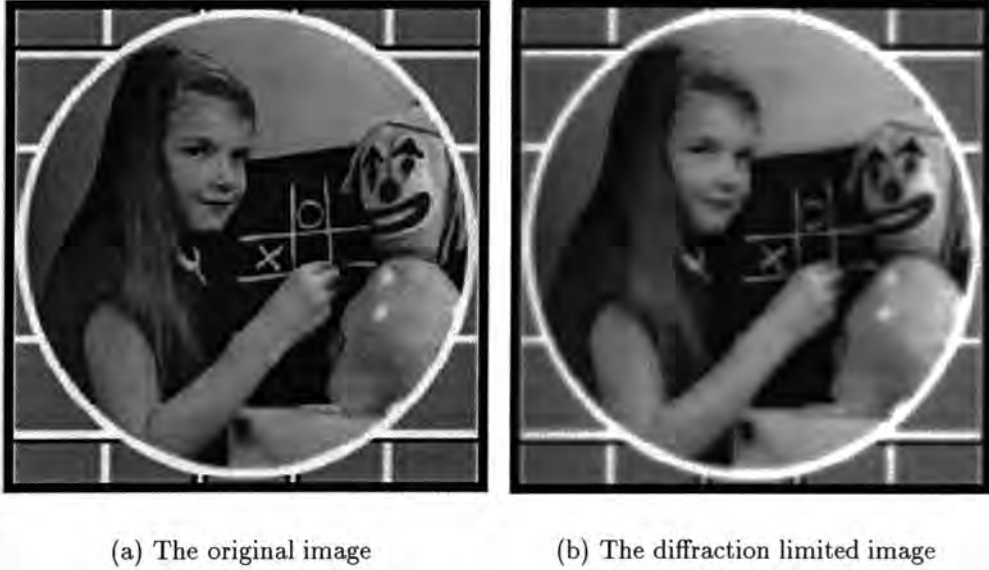
Figure 5.18: The original and diffraction limited images.

Fig. 5.19 shows the aberrated and corrected images. As can be observed there is a marked improvement in the image quality.

Table 5.5 shows the applied aberration and the corrected modal amplitudes. There will be some fitting error present now due to the discrete nature of the corrective phase screen. A second cycling only resulted in a modest improvement.

Zernike mode	3	4	5	6	7	8	9	10	11	12	13	14	15
Aberrated wave	0.5	-0.1	0.3	0.1	0	-0.2	-0.2	0	-0.1	0.1	0	-0.1	0
Corrected wave	0.3	-0.1	0.1	0.1	-0.1	-0.1	-0.1	0	0	0	0	0	0

Table 5.5: Aberrated and corrected amplitudes for the extended source (in terms of λ) after 2 cycles.

To get a more quantitative value for the improvement in the image quality, the power spectrum for each image was determined and the result is shown in Fig. 5.20.

The image power spectrum is given by the squared modulus of the image Fourier transform. To facilitate comparison between the images, the 2-dimensional power scene was reduced to the 1-dimensional case. This was achieved by averaging the power obtained in bands of spatial frequencies centered around the
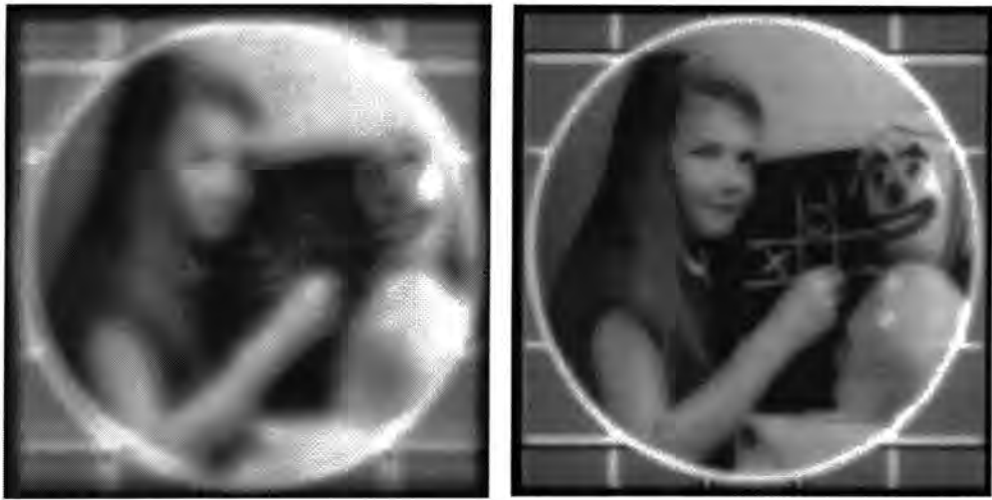
(a) The aberrated image   (b) The corrected image

Figure 5.19: The aberrated and corrected images.

azimuth. The spectra were normalised as described in the paper by Nill *et al.* [76]. As expected there is a reduction in the relative contributions to each spatial frequency when the aberration is introduced. After correction for 13 modes there is an improvement in the spatial frequency amplitudes of the corrected image. These are only be observed over a narrow range due to the frequency response of the LC-SLM.
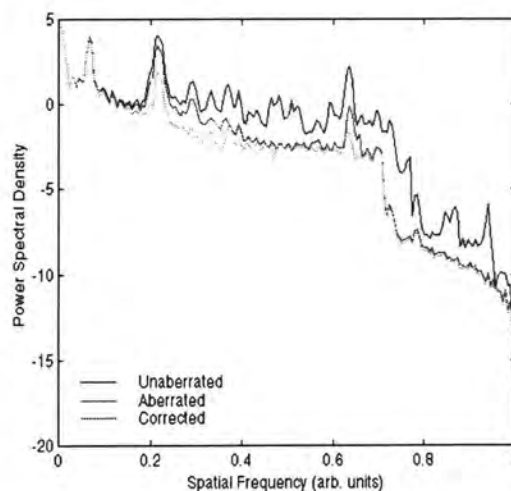
Figure 5.20: Spectral power density plots. The improvement over a limited range is clearly visible.

The initial and corrected pupils are shown in Figs. 5.21 and 5.22. The corrected pupil has a reduced phase variation, Fig. 5.21 with an rms. error in waves

of 0.17 compared to 0.31 for the initial aberrated case. All legends are in waves.
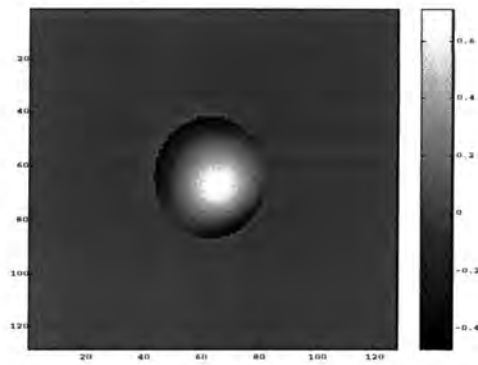
Figure 5.21: The initial pupil. Rms. error of 0.31λ.
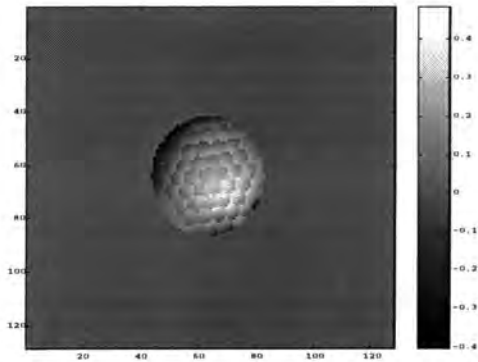
Figure 5.22: The corrected pupils. Rms. error of 0.17λ.

As can be seen in the form of Fig. 5.22 the pixelated array is apparent in corrected phase screen. The actual values of the LC-SLM is shown in Fig. 5.23.
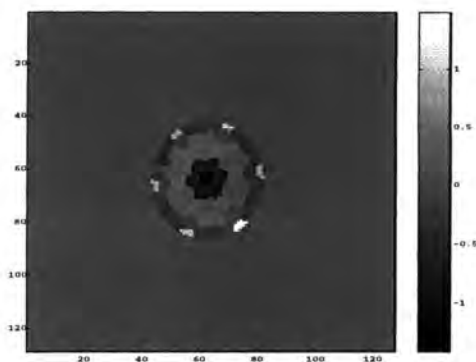
Figure 5.23: The final Meadowlark pixel configuration. Legend is in waves.

5.5 Experimental results with USAF test target

To see the effect of the correction on an extended source, a standard USAF test target was illuminated by a white light fed fibre bundle. Fig. 5.24 shows the central part of the image without the glass slide present. The target allows the determination of how known spatial frequencies are imaged through the system. As can be observed the spatial frequencies increase in roughly a spiral manner towards the centre with the value doubling each time after seven groups of 6 elements. Prior to taking these images the bias frame was subtracted and then divided by the image taken without the target in place i.e. flat fielded.
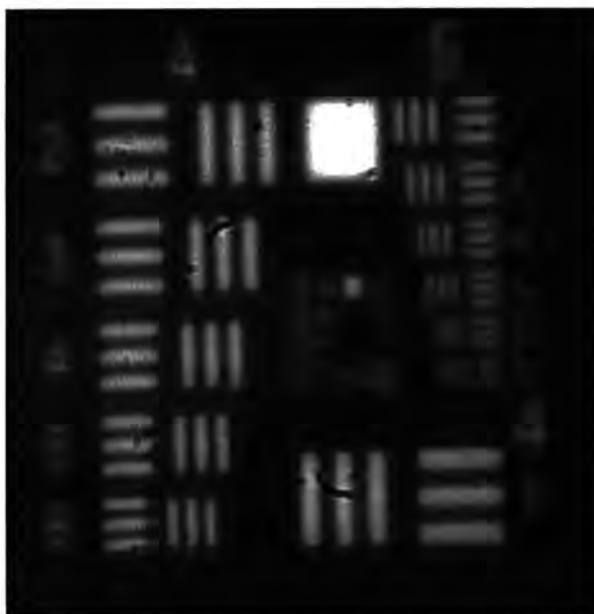
Figure 5.24: Initial USAF test target Frequencies just resolved up to approx. 70 cycles/mm.

The MF, S_4 with $n = 2$ was used for the images shown, and this was determined over the whole search space. The use of particular metrics for extended objects was not investigated. The same procedure was followed as detailed in the point source experiments. The aberrated image is shown in Fig. 5.25 with the corrected form in Fig. 5.26. As can be observed the blurring is substantially reduced.

Figure 5.25: The aberrated USAF target.
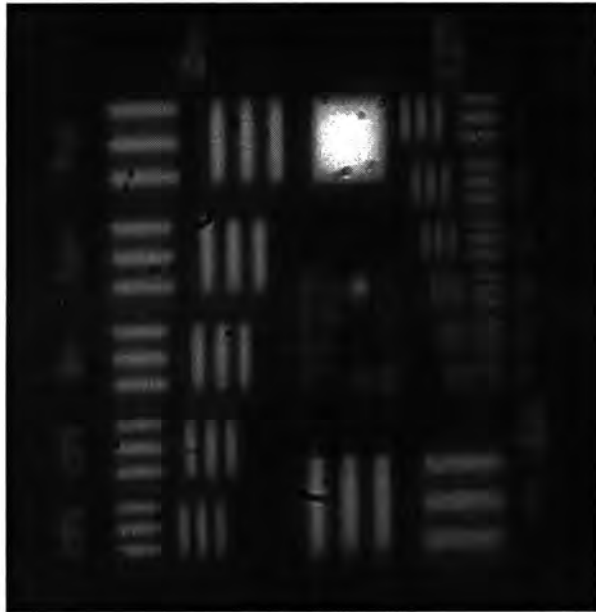
Figure 5.26: The final image after the correction of the first 13 Zernike modes.

The cutoff frequency, ν_c for the system is given by the Eq. 5.2

$$\nu_c = \frac{D}{f\lambda} \qquad (5.2)$$

where the symbols have their standard meaning.

For the experimental system described ν_c had a value of 75 cycles/mm. Although this is not clear in Fig. 5.24, the group (6,2) was just resolvable which corresponds to the frequency of 71.8 cycles per mm indicating that the system is well aligned.

As described for the theoretical case the power spectrum was measured. Fig. 5.27 shows the improvement in the performance of the system before and after correction. The system behaved as expected with improvement only being observed up to approx. 10 cycles/mm (the frequency response of the Meadowlark). The LC-SLM has a limited spatial frequency response and essentially removes the low frequency blur.
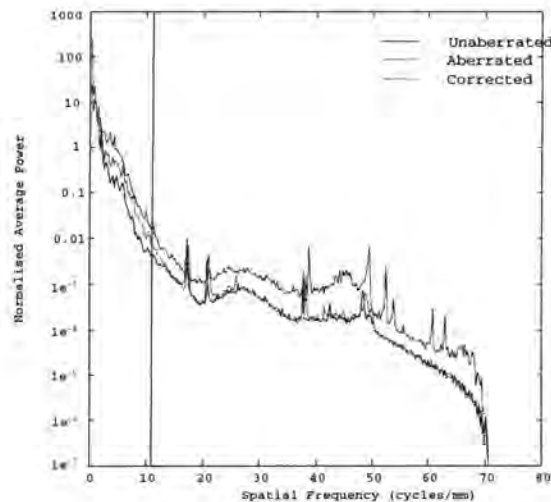
Figure 5.27: The improvement in the modulation depth before and after correction. The vertical line marks the limit of the LC-SLM correction.

5.6 Conclusion

It has been shown that significant system performance can be achieved through the use of a simple image sharpening set-up. Diffraction limited imaging was obtained using the LC-SLM when viewing a point source through an aberrating phase screen.

When used with an extended object, improvement was observed up to the limiting spatial frequency response of the LC pixels. The use of different image

metrics for extended objects was not investigated, some measure of the MTF or power spectrum may prove useful. For both schemes the cycle time was of the order of 90 seconds.

The extension to quasi-static image sharpening is possible providing the measurement and application of the correction can be determined at the required bandwidth.

The next chapter discusses the use of search algorithms needed for systems where the number of degrees of freedom becomes very large.

Chapter 6

Mirror alignment using image sharpening

6.1   Introduction

This chapter describes the simulation of various search strategies and metrics in the correction of the non-common path error (NCPE) in the ELECTRA system. From Fig. 6.3 it can be seen that after the beamsplitter (directly behind Flat 2) the light travels along two paths. One is to the WFS and the other to the science camera. It is the difference in the errors in these two arms that are uncorrected for in the normal operation of the AO system and are termed the NCPE. The correction techniques described will not allow for real-time atmospheric correction but will provide a correction of any quasi-static system aberrations present. It is envisaged that such a correction would only be required a few times during a night's observation at a telescope site. In general, the mirror will be found in an initial misaligned state and such a correction would configure the deformable mirror to correct for any system misalignments in the science arm by providing a mirror offset. This chapter proceeds by detailing the ELECTRA system and gives both theoretical and results for alignment correction.

6.2   Overview of the ELECTRA system

The 76 element ELECTRA system [77] (*E*nhanced *L*ight *E*fficiency *C*ophasing *T*elescope *R*esolution *A*ctuator) is the successor to the prototype 6 element MAR-TINI system [78, 79]. The system is designed for the Nasmyth platform at the William Herschel Telescope (WHT) at La Palma. The number of degrees of freedom (76x3) was chosen such that it would provide a 15-40% Strehl Ratio (SR) at 500 nm in median seeing conditions. The mirror is unique in the fact that it

incorporates a strain gauge loop which linearises the actuator motion virtually eliminating the effects of hysteresis. The actual mirror segments can be seen within the circular aperture at the front of the apparatus, Fig 6.1. The strain gauge preamplifiers can be seen above the mirror.
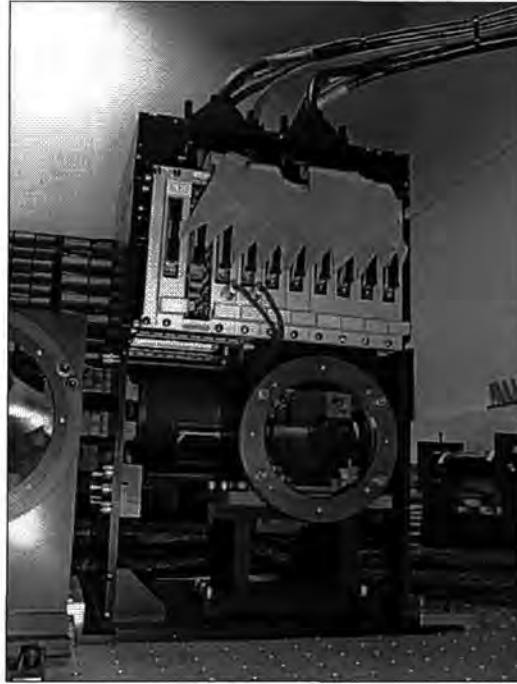
Figure 6.1: The ELECTRA mirror and housing.

The ELECTRA mirror was manufactured by the ThermoTrex Corporation and is segmented with the 76 elements arranged on a square array, each segment being 7.54 mm square with a separation of 0.08 mm giving an overall fill factor of 98%. The mirror segments, piezoelectric drives and backplate are shown in Fig. 6.2.
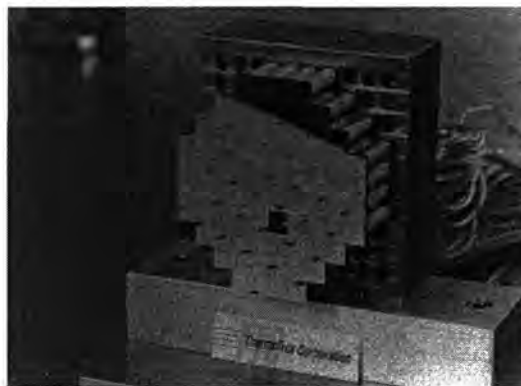
Figure 6.2: Close up of the ELECTRA segment arrangement.

The individual segments can each be driven in tip, tilt and piston. The piezo-

electric actuators provide 6 microns of throw with 2 microns being used to flatten the mirror. The surfaces are aluminium-coated optical grade silicon, flat to 10nm RMS. The optical arrangement used for a commissioning run at the WHT in July 1998 is shown in Fig. 6.3.

The ELECTRA layout shown can be broken down into two distinct parts. The first is the actual AO system which runs from the derotator via parabola 1, the segmented mirror (SM) and the through the hole in flat 2 to the beamsplitter. There are then the paths to the WFS and also to the CCD science camera. The other arm of the apparatus is the figure sensor shown by the dashed lines which uses a Twyman-Green interferometer to monitor the position of the mirror segments. The two parts are discussed separately.

- The AO system. The incoming starlight first passes through the derotator and parabola 1 collimates the incoming f/11 beam. This is then reflected off the SM and refocused by parabola 2. Just before focus the beam is separated into two paths, one to the WFS and the other to the science camera. This is achieved either by a 40-60% beamsplitter or through the use of an infrared/visible dichroic.

  The WFS arm consists of a 10x10 Adaptive Optics Associates microlens array, with a wavelength range of 0.4-0.8μm. Each spot from the lenslet array (one spot per mirror segment) is then mapped to an 8x8 pixel subarray on the EEV CCD-39 camera. Two sets of lenslet arrays are used, one of scale 0.36" per pixel (better tracking in poor seeing) or another at 0.27" per pixel (better centroiding).

  The path to the science camera consists of an IR doublet lens to form the f/55 beam required by the science camera.

- The Figure Sensing Arm. This consists of a folded Twyman-Green interferometer to monitor the state of the mirror. It lies off the main path and can be used at the same time the main system is running. Due to lack of bench space at the WHT it is unlikely that the interferometer will be incorporated into the final common user NAOMI system. Another example of this space limitation is the mounting of the strain gauge amplifiers above the mirror shown in Fig. 6.1.

Other instruments such as the fibre spectrograph TEIFU [80] and DAFI [81], a fibre fed interferometer are future additions to the ELECTRA instrument.
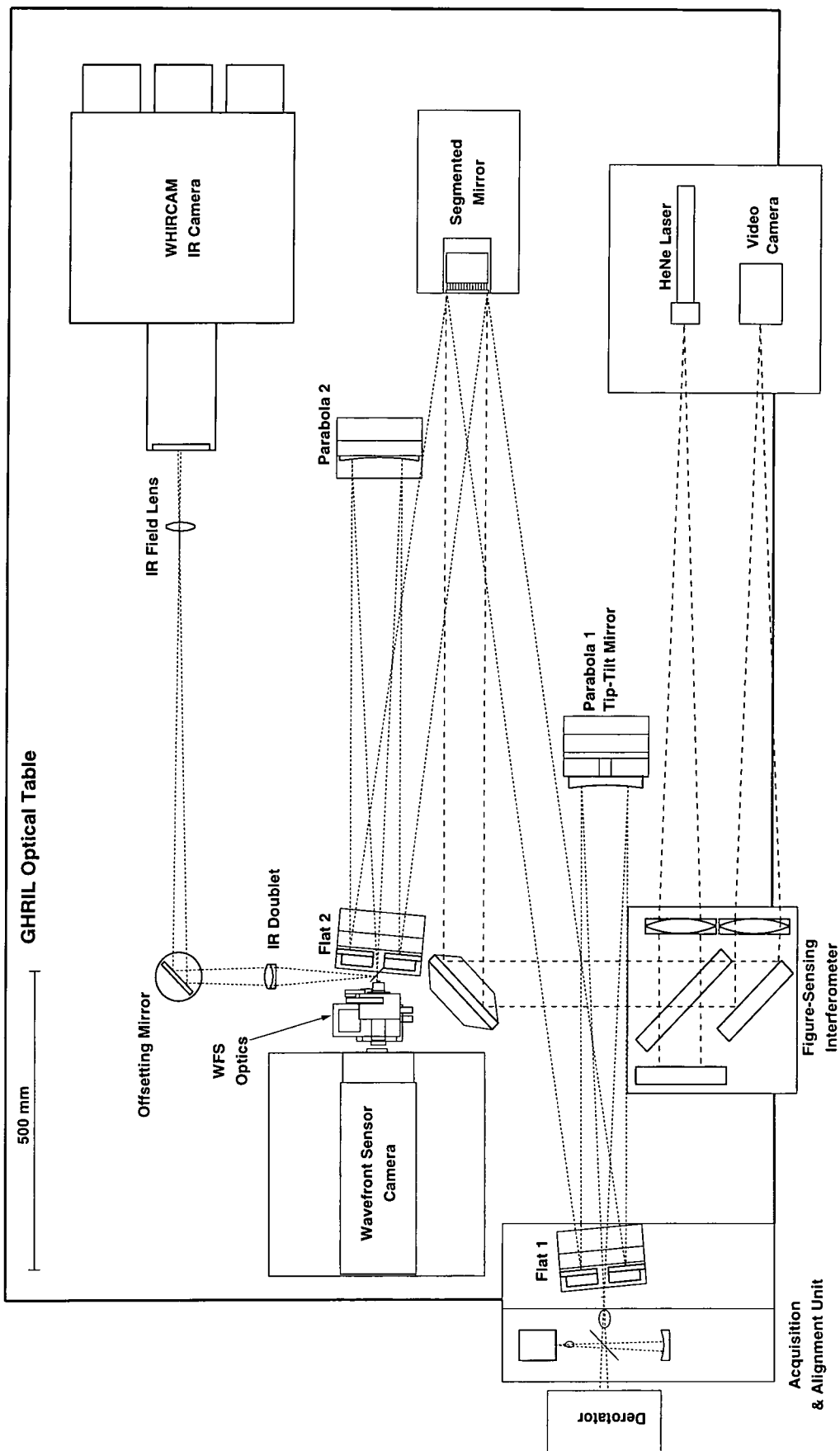
Figure 6.3: The ELECTRA layout used on the commissioning run at the WHT in July 1998.

6.3 Non-common path errors

One problem with all AO systems is that of NCPE. Acton in his paper [82] notes, that in good seeing conditions the corrected image was sometimes worse than an instantaneous image obtained without AO and puts this down to misalignments in the optics of the AO system itself. Such errors can be caused by several factors, for example, gravity or thermal stresses and in general these aberrations vary over a long time period. For space based systems, launch forces are a cause of misalignment and would require active correction.

The usual means of calibrating the WFS is to send a wavefront from the alignment source through the system and then take the positions of the lenslet spots to be the null case. Using this method does not allow for a measure of the actual system errors, any atmospheric wavefront correction is then measured with respect to this. Another upshot is that any NCPE in the science camera arm is also not calibrated for.

As the image at the science camera is of principal interest, a superior way is to calibrate the system with respect to this rather than use the null case described before. This chapter and the subsequent one describe a means whereby the science camera PSF due to the alignment wavefront is optimised by applying a correction using the SM. These Shack-Hartmann spot positions are then taken as the null case.

Acton [82] describes a technique, essentially a depth first search technique, whereby the centroid of the image at the science camera is determined and the individual segments of the mirror adjusted so that their Airy patterns fall exactly on this centroid. Such a technique will adjust the tilt of each of the mirror segments but will not correct for piston. Another problem is that this is not applicable to deformable mirrors due to the fact that individual portions of the mirror cannot be singled out.

Work on the Palomar 200" telescope [83] has shown that NCPE broadens the PSF by a factor of 10% over a timescale of 2 minutes. Most of this aberration is introduced due to gravitational effects as the AO system is attached to the telescope tube. Their solution is to position a laser fed optical fibre at the output camera and by use of a corner cube mounted near the steering mirror redirect the guide star to the improved reference provided by the laser. Such a system relies on the fact that the two paths followed by the beams are identical.

Work with ELECTRA has shown that the NCPE has a slower timescale, evolving typically over the period of about an hour leading to a broadening of the

K-band FWHM by a factor of 2-3. This is mainly due to temperature fluctuations and leads to astigmatism and higher order trefoil. Zadrozny [84] details how the magnitude of this aberration was such that it could not be corrected for in closed loop as it exceeded the range of a WFS subaperture.

The remainder of this chapter deals with correction of system errors by using measurements of the alignment source at the output science camera. The use of an image metric and a search algorithm which can iteratively offset the mirror to correct for quasi-static system misalignments is detailed.

6.4 Alignment of the ELECTRA mirror with laser light

The aim of this work is to provide an offset to the mirror which encompasses any misalignment in the science arm and as stated before this may need to be done several times during an observing run. To achieve good performance the mirror initially needs to be aligned so that the segments are cophased. Several methods have been tried. The Keck telescope on Mauna Kea, Hawaii, for example, has 36 segments which are aligned via 168 edge sensors [85]. Another method is to use the wave-front sensor to configure the mirror to alignment. At present, the ELECTRA figure is monitored using the Twyman-Green interferometer. However, this can only flatten to modulo λ as the light source used is monochromatic and also cannot be used for NCPE correction.

As a precursor to NCPE correction, various search strategies were simulated to test their ability to flatten an initially misaligned mirror. The only aberration present at this time being that due to the mirror. The incident wavefront was assumed planar with no aberration contribution by the science camera optics. Although the temporal aspects of the correction are not demanding, valuable observation time does not want to be wasted taking out system errors. The number of iterations, ability to find minima etc. for various strategies are therefore important considerations and require investigation.

ELECTRA mirror alignment

The simulation was constructed as follows. The initial wavefront was simulated as a 2-dimensional array. The incident wavefront in terms of this work was assumed flat. This was then combined with a pupil function to produce an output array with zeros if a part of the wavefront lay outside the pupil - see Fig. 6.4. In practice, the central 4 elements are not used, however, early in this simulation they are

included. The mirror was described by a 2-dimensional array subdivided into individual mirror segments. This array was then subtracted from the incident wavefront to produce the reflected matrix. Any science arm aberrations could then be simulated as another array and added to the reflected one. The total was then converted to a complex wavefront and Fourier transformed to give the resultant PSF.
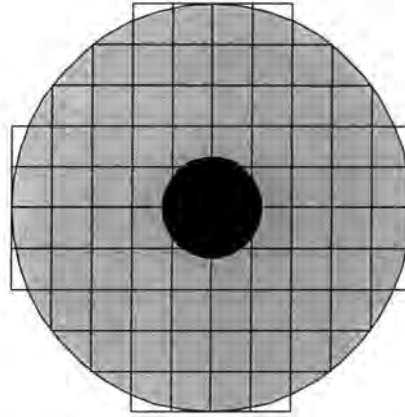
Figure 6.4: Image of the segmented mirror on the incident wavefront.

A MF (such as those described in Section 3.4) was used to characterise the image and a search algorithm implemented to optimise it's value. The value of the MF is, of course, directly related to the mirror figure. If the tip/tilt and piston values are used as input parameters to the search algorithm then a MF can be determined based purely on the image plane intensity data. Fig. 6.5 shows the basic arrangement under consideration.

The goal of mirror alignment is to produce a focal plane PSF that is as close to the theoretical Airy pattern as possible. Several parameters deserve careful consideration, namely:

- Choice of MF. It may be desirable to have a change of MF during the procedure. For example, a MF which quickly produces an improvement then a further MF which further refines the shape of the PSF.

- Choice of search algorithm (SA). Can the SA find the global minimum of the system? Computation time and number of iterations are important factors.

- Effect of stuck or 'frozen' actuators is investigated and their effect on the overall process determined.

- The use of image plane information to remove low order tip and tilt.
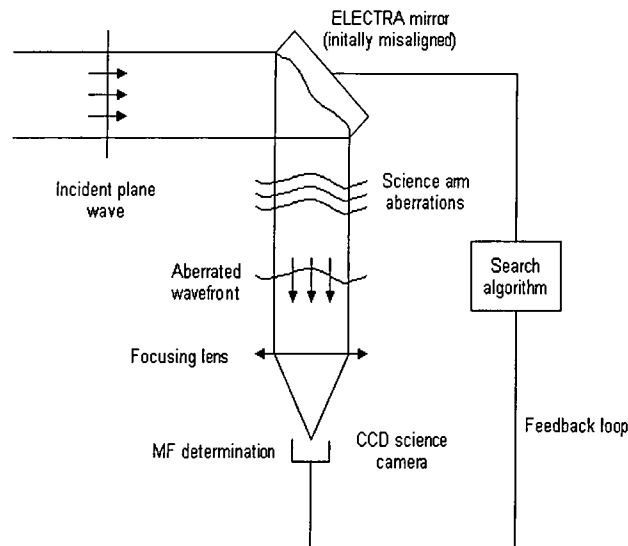
Figure 6.5: The ELECTRA image sharpening arrangement under consideration.

The following simulations are just concerned with initial mirror flattening and tip/tilt compensation in order to investigate the relative merits of various search strategies/MF combinations. The simplex algorithm was tried first and is therefore more detailed than for other search strategies. Where the SAs differ in operation will be detailed and investigated.

6.4.1 Results using the downhill simplex method

Mehta *et al.* [86, 87, 88] first used a simplex algorithm in conjunction with a MF to provide adaptive correction in the presence of both static and dynamic turbulence. Their motivation was for the technique to provide the full atmospheric adaptive correction i.e. to take the place of the 'standard' wavefront sensor. They used the standard definition of SR and 'energy in a bucket' MFs as their measures of image quality.

The simplex algorithm requires several arrays as input. Namely, a 2-dimensional array of $N+1$ by N where N is the number of degrees of freedom. For the full ELECTRA mirror of 76 segments, N is 228 and each of the $N+1$ rows of the matrix correspond to a vertex of the initial simplex. Each vertex of the simplex being a mirror array. Another required 1-dimensional array is the MF evaluation for each of the $N+1$ random mirror arrays. One more input parameter needed is the function tolerance (FTOL). The process can be terminated either by exiting after a fixed number of iterations or by the fact that the improvement in the MF is less than FTOL.

In an experimental situation, the initial simplex array would be determined by taking the initial piezo drive voltages and then adding a random perturbation voltage. The reason for adding a small voltage is to perturb the starting simplex out of any local minima. In the simulation however, the randomly generated phase of each segment is equivalent to the experimental voltages.

Dependance on the function tolerance - FTOL

The following graph Fig. 6.6 shows the number of iterations required for a given number of mirror segments for various values of FTOL. The initial mirror was generated from a set of random numbers scaled to give an average rms. error (in waves unless otherwise stated) of 0.19 corresponding to a SR of approximately 20% (from Eq. 3.11). As expected a tighter FTOL results in a better correction but requires more iterations. The MF used in this case was the SR, taking the intensity at the centre of the image plane. Note that initially the incident light was assumed to be monochromatic and hence mirror flattening to only modulo λ is possible.
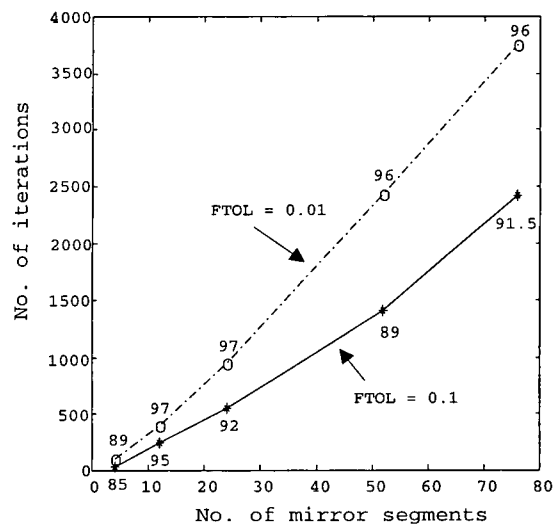
Figure 6.6: Number of iterations required for varying numbers of mirror segments under simplex minimisation. The figures against the data points correspond to the corrected SR.

Fig. 6.6 highlights the need for careful consideration of FTOL. Especially when dealing with large segmented arrays where the contribution of a segment to the form of the overall PSF is reduced, the number of iterations required is considerably increased. As convergence speed is an important consideration a careful choice for the function tolerance is required.

Choice of initial simplex

Another critical parameter is the choice of the initial simplex. As stated before, if this is too small then the algorithm may simply think that the minimum has been reached and collapses around this. Conversely, if the simplex is too large then the probability of falling into a false minimum is increased. For systems with a large number of DoF the choice is essentially arbitrary. For example, if nothing is known about the mirror state then the initial perturbations should be generated using a flat mirror. If it was suspected that the mirror had a higher piston misalignment then better performance might be achieved when the piston perturbation coefficient is made larger, although the actual scale is still important. This dependance is shown in Fig. 6.7. The full mirror array of 76 segments is used for an FTOL of 0.05 with initial SRs of approximately 0.10 and 0.20. Tip, tilt and piston were given equal weighting in the simplex generation.

(a) Final Strehl Ratio

(b) Required iterations
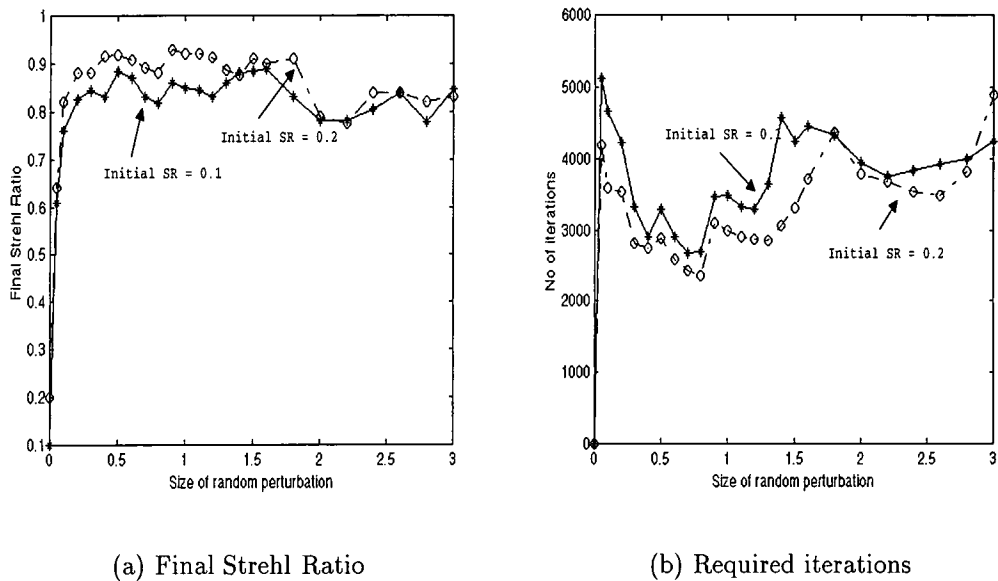
Figure 6.7: Dependance of final state against size of the perturbations applied to the initial simplex.

The ordinate axis is the scaling factor (arbitrary units) applied to the random number generator in the C code, to give a value up to one wave. The higher the scaling factor, the larger the perturbation. If the initial perturbation is very small (< 0.05) then wherever the simplex looks the improvement is less than FTOL and the program exits. If the scale is increased then although the program may be correcting even for small perturbations, the rate at which it does so is very slow due to the small size of the simplex. A small simplex implies that the initial trial deformations will also be small. The simplex will tend very slowly towards

a solution requiring many iterations.

It can be seen that there is an optimum perturbation size of approximately 0.8. For this value of the scaling factor the SR is close to the maximum and the number of iterations required a minima. For large simplices the performance decays slightly.

The use of the intensity median to take out low order global aberrations of tip and tilt is discussed in a later section.

Mirror flattening and the choice of MF

In the first simulation the misaligned mirror was corrected using several different MFs. The FTOL was set at 0.01 with piston being the dominant source of mirror misalignment.

Figs. 6.8 shows the mirror figure and PSFs before and after correction respectively with the SR at the centre of the image plane being used as the MF. The correction wavelength was 1 micron with a mirror rms. $=0.129\lambda$ corresponding to a SR$=0.07$.

As can be observed from Fig. 6.8.c there are two segments with half integer wavelength piston errors. Such a displacement is undetectable in the far field and will always be a problem when the correction is performed at one wavelength. For highly misaligned mirrors the simplex deformations may be such that a segment is moved to $\pm\lambda/2$. Using a longer wavelength will get around this problem but this wavelength must be compatible with the installed science camera. The modulo λ piston error was only observed when the reflected wavefront was approximately greater than 0.258 waves rms. - refer to Table 6.2.
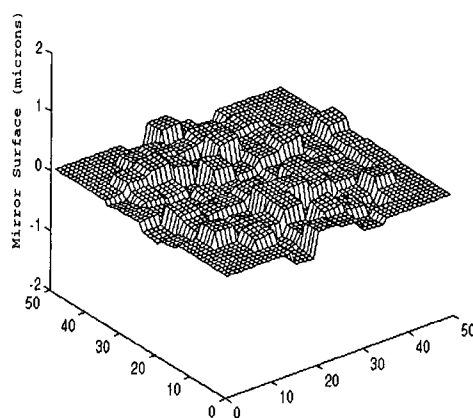
(a) Initial mirror figure
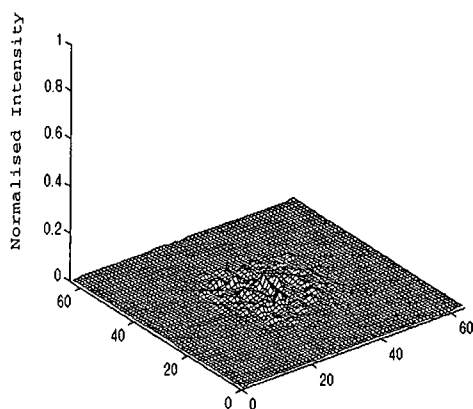
(b) Resultant PSF. Rms.=0.124, SR=7%
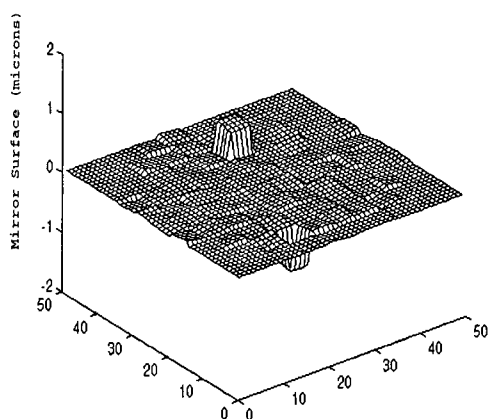
(c) Corrected mirror figure
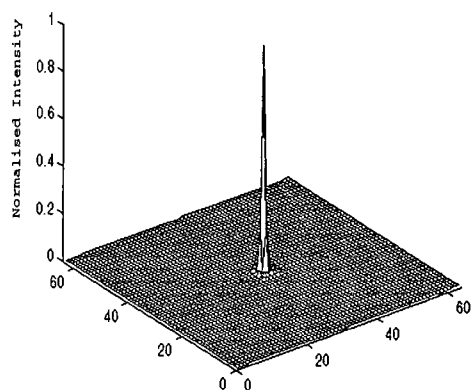
(d) Final PSF. Rms.=0.08, SR=95%

Figure 6.8: Initial and corrected mirror figure and corresponding PSFs. The final mirror has an rms. of 0.081λ and the SR=0.95.

Fig. 6.9 shows the evolution of the correction. The 'bottlenecks' on the graph are due to a multi-dimensional contraction around the best point, as described in Section 4.4.1. The initial oscillations start large but decrease as the simplex tends towards the optimal solution. Note that the rms. error decreases to a minimum and then increases slightly. This is due to the racking of the two modulo λ piston segments.

It should be noted that the SR can be defined in one of two ways, either by monitoring the intensity at the centre of the image plane or by using the
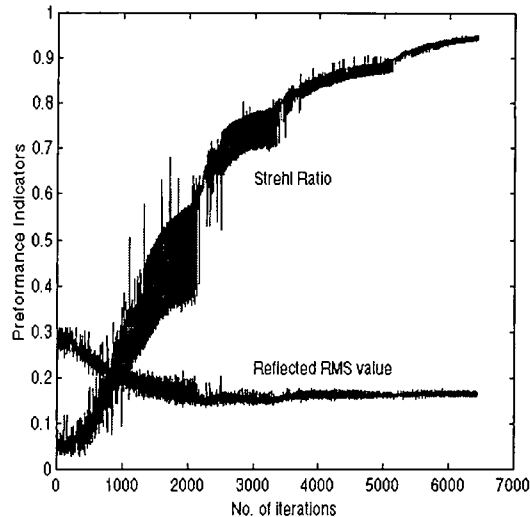
Figure 6.9: Evolution of the Strehl Ratio correction plus rms. error.

maximum intensity anywhere in the field. The second approach has the effect of making the correction insensitive to any beam jitter.

Table 6.1 compares the performance of different MFs. For all cases the initial conditions were the same as described for Fig. 6.8.

Merit Function	*Final rms. error*	*Final SR*	*No. of Iterations*
SR (centre)	0.162	0.95	6435
SR (anywhere)	0.336	0.920	6879
Bucket - 3 x 3	0.378	0.884	7914
" " - 5 x 5	0.275	0.881	6910
" " - 7 x 7	0.237	0.718	8875
I^2	0.317	0.834	8412
I^3	0.307	0.907	8145
I^4	0.309	0.917	10008
-I ln(I)	0.285	0.901	12314

Table 6.1: Comparison of different MFs. Same initial conditions without nudging.

With the exception of the SR at the centre, all the other MFs resulted in a mirror surface with a global tilt which explains the high values for the rms. errors. When the maximum intensity was monitored, the MFs except for SR (centre) were observed to lock onto the peak intensity. If this was not at the centre of the image plane then a global tilt was observed in the final mirror state. The 'bucket' MFs were defined about the peak intensity anywhere in the image plane.

Effect of the initial mirror state and the use of 'nudges'

When the simplex algorithm initially converges it is sometimes useful to give the simplex a 'nudge'. A nudge consists of applying small random perturbations to the best solution found. The effect of this was to knock the simplex out of a potential local minimum. Such a nudge will not be expensive in computation time as the simplex has already converged. It was shown that for mirrors in an initial, highly misaligned state such nudges proved beneficial. The SR (centre) was used both before and after the nudge. The same initial conditions were applied as in the previous example, Fig. 6.8. The FTOL value was set to 0.01 and the simplex nudged when it first converged. Fig. 6.10 shows the evolution of the correction with the number of iterations. Reducing the FTOL is shown to indicate the usefulness of a system nudge.

(a) FTOL = 0.001 with no nudges   (b) FTOL = 0.01 with one nudge
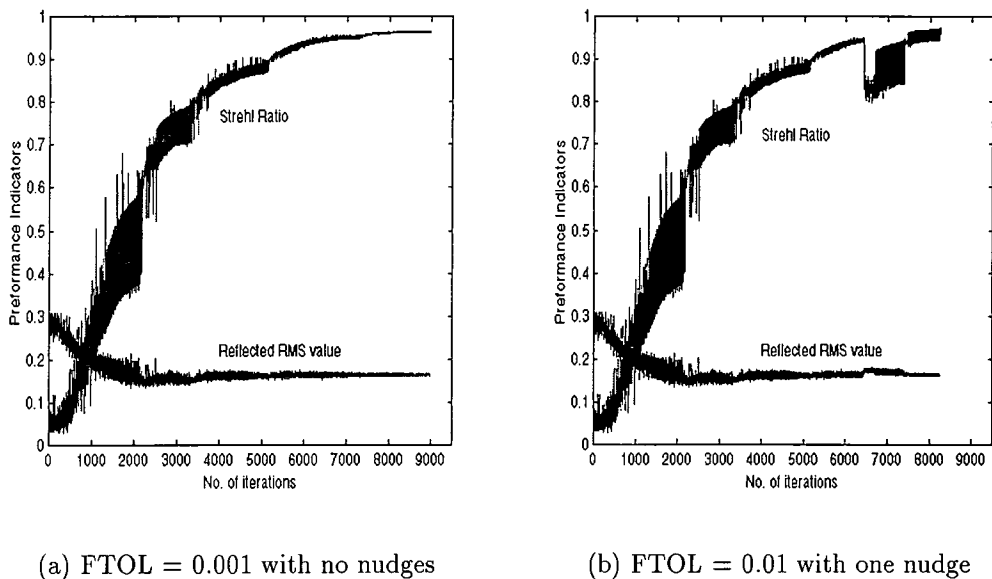
Figure 6.10: The effect of nudging the converged simplex.

It can be seen the use of nudges (shown after 6500 iterations on 6.10.b) is highly beneficial. For FTOL = 0.001 the final SR was 0.965. With FTOL = 0.01 the resultant SR was only slightly better at 0.972 but achieved with approximately 800 fewer iterations. Instead of letting the simplex creep towards a better solution with a tighter FTOL, a better scheme is to periodically nudge the simplex. This nudging could be preformed when the simplex converges or after a set number of iterations.

Table 6.2 shows how the final correction varies with different initial conditions. The starting simplex was made large enough for optimum convergence with FTOL

= 0.01. Again the SR at the centre of the image plane was used as the MF. This would allow elimination of the global tip/tilt allowing concentration on the piston error. The rms. errors given are for the reflected wavefront not the mirror surface.

Initial RMS error	*Initial SR (intensity)*	*SR - pre-nudge*	*SR - post-nudge*	*Final RMS error*	*No. of iterations*
0.053	0.892	0.988	0.988	0.017	3755
0.106	0.635	0.978	0.981	0.022	4465
0.142	0.447	0.969	0.976	0.026	4910
0.195	0.189	0.954	0.971	0.027	5996
0.258	0.071	0.950	0.972	0.162 *	8243
0.302	0.026	0.897	0.923	0.245 *	8434
0.348	0.008	0.921	0.966	0.288 *	9567

Table 6.2: Dependance of final solution on the size of the initial mirror deformations (* denotes modulo λ piston error).

Nudging the system when the initial misalignment is small does not result in any improvement, however, for higher rms. values the simplex has a greater probability of falling into a local minimum and the nudge is needed to 'push' it out. When the initial misalignment is very large, several nudges may be required as the simplex continually falls into a minimum. For highly aberrated initial states there were several segments which had $\lambda/2$ piston error in the final mirror figure.

As a check the simulation was performed using the rms. error as the MF. As expected, the corrected mirror figure did not contain any piston errors. In an experimental situation, however, such a measurement is not possible as it is essentially a measure of phase.

Switching of the Merit Function

Another possible improvement warranting investigation was a switch of MF after the nudge. The rationale being that using one MF to gain initial, quick convergence then the use of another to further refine the shape of the PSF might prove beneficial. The results of the simulations are shown in Fig. 6.11, the starting mirror had a reflected rms. of 0.234 with a SR of 0.08.

Using the SR (not centre) as the MF after the nudge proved the best in shaping the form of the final PSF, various other MFs were tested prior to the nudge. The best overall performance was observed when keeping the same MF in this case the SR. It can be argued that using a 3x3 pixel bucket defined around the maximum intensity has initial quicker convergence up to a SR of 0.4 but falls away after that. Other forms of the MF had slower initial convergence and poorer overall

performance. Bear in mind that in these simulations a point source is being used, extended source imaging may require different MFs and perform differently.
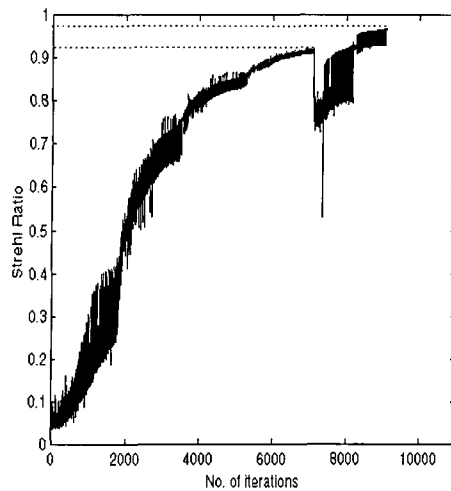
(a) SR (not centre) only
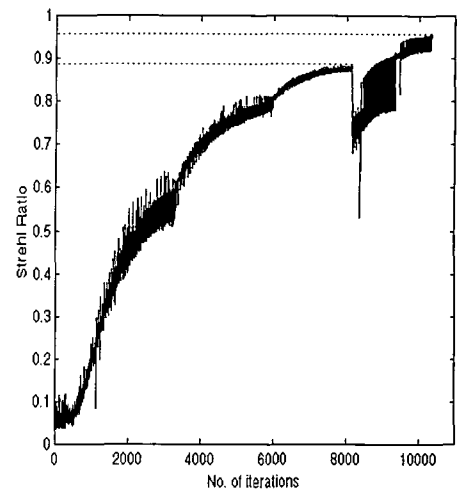
(b) 3x3 pixel bucket then SR
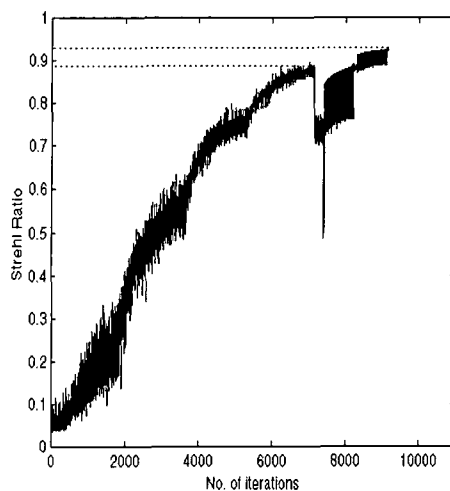
(c) 5x5 pixel bucket then SR
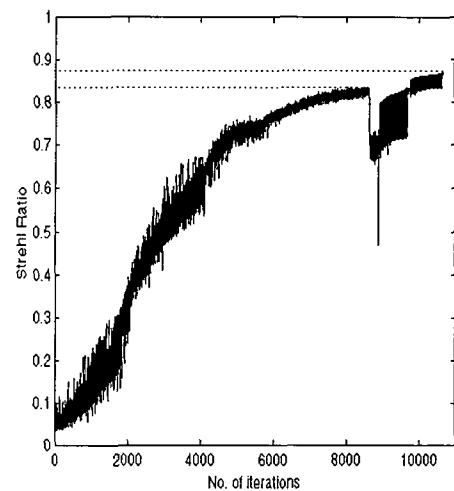
(d) I^2 then SR

Figure 6.11: The effect of a change in the MF after one nudge.

Use of the intensity median to correct for tip and tilt

With the previous simulations in this chapter, the initial simplex has been generated using the mirror values for tip, tilt and piston. The final desired mirror state being flat. The applied perturbations are then generated with respect to these initial values with possibly a bias towards a higher value for the piston coefficient.

One improvement that results in faster, improved convergence is that of using the intensity median. Just considering mirror aberrations alone, the peak intensity should lie on the optical axis for an aligned mirror. If the mirror deformations cause this peak to lie off the axis then the calculation of the image median can provide substantial benefits. If there was another form of global tip/tilt in the system then the determination of the median could be used to essentially bias the initial simplex.

The median is likened to the 'centre of gravity' of the image intensity plane. What it does is take out the low order global tip and tilt corrections. The value of the median can then be used to define generation conditions for the initial simplex that are sloped rather than flat. This has the effect of 'bypassing' the iterations needed for tip/tilt correction. For tip/tilt dominated system errors it has the added advantage of reducing the modulo λ error.

The median is calculated by summing across the rows in the image plane array and also down the columns. The two arrays are each processed individually by comparing the intensity sums either side of a starting point, the next point is then assessed. The point at which the intensity distribution either side is 50:50 is the median. The appropriate global low order correction can then be calculated and the resultant values for tip, tilt and piston used to generate the initial simplex.

In the simulation, a wavefront with tip/tilt aberration induced by the science arm is combined with the misaligned mirror, the simplex routine is then run with and without median correction and the results compared. Fig. 6.12 shows the tilted wavefront, the mirror surface and the resulting PSF. The initial maximum intensity was located at the point (35,30), the grid for the Fourier transform was 64x64 in dimension.

(a) Tilted wavefront, tip = 0.35λ, tilt = -0.2λ

(b) Mirror surface, rms. = 0.089λ

(c) Resultant PSF, SR (not centre) = 0.15
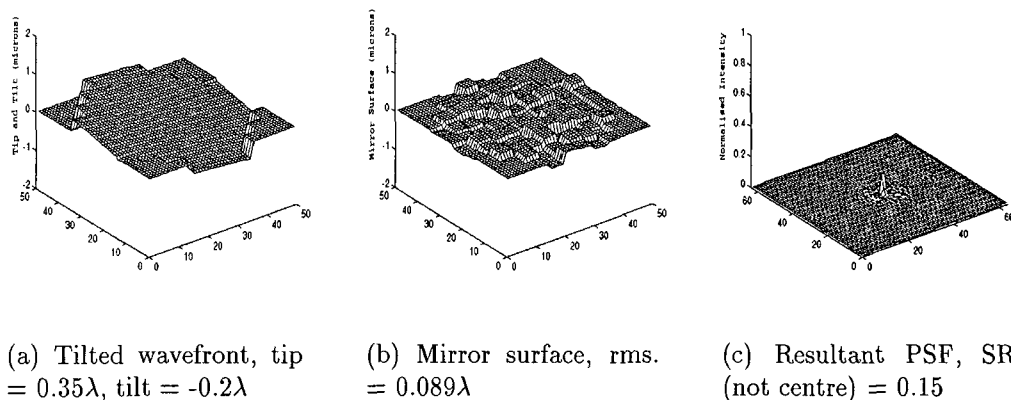
Figure 6.12: The tilted wavefront and mirror figure prior to median correction.

Without median correction

The first MF used was the SR anywhere in the image plane without the median correction. Using this MF resulted in a tilted, reflected wavefront with the mirror flattened as shown in Fig. 6.13. As can be seen, the rms. values for both the reflected wave and the mirror decrease. This is due to the improvement in the mirror figure while the overall global tip/tilt remains unchanged. Normally, it would be expected that the reflected rms. value would be twice that of the mirror rms. but it needs to be borne in mind that the resultant wavefront still has an overall tilt explaining the form of Fig. 6.13c

(a) Mirror surface, rms. = 0.034λ

(b) PSF, SR (not centre) = 0.96. Max Int at (35,30)

(c) Iteration cycle and the rms. errors
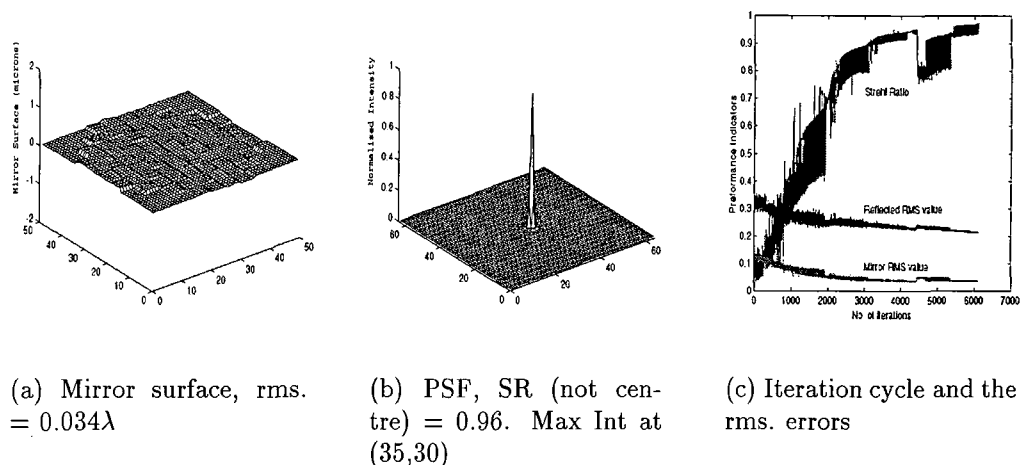
Figure 6.13: Final corrected state using the SR (not centre) without median correction.

There is a slight residual mirror tilt but this will not affect the final SR. The difference between the mirror and reflected rms. values is due to the initial, tilted wavefront. Using the SR defined anywhere in the image plane has the effect of flattening the mirror 'seeing through' any system tilts.

Next the SR (centre) was used and the results shown in Fig. 6.14. This MF forces the mirror to adopt the conjugate shape to the aberrated wavefront. There are several segments with modulo λ piston which explains the reflected rms. error. The mirror has a tilt which is half that of the incoming wavefront as expected. For this case, the reflected wavefront rms. is twice that of the mirror.

(a) Mirror surface, rms. = 0.151λ

(b) PSF, SR (centre) = 0.95. Max Int at (33,33)

(c) Iteration cycle and the rms. errors
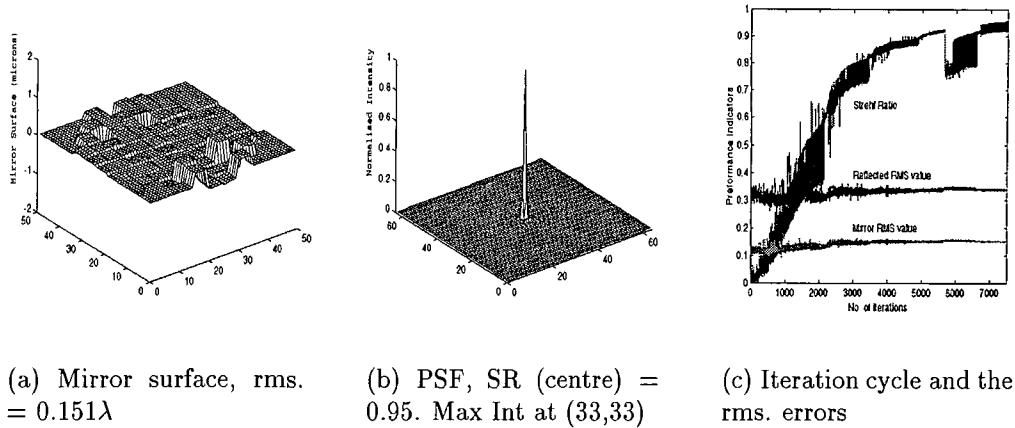
Figure 6.14: Final corrected state using SR defined at the centre of the image plane again without median correction.

With median correction

Finally the median correction was applied. This had the effect of reducing the number of iterations required and also avoided the problem of piston errors. As can be seen the final mirror surface is conjugate to the aberration.

(a) Mirror surface, rms. = 0.100λ

(b) PSF, SR (centre) = 0.97. Max Int at (33,33)

(c) Iteration cycle and the rms. errors
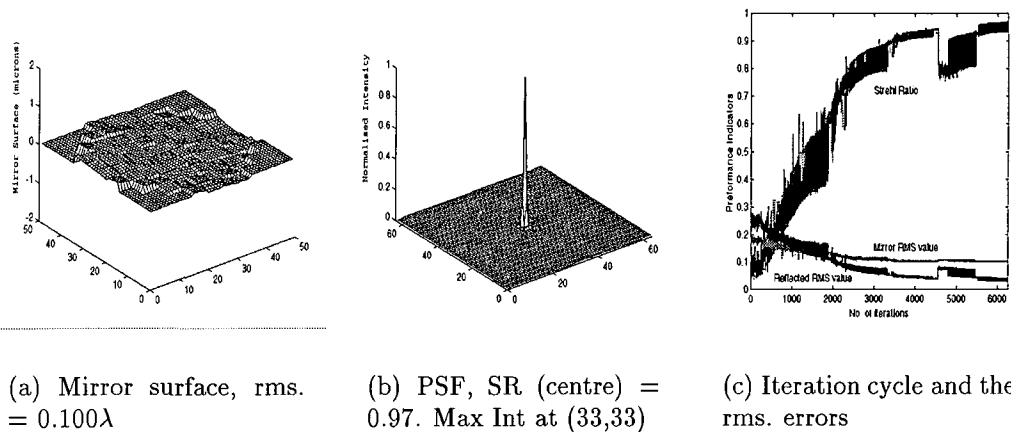
Figure 6.15: Final corrected state using SR defined anywhere in the image plane with median correction.

As can be observed the use of the median can prove very beneficial. For this case the mirror is conjugate with the incident wavefront resulting in a mirror rms. value which is greater than that of the reflected wavefront.

Effect of frozen actuators

Finally, the simplex algorithm was tested with a few of the actuators 'frozen' to mimic faulty or stuck elements. Also the central 4 segments were not used due to the obscuration by the secondary mirror. They were assumed flat in this simulation but will found in a random state in practice. The figure of the initial mirror and corresponding PSF are shown in Fig. 6.16 For all parts of this section the median was used to aid correction.

(a) Mirror surface, rms. = 0.08λ

(b) PSF, SR (centre) = 0.33
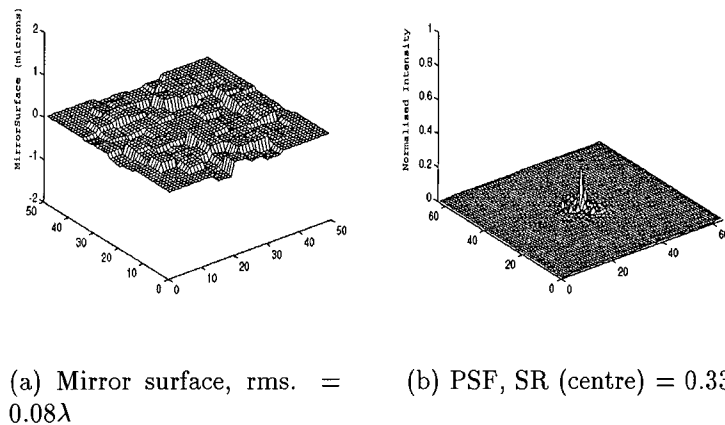
Figure 6.16: Initial mirror state and system PSF for the ELECTRA mirror with the 4 central segments taken out.

Fig. 6.17 shows the corrected state using the SR (anywhere) as the MF with the central 4 segments unused but with no frozen actuators. The system was not nudged when convergence occurred. As expected the initial SR is improved from 33% to 96%. The final reflected rms. value being twice that of the corrected mirror.

The next step was to include 3 frozen actuators. Three were chosen at random and were held at the tip, tilt and piston values given in Fig. 6.16a. Fig. 6.18 shows the corrected state for the mirror with 3 dead actuators but with no other form of system aberration present. As expected there is a degradation is the final image quality but the mirror does flatten despite the initial conditions.

(a) Mirror surface, rms. = 0.016λ

(b) PSF, SR not (centre) = 0.96

(c) Iteration cycle and the rms. error
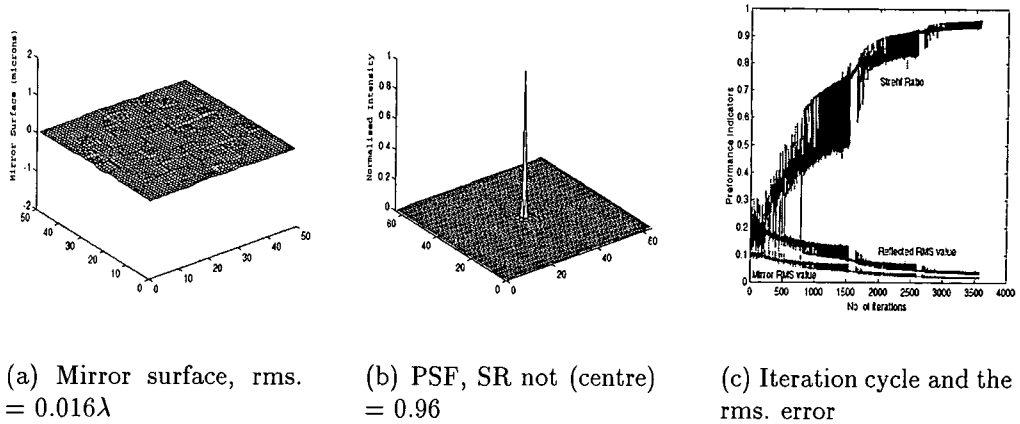
Figure 6.17: Final corrected state without frozen actuators or other aberrations present.

(a) Mirror surface, rms. = 0.056λ

(b) PSF, SR not (centre) = 0.86

(c) Iteration cycle and the rms. error
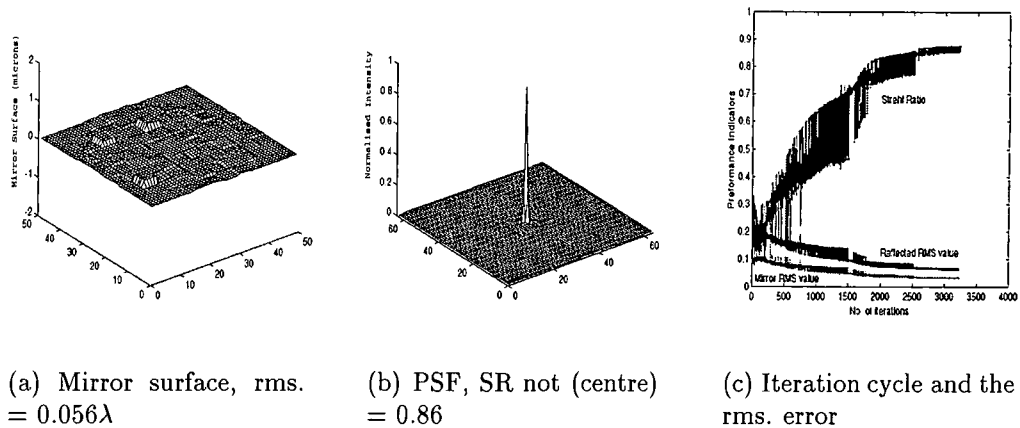
Figure 6.18: Final corrected state using SR defined anywhere in the image plane with frozen actuators.

The final figure, Fig. 6.19 is the final mirror state with a tip/tilt aberration introduced by the science camera optics. The final SR is worse but demonstrates that the mirror can still be offset even in the presence of frozen actuators. NOTE: Tip/tilt is different from previous figures.

(a) Mirror surface, rms. = 0.112λ

(b) PSF, SR not (centre) = 0.84

(c) Iteration cycle and the rms. error
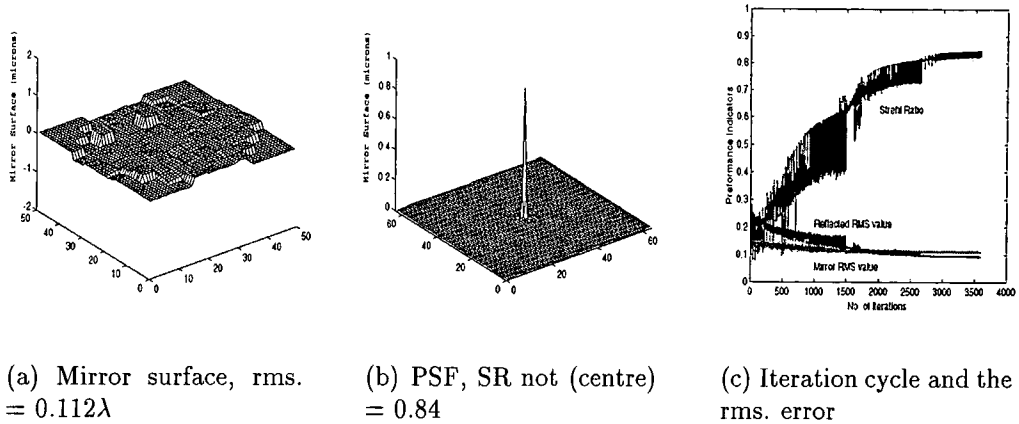
Figure 6.19: Final corrected state for 3 frozen actuators with a tilt aberration under median correction. Note, a different tip/tilt was used as compared to Fig. 6.12.

6.4.2 Results using simulated annealing

The next algorithm to be tested was that of simulated annealing. Ribak [89] used an annealing algorithm to perform piston only mirror correction but did resolve the modulo λ problem by use of a set of related wavelengths. Only a theoretical simulation was provided.

The one aspect of simulated annealing that is of particular attraction is its ability to find the minimum in the presence of many local minima. The MFs used in this work are well behaved functions with an easily locatable global minimum. The only form of a local minimum is due to the modulo λ piston error which independent of the algorithm used is untractable when correction is only performed at one wavelength. These forms of local minima due to the periodic nature of light have no effect on the far field intensity profile.

The performance of the simulated annealing algorithm is dependant on several factors, namely the annealing schedule and the time spent at each temperature. If the system is cooled slowly then the final state will be closer to the theoretical maximum but will take longer. Conversely, quick convergence will tend towards a poorer final state but in a shorter time. The algorithm was taken from Press *et al.* [74] and used a modified simplex routine to search the space at each temperature. With the well behaved nature of the MFs the simulated algorithm will have the quickest convergence when the system is 'quenched' i.e. cooled very quickly. The form of the algorithm is such that in this regime the algorithm performance mirrors that of the downhill simplex method.

It was expected that whatever the initial parameters used the final solutions will have similar Strehl Ratios, as with the simplex algorithm in Table 6.2. If the system is cooled slowly then a slight improvement would be expected purely due to the implicit increase on the number of MF evaluations and not due to any escapes from localised minima. The simulations were run with a view that the simulated annealing algorithm might be more robust when used on the actual ELECTRA apparatus. Any alignment source used in the experiment will not have the Dirac profile of the monochromatic source used in the simulations but will have a broader Lorentzian shape so there may be an effect due to the composite wavelengths.

As well as a change in the algorithm a variation in the method of searching the space was tried. Instead of treating the entire system of 76 mirrors in one routine, the ELECTRA surface was broken down into a series of concentric loops, and the algorithm run on each. Essentially the problem is treated as a series of smaller minimisations and will be described in more detail in Section 6.4.2.

The effect of the annealing schedule

The full mirror array of 76 segments was used. The initial starting temperature, T_0 was set to 1. It was found that for any values greater than this resulted in an increase in the required iterations. As the simplex is scaled proportional to this temperature, virtually all the trial points will be accepted. A significant percentage of the simulated annealing routine is therefore spent doing little more than a random walk. As $T_0 \to 0$, then the simulated annealing algorithm gives the same output as that of the downhill simplex method.

The standard annealing schedule was used as described by Levin [90] namely multiplication of the temperature by a factor α, $0 < \alpha < 1$. The number of iterations was increased from 2 through to 100, the results are shown in Tables 6.3, 6.4 and 6.5. The initial starting conditions gave a mirror with an rms. of 0.145λ corresponding to a SR = 0.07.

Fig. 6.20a shows the evolution for simulated annealing when the number of iterations was set to 2 per temperature drop with $\alpha = 0.99$. For the first 1750 iterations virtually every solution is accepted resulting in little overall improvement in the SR. If α is decreased to 0.9 then the probability of accepting every solution is decreased. Instead of meandering along, the improvement is much more rapid, Fig. 6.20b.

(a) Annealing evolution for $\alpha = 0.99$

(b) Evolution for $\alpha = 0.90$
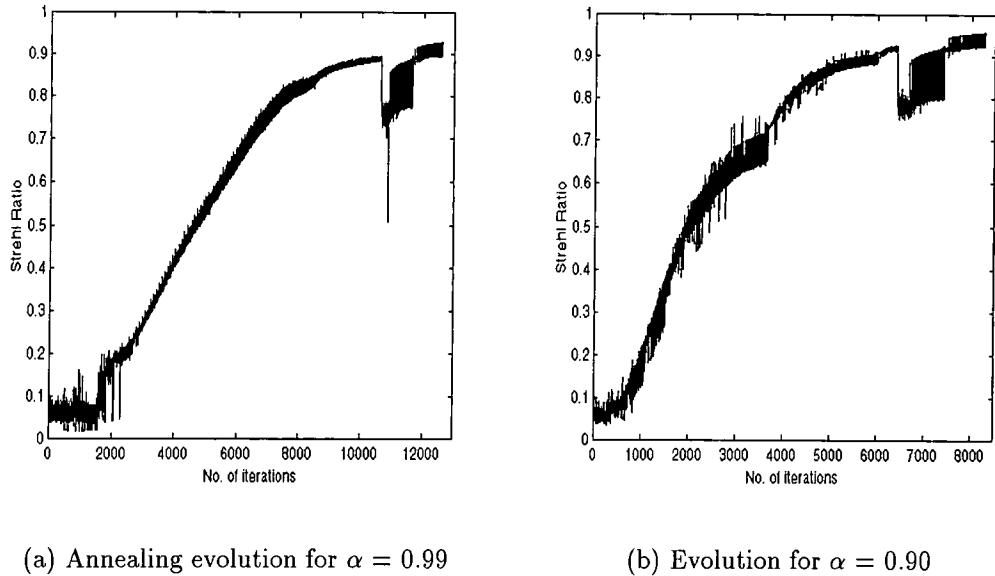
Figure 6.20: Evolutions of the simulated algorithm for a rapid quench. Nudges are visible at approximately 11000 and 6200 iterations respectively.

Tables 6.3, 6.4 and 6.5 show that as the system is quickly quenched i.e low values of α, the number of required iterations decreases. If the time spent at each temperature step increases then this still holds although as expected the relative number of iterations increases. For high values of α, the algorithm spends more time in a larger simplex space, the probability of a piston being racked through a distance comparable to half the wavelength is greater. For a rapid quench namely when iterations = 2 resulted in the lowest rms. mirror figures. Forcing the time spent at high values of T means that modulo λ may increase due to the larger simplex deformations.

α	SR - pre-nudge	SR - post-nudge	Final Rms. error	No. of iterations
0.99	0.89	0.93	0.062 *	12617
0.95	0.93	0.96	0.058 *	8298
0.9	0.94	0.96	0.082 *	8884
0.8	0.93	0.95	0.061 *	7433
0.6	0.94	0.97	0.078 *	6811

Table 6.3: Simulated annealing and the effect of quenching, 2 iterations per temperature decrease. (* denotes modulo λ piston error).

α	SR - pre-nudge	SR - post-nudge	Final Rms. error	No. of iterations
0.99	0.87	0.91	0.092 *	15962
0.95	0.94	0.97	0.058 *	8376
0.9	0.95	0.97	0.059 *	8517
0.8	0.94	0.97	0.056 *	7739
0.6	0.94	0.96	0.074 *	7914

Table 6.4: Simulated annealing with 10 iterations per temperature decrease.

α	SR - pre-nudge	SR - post-nudge	Final Rms. error	No. of iterations
0.99	0.86	0.90	0.126 *	21658
0.95	0.92	0.95	0.112 *	18758
0.9	0.89	0.96	0.115 *	14109
0.8	0.94	0.97	0.067 *	11221
0.6	0.94	0.97	0.113 *	7521

Table 6.5: Simulated annealing with 100 iterations per temperature decrease.

The effect of mirror alignment using a series of minimisations

It was found that a considerable system improvement could be achieved if the 76 segment mirror array was broken down into a series of minimisations. Each set of mirror elements could then be annealed into alignment, repeated application eventually phasing the whole mirror. Fig. 6.21 shows the arrangement used, the geometry of the mirror allowed for the formation of 5 concentric rings of mirror segments. Loops are indicated by segments of equal shading.
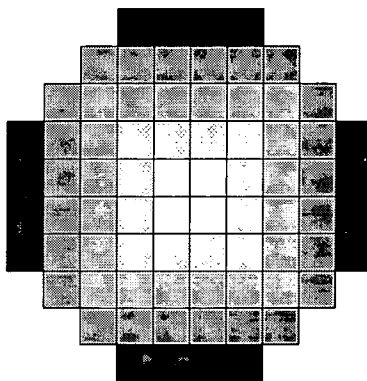
Figure 6.21: Loop arrangement used in the simulated annealing arrangement.

To minimise the mirror the following procedure was used:

- Calculate location of the peak intensity. For the simulation this is straight forward. In an experimental case, the centroid of the PSF could be used.

- Apply a tilt such that the segments do not contribute to the overall PSF. The mirror was divided in two and given opposite tilts - see Fig. 6.22 .

- For each loop remove the tilt, perturb and then minimise. Hold loop at the final algorithm output.

- Step through each loop, following procedure in previous line.

- Nudge and repeat whole procedure if necessary.

The tilt should be large enough to negate the contribution of any actual mirror tilts. For the simulation a global tilt of 0.1λ was applied. The form of the mirror and resultant PSF are shown in Fig. 6.22.
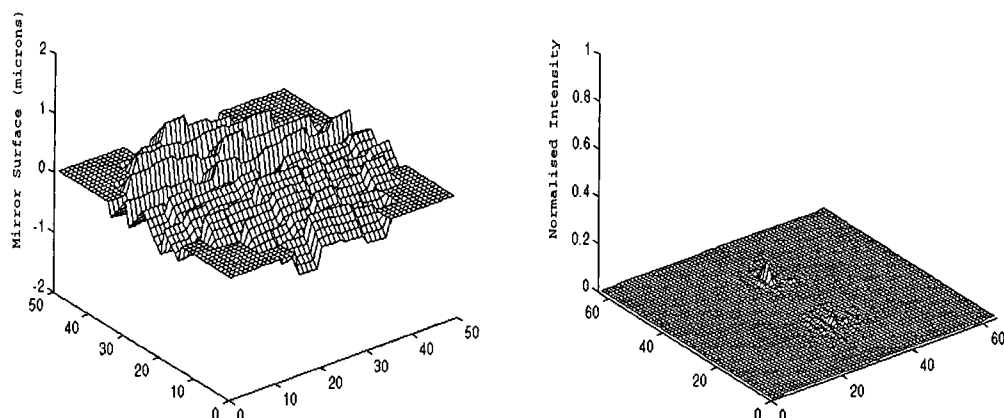
(a) Mirror surface with a segment tilt of 0.2λ

(b) Tilted PSFs, SR=0.02

Figure 6.22: The tilted mirror surface and far field intensity profile.

The SR at the centre of the pattern was used as the MF. Experimentally, any could be used but care needs to be taken not to include the contribution of the tipped PSFs. Using other metrics defined over a region of space would require that the active area has no contribution from the tilted PSFs. Another problem is that high values for the mirror tilt requires considerable work by the piezoelectric actuators and can result in appreciable hysteresis.

Fig. 6.23 shows a typical correction cycle and the values for the mirror and reflected rms. errors and the MF. As each loop is corrected the rms. and MF change accordingly. No nudge is performed.
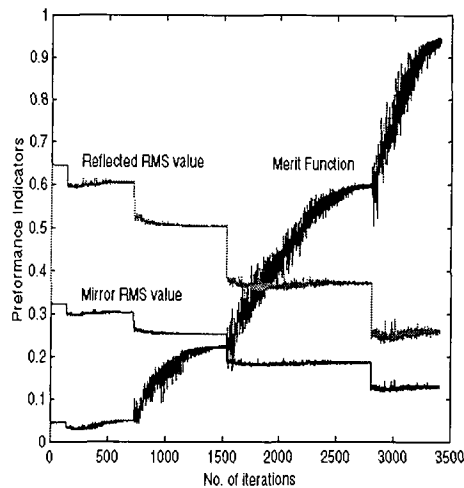
Figure 6.23: The MF, mirror and reflected rms. values for simulated annealing with loop correction.

As the segments in a loop are brought back the corresponding rms. values fall, the biggest being observed for loop 4 which has 24 segments. The final mirror state had several segments with modulo λ piston error.

The following Tables 6.6 and 6.7 show the final mirror states using the simulated annealing and simplex algorithms with the loop approach. Tables 6.6 and 6.7 should be compared to Table 6.2

Initial rms. error	Initial SR (intensity)	SR - pre-nudge	SR - post-nudge	Final rms. error	No. of iterations
0.053	0.892	0.986	0.987	0.016	3483
0.106	0.635	0.980	0.981	0.020	3769
0.142	0.447	0.969	0.977	0.022	3969
0.195	0.189	0.951	0.964	0.030	4429
0.258	0.071	0.935	0.950	0.118 *	5046
0.302	0.026	0.932	0.936	0.231 *	4839
0.337	0.008	0.919	0.921	0.276 *	5249

Table 6.6: The performance of simulated annealing with different input parameters under loop correction.

Running the same simulation with the simplex algorithm gave the results in Table 6.7.

Table 6.8 shows the mirror surface and PSF at various stages of the correction. The initial mirror has a SR of 0.19 with a corresponding reflected rms. error of 0.205λ.

Initial rms. error	Initial SR (intensity)	SR - pre-nudge	SR - post-nudge	Final rms. error	No. of iterations
0.053	0.892	0.987	0.987	0.017	2850
0.106	0.635	0.979	0.982	0.021	3111
0.142	0.447	0.969	0.976	0.024	3317
0.195	0.189	0.954	0.963	0.030	3753
0.258	0.071	0.940	0.950	0.060 *	4519
0.302	0.026	0.934	0.936	0.235 *	4569
0.337	0.008	0.919	0.919	0.275 *	4991

Table 6.7: Simplex correction with different input parameters under loop correction.

6.4.3 Results using Powell's method of conjugate directions

Powell's method is a more direct and faster approach for finding minima in multi-dimensional topologies. Whereas the simplex and simulated annealing routines assume no information about the system, Powell's method does and to some degree this explains the difference in their performance.

The actual algorithm utilised uses several subroutines in its operation. Apart from the actual Powell code, a program for bracketing the minimum along with another for the parabolic interpolation is required. The input to the routine needs several arrays and parameters. The initial starting point is composed of the mirror tip/tilt and piston values and is saved as a column vector. Also required is an $N \times N$ array containing the initial set of directions. For this simulation nothing was assumed and the matrix was generated from a set of random numbers with a weighting towards piston error. As with previous search techniques a convergence criterion, FTOL was required.

Effect of the bracketing routine

When the program was initially run the MF values varied rapidly. The bracketing routine initially takes large steps so as not to waste computation time. All it works towards is finding the bracketing triplet, the size of the interval is not of prime importance. The parabolic interpolator will quickly converge to the minimum within this. The effect of the step size in shown in Fig. 6.24. The initial conditions gave a SR of 0.189 with a reflected rms. error of 0.205λ the correction being performed at 1 micron.

As can be observed, decreasing the bracketing step size has no effect on the system performance. Actually, fewer iterations are required by the parabolic

Table 6.8: The mirror surface and PSF at various stages through the loop correction under simulated annealing.

(a) Bracketing constant = 1.0   (b) Bracketing constant = 0.4
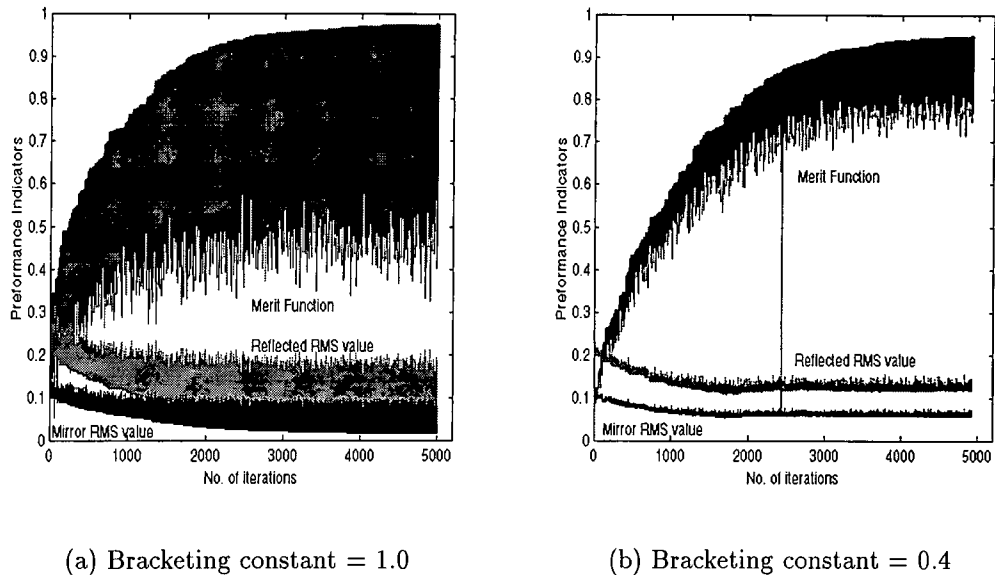
Figure 6.24: Effect of the size of the bracketing interval.

interpolation routine to perform the line minimisation with a large decrease in the system deformations.

In an experimental situation, there is an obvious gain in not moving the segments through huge distances. Fig. 6.24a shows an almost 40% swing in the SR value, something one would want to avoid. For the simulation the step size was kept less than $\lambda/2$. Another effect of large bracketing intervals is the promotion of modulo λ errors.

Performance with different MFs

The algorithm was then run with several metrics and the results are listed in Table 6.9. No nudge was used at this time. As can be seen the performance when using the bucket metrics is very poor. This is possibly due to the defocus effect of racking mirror segments through large distances. For the other metrics the final states are very similar and achieved with an equal numbers of iterations.

Nudging after the first convergence

The system was nudged by taking the final mirror values as the starting point but small perturbations were added to the directions. As with the previous algorithms a larger improvement was observed for higher, initial mirror misalignments. Typical evolution is shown in Fig. 6.25, the size is exaggerated for clarity. The SR

Merit Function	Final rms. error	Final SR	No. of Iterations
SR (centre)	0.118	0.950	4934
SR (anywhere)	0.119	0.951	4965
Bucket - 3 x 3	0.236	0.788	4984
" " - 5 x 5	0.210	0.696	3571
" " - 7 x 7	0.200	0.480	2477
I^2	0.118	0.954	4970
I^3	0.117	0.957	4986
I^4	0.117	0.945	5003
-I ln(I)	0.260	0.714	3571

Table 6.9: Performance of Powell's routine with different metrics. Initial rms. = 0.205λ, SR = 0.189.

rose from 95% to 96% for an initial mirror rms. of 0.10.
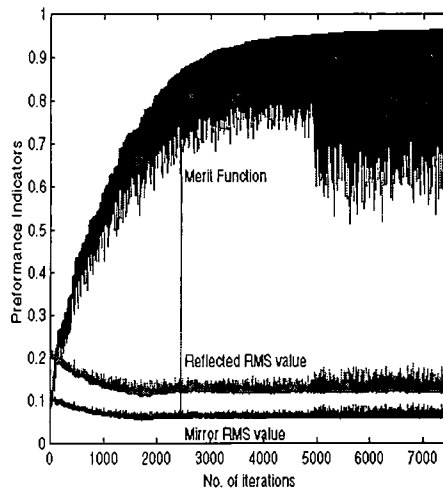
Figure 6.25: The effect of a nudge when used with Powell's routine.

Comparison to the simplex and simulated annealing routines

Finally the routine was run with varying initial conditions to compare the performance to the other algorithms. The full ELECTRA mirror was used without the loop correction described in Section 6.4.2. Table 6.10 contrasts the 3 search strategies described in this chapter.

The loop arrangement offered a slight improvement typically a reduction in the number of iterations by about 5% but nothing as dramatic as that seen with the simplex and annealing programs.

Initial	Initial	Powell		Simplex		Simulated Annealing	
error	SR	SR	Iter.	SR	Iter.	SR	Iter.
0.053	0.892	0.993	2499	0.988	3755	0.978	4243
0.106	0.635	0.973	2675	0.981	4465	0.976	4786
0.142	0.447	0.952	3467	0.976	4910	0.980	5324
0.195	0.189	0.955	4934	0.971	5996	0.973	6213
0.258	0.071	0.935 *	5140	0.972 *	8243	0.918 *	8453
0.302	0.026	0.905 *	5238	0.923 *	8434	0.910 *	8765
0.343	0.008	0.890 *	5543	0.966 *	9567	0.900 *	9645

Table 6.10: Comparison of various search strategies. Simulated annealing was set to 10 iterations per temperature decrease, $\alpha = 0.9$.

6.5 Summary

This chapter has indicated the viability of using an image sharpening metric in conjunction with a search algorithm. Starting with system Strehl Ratios as low as 3%, final SRs in excess of 90% were regularly obtained within a reasonable number of iterations. All three algorithms achieved similar final results the difference being in the number of iterations required. Powell's method although requiring the least iterations had an execution time similar to that of the simplex and simulated annealing programs due to it's dependance on several subroutines.

When the simplex and simulated annealing programs were run as a series of minimsations considerable improvement was observed in the number of iterations required. This can be explained due to the fact that the correction of the first loop of segments forms a 'seed' which subsequent loop corrections lock onto. When this method was used in conjunction with Powell's method the effect was not as marked. Using a series of loop minimisations reduces the number of DoFs, in other words it tends towards one dimension which is implicit in the use of Powell.

In a real system, the segmented mirror is not continuous but has edges, the effects of which has not been discussed here. In addition noise has not been accounted for. Also the use of a monochromatic source means that the modulo λ piston error is a real problem. Ribak [89] proposes using a related set of wavelengths to overcome this problem. There is a more subtle effect to piston errors in that it affects the focusing properties of the system, how the algorithms cope with this is not entirely clear and this is discussed further in Chapter 8.

The next step was to incorporate these ideas into the experimental ELECTRA system and this is detailed in the next chapter.

Chapter 7

Experimental results of NCPE correction within ELECTRA

7.1 Introduction

This chapter details the experimental results of using an image sharpening system within ELECTRA. As mentioned in the previous chapter the ELECTRA system is incapable of correcting any aberrations in the path from the beamsplitter to the science camera. The use of an image sharpening metric not only corrects for NCPE but also for any misalignments before the beamsplitter.

7.2 Measurement of the ELECTRA NCPE

On one of the commissioning runs a measure of the NCPE was determined. Essentially, the process involved using the science camera as a wavefront sensor. The technique used is only applicable when using a segmented mirror. All but one of the mirror segments have a large tilt applied so that the light from those segments is not incident on the camera. The segments are then brought back in turn and the following procedure applied:

- The loop is closed and the position of the PSF at the science arm is measured with respect to a reference (usually the zero offset position for the first segment at the science camera).

- A calibration offset is then applied and the loop closed again and the position of the science arm PSF determined. This provides a calibration between the WFS and the science arm displacement. The displacement of the science arm PSF from the reference is converted to a WFS offset.

When all the segments have been cycled through they are then applied to the WFS calculations in real-time. The offset slope measurements are then fed to the piston reconstructor matrix as usual. The mirror will then adopt the conjugate form to any static aberration present.

From such an experiment it was shown that the main aberration present was in the form of astigmatism with a contribution from a trefoil or a very high order Zernike mode. The evolution was typically on the timescale of an hour.

7.3   Mirror flattening

In order to achieve good system performance the mirror needs to be initially flattened. In theory, an image metric and search algorithm could be used with the initial mirror and the mirror driven to a state conjugate to the system aberrations. A more efficient method is to use the interferometer to initially cophase the mirror and then apply image sharpening after this. Currently two schemes are used with ELECTRA, one uses a laser source to flatten to modulo λ and then a white light procedure to remove any piston errors.

- *Mirror flattening to modulo λ*

  This proceeds by moving all mirror segments through 4 quarter wavelength steps simultaneously each time recording the interferogram. Each pixel can then be treated as a '4-bucket' interferometry experiment. The tilt of a particular segment can then be determined by the rate of change of the phase across it and the piston from the mean phase. All the segments can then be adjusted until they all have zero tilt and the same piston (modulo 2π).

- *White light flattening*

  After the laser flat is generated, the white light flat is then used to overcome the piston errors. This is achieved by shearing the Shack-Hartmann array by half a segment both vertically and horizontally. The effect of this is to combine the light from two adjacent mirror segments. These mirrors are then scanned in piston to find the central maximum of the white light fringe. For example, segment A can be aligned with segment B, B is then reset and A aligned with segment C and so on. A set of equations is then built up which can then be solved in order to phase the whole mirror array.

Applying the image sharpening method after this has been performed results in a major reduction in the number of iterations required.

7.4 Experimental method

Next the various algorithms and metrics were tested on the actual ELECTRA apparatus, the typical arrangement used is shown in Fig. 6.3. The algorithms were tested using a mirror flattened to modulo λ using the Twyman-Green interferometer. Later, the white light source and its associated mirror flat were used.

Initially, the science camera was a Baxall CCTV V5214 camera which had high sensitivity in the infrared. When an algorithm was run with this camera in place the value of the MF fluctuated wildly. Using zonal correction with 76 individual mirror segments means that the contribution of one segment to the overall mirror PSF is very small and hence sensitivity is a problem. A general trend could be perceived in the MF evolution but the convergence was extremely slow and of no practical use.

To overcome this sensitivity limitation a SBIG camera [1] was introduced. The important camera parameters are listed in Table 7.1. One problem with this camera however, was that it required a parallel PC printer port for control. The previous Baxall camera could be run from the main control computer, a UNIX based Silicon Graphics (SGI) workstation and hence the control algorithms for the mirror and the camera could be incorporated into one C program. This was not possible when using the SBIG camera.

Camera Parameter	*Specification*
CCD	Texas Instruments TC255
Pixels	320 x 240 each being 10 μm square
Active area	3.2 x 2.4 mm
Read Noise	$25e^-$
Sensitivity	16 Bit @ 22kHz Pixel Rate
Shutter Speed	0.01 to 3600 seconds

Table 7.1: The SBIG camera specifications.

The SBIG camera was therefore interfaced to a DELL Latitude 366MHz Pentium II laptop computer. What was needed was a way of getting the camera data from the laptop to the SGI workstation which controlled the mirror. To solve this problem it was decided to write a routine using the NCSA's DTM (*Data Transfer Mechanism*) program. This software allowed for the setting up of a 'client/server' facility between the SGI and the laptop. The DTM program had a bandwidth of approximately 200 kbits per second and the coding was written in C. The overall situation is summarised in the following diagram, Fig. 7.1.

---

[1]Santa Barbara Instrument Group, Suite 33, PO Box 50437, Santa Barbara, CA 93150, USA
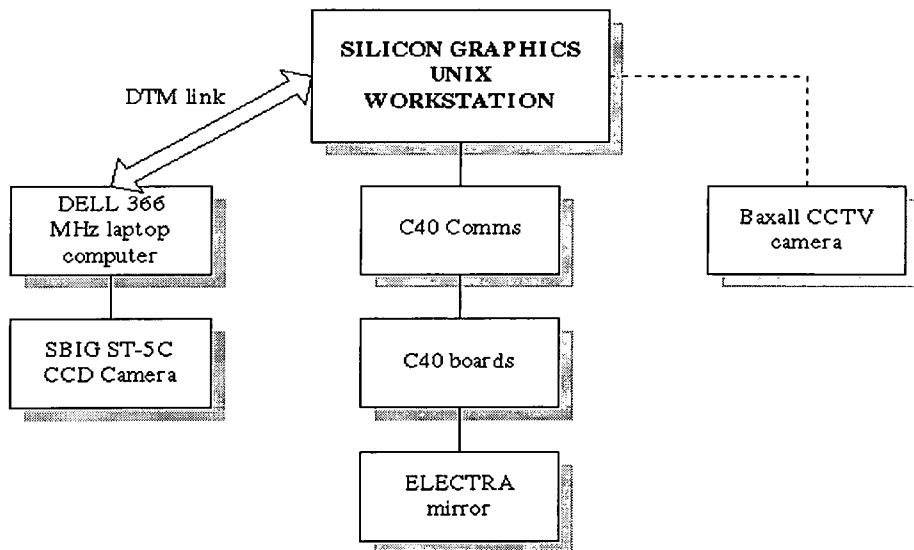
Figure 7.1: The computer interfacing arrangement, the Baxall camera could be linked directly to the SGI.

Although the camera had increased sensitivity the frame rate was slow, in the region of approximately 3Hz when the full minimisation program was run.

At first, the whole region of interest on the SBIG was transferred using the DTM program to the SGI and the frame processing carried out there i.e. the MF determination. In later work, a slight improvement in execution speed could be achieved by doing the MF determination etc. on the laptop and sending only the MF value.

7.5 ELECTRA results for NCPE correction

The following interferogram, Fig. 7.2 shows the mirror figure after the apparatus has been switched on and the He-Ne laser cavity length allowed to stabilize. As can be seen the segments all have different tip/tilts etc. The intensity given is the camera grey scale value. This has a full range of 0 to 32768, the 15 bit quantisation of the SBIG camera.

The results given are for monochromatic light at 633nm. The full frame of the PSF plot is 200 x 200 pixels corresponding to 1.2 by 1.2 arcseconds. Each pixel being equal to 0.006" on the sky.
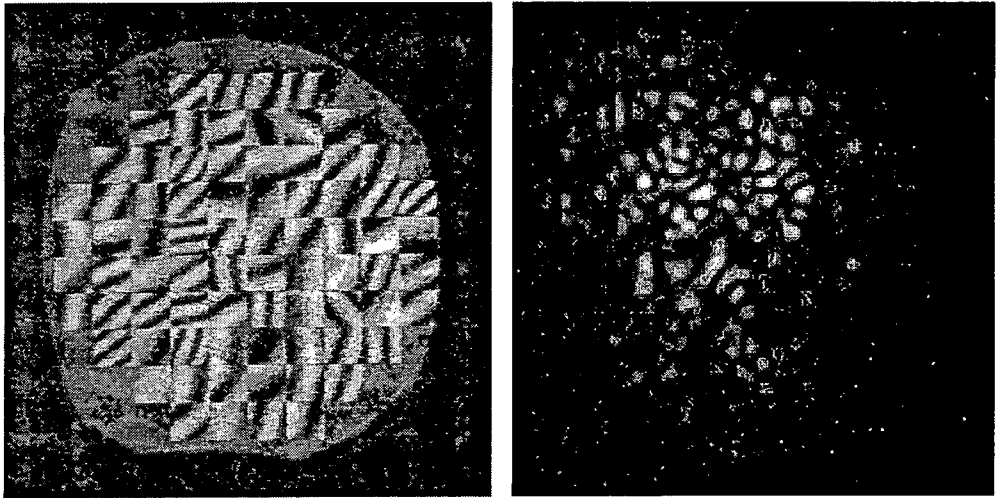
Figure 7.2: Initial interferogram and PSF. Max intensity of 1850.

7.5.1 Results with simplex correction

The first run started with the mirror initially flattened to modulo λ using the '4-bucket' flattening program. As the SBIG camera is relatively slow the frame size taken was reduced to 75 pixels square, the processing being performed on the laptop computer. The flux was adjusted by means of neutral density filters so that the maximum pixel intensity was approximately a third of the full range of the camera sensitivity. It was found that any value lower than this resulted in poorer algorithm performance. The shutter speed was set to 100 msec. The flattened mirror and PSF had the form shown in Fig. 7.3. The central 4 segments were blocked out at a low level in the software.

As can be observed the formation of the first Airy ring is just visible. The beam had to first pass through some liquid crystal optics installed for another experiment and this explains the other spot observable below the main one. Strictly speaking, when using this source there will be aberrations introduced due to these extra components. The use of the white light source did not have the LC optics in the optical path.

Due to the relatively short exposure time, the image tended to be rather noisy and hence using a function tolerance criterion for ending the simplex routine did not prove very useful. The algorithm did converge but tended to oscillate around the final solution and would not exit. This was of benefit, however, in gauging the number of iterations required. It was more favourable to set the algorithm going for a fixed number of iterations. Starting with a flat mirror approximately 1500 cycles proved to be sufficient, the whole minimisation process taking around
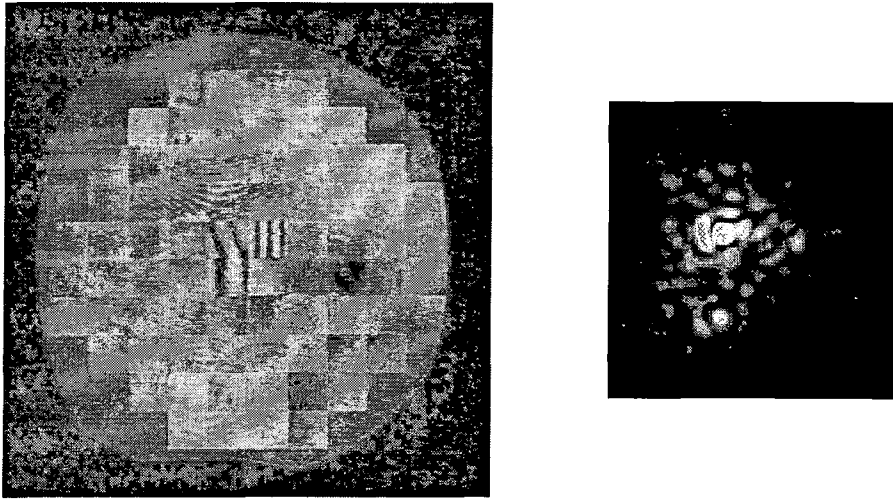
Figure 7.3: Interferogram and PSF when the mirror has been flattened. Maximum intensity of 9241. (PSF plot is 120 by 120 pixels).

8 minutes.

Various metrics were tried, although $S_1 = I_{max}$ was used in the first instance. The initial mirror perturbations were made predominantly piston and the cycle was run through once without nudging.

Results with a single iteration cycle

Fig. 7.4 shows the result for simplex correction under S_1, as can be observed the improvement is quite marked. The maximum intensity in the corrected image was 24106. The increase in clarity of the first diffraction ring can be seen.

The interferogram in Fig. 7.4 shows that the mirror figure has been modified from its initial, flat state to compensate for the system errors and the NCPE. The iteration cycle is shown in Fig. 7.5. The first 229 function evaluations are used in the generation of the initial simplex. After the program exits the simplex returns to the mirror configuration that gave the best MF. As the simplex program always remembers the best vertex this may not be the last configuration tried.

This first run showed the importance of the initial simplex generation. If the tip/tilt and piston coefficients were made equal then the system would only correct itself back to the state shown in Fig. 7.3. In order to proceed further and compensate for the system aberrations a higher weighting for the piston coefficient was required. Only then would an improvement be observed.
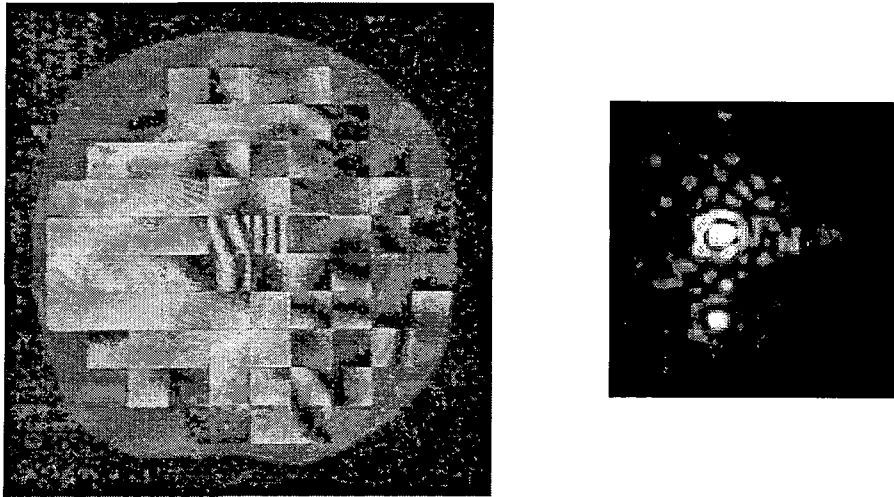
Figure 7.4: Corrected interferogram and PSF. Maximum intensity of 24106.
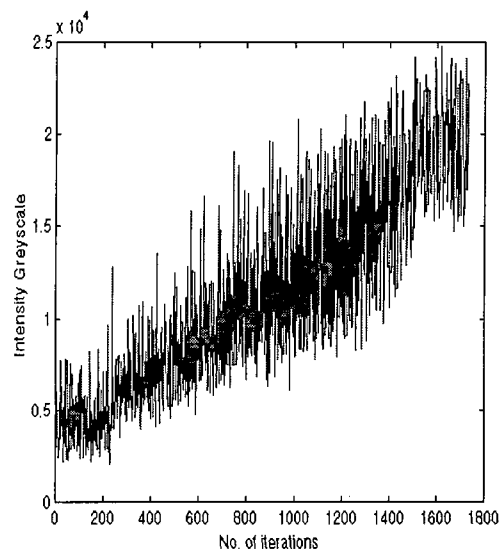
Figure 7.5: Evolution of the correction cycle. The process was terminated after 1500 function evaluations.

Fig. 7.6 shows the three dimensional plots of the PSFs shown in Figs. 7.3 and 7.4. They are drawn to the same scale for easier comparison. As can be seen that along with the increase in the peak intensity there is a loss in the peripheral structure. There is a slight improvement in the FWHM.

Performance with other merit functions

When run with other MFs the final state was not quite so good although the improvement was at least a doubling in the peak intensity. All required a similar
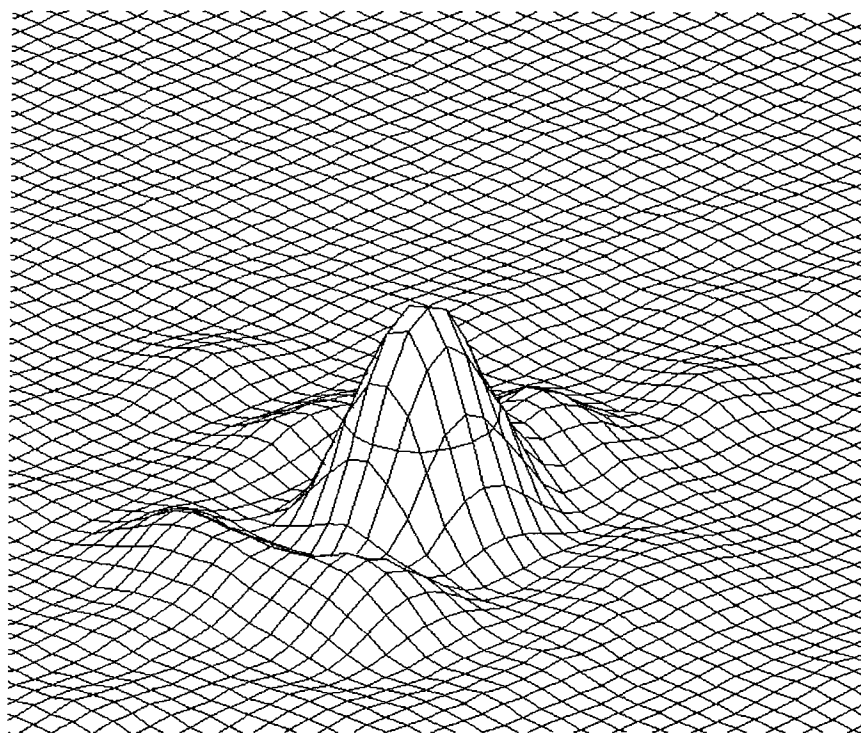
(a) PSF for the laser source through the AO system and LC optics
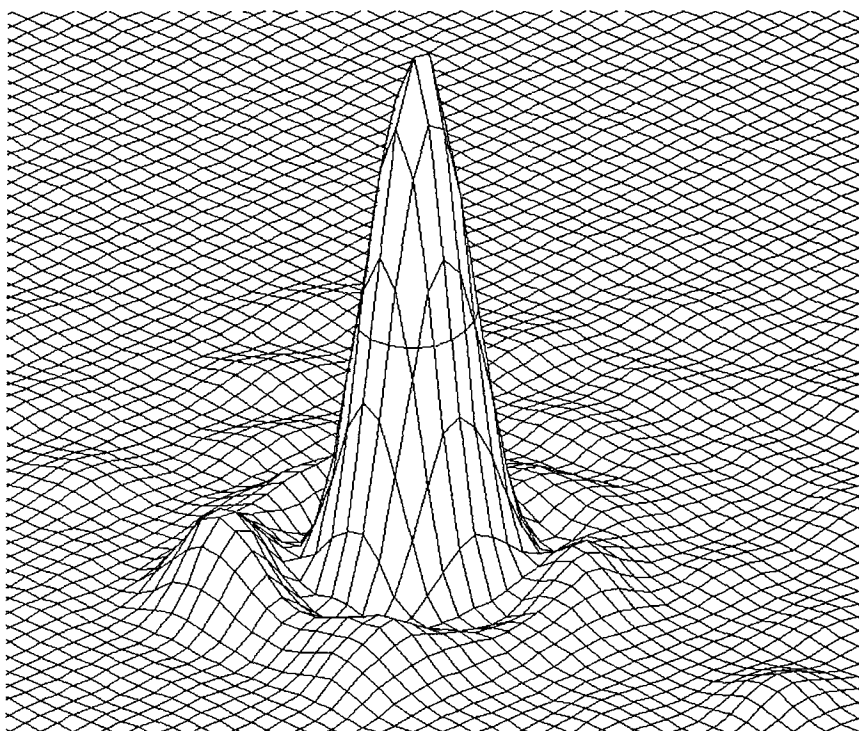
(b) Result after simplex correction. FWHM 0.048"x0.042"

Figure 7.6: The improvement in the PSF is clearly visible when comparing the above images. The formation of the first diffraction ring is apparent. The process was terminated after 1500 iterations.

number of iterations. Fig. 7.7 shows the final form of the PSF for the metric S_4, $n = 2$, the overall PSF is not quite as good as in Fig. 7.5 but the improvement is still marked. Note: the intensity scale on the diagrams was set by the maximum intensity in that particular frame so the diagrams are not directly comparable.

(a) PSF   (b) Merit function   (c) Intensity profile
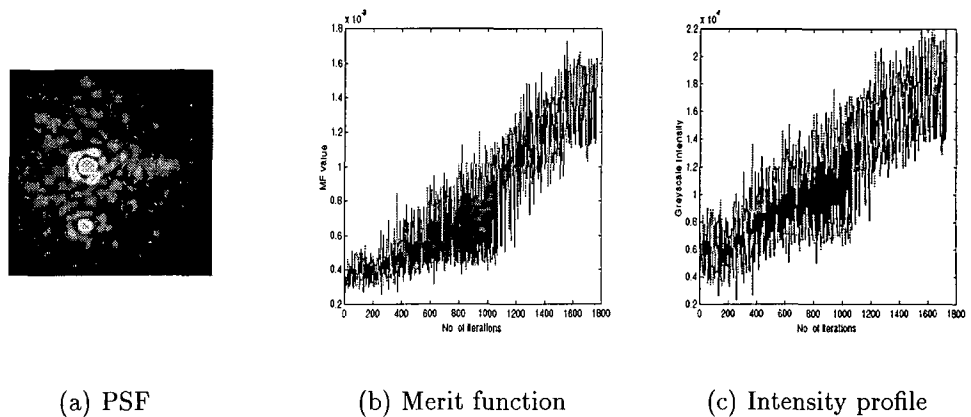
Figure 7.7: Results for $S_4 = I^n, n = 2$. Maximum intensity of 21147.

Similarly, the result for $S_4, n = 3$ is shown in Fig. 7.8.

(a) PSF   (b) Merit Function   (c) Intensity profile
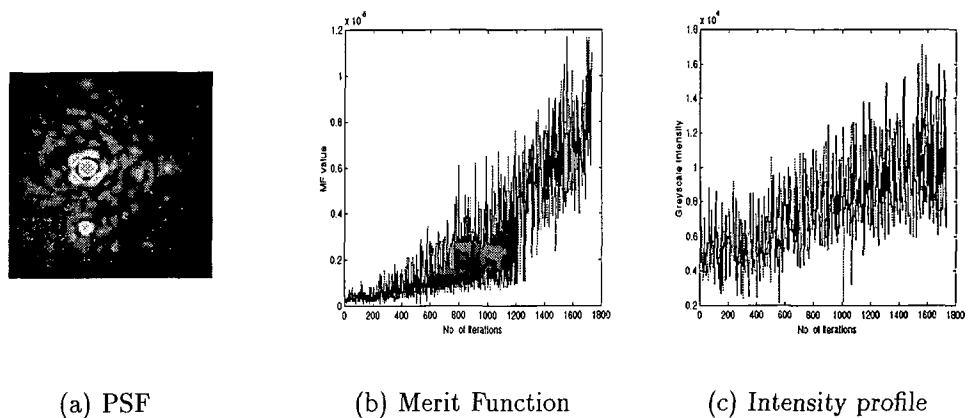
Figure 7.8: Result for $S_4, n = 3$. Maximum intensity of 19916.

The metric S_6 (with a 5 by 5 bucket) did not require the full 1500 function evaluations but met the convergence criterion early and exited after approximately 1300 iterations. The final figure, Fig. 7.9 is not as good as with the previous merit functions, with the maximum intensity being just under 16000.

(a) PSF   (b) Merit function   (c) Intensity profile
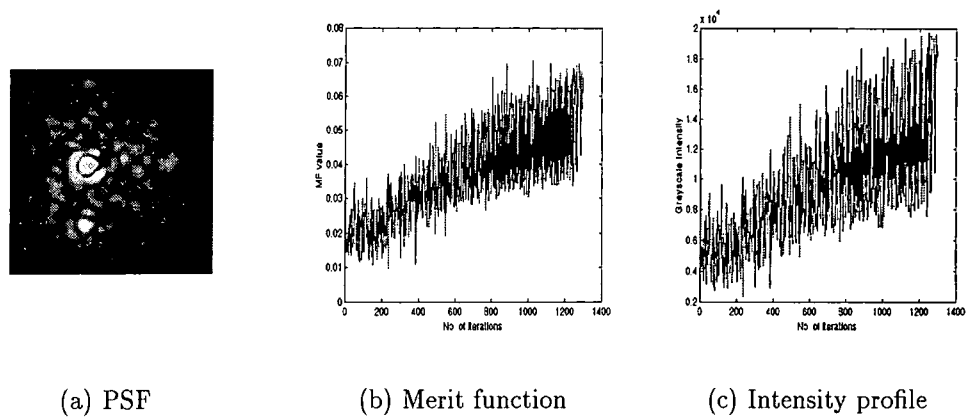
Figure 7.9: Result for S_6. The process exited after meeting the FTOL criterion. Peak intensity of 15788.

The effect of 'nudging' the simplex after the first cycle

The next aspect to look at was to see if there was a further improvement using a nudge after the initial convergence. Other features to examine were varying the weighting of the piston and the tip/tilt perturbations. The results given here are for a different experimental session to that described previously.

The metric $S_4, n = 2$ was used as this generally proved to be most stable when using short exposure times although better results were occasionally achieved with S_1. The initial PSF from a flattened mirror had a peak intensity of 10686. Running the program for 2000 iterations without nudging gave a final PSF with a peak intensity of 17178.

Table 7.2 shows the performance of the system when a nudge is included. The program was allowed 1500 iterations of the first cycle followed by another 500 after the nudge. The generation of the initial simplex was biased towards either piston or tip/tilt correction by appropriate weighting of the respective coefficients. These differed by a factor of 5.

Final state before nudge				*Final state after nudge*			
Relative weighting		*Iter.*	*Max.*	*Relative weighting*		*Iter.*	*Max.*
Piston	*Tip/tilt*		*Intensity*	*Piston*	*Tip/tilt*		*Intensity*
5	1	1500	17898	5	1	500	18687
5	1	1500	18219	1	5	500	20860
1	5	1500	10956	1	5	500	11154
1	5	1500	10736	5	1	500	14045
5	5	1500	14175	5	5	500	15683

Table 7.2: Effect of biasing the initial simplex.

As can be observed, the importance of the initial simplex generation has been demonstrated. The best improvement was when the piston coefficient was made larger before the nudge. Piston will have the greatest effect on the form of the PSF and concentrating on this first produces the best improvement, this then allows the algorithm to focus on the tip/tilt post-nudge.

Use of a white light source

The simplex algorithm was also tested under white light illumination. This is of more interest as the effect of system misalignments on starlight can then be estimated. Using the white light source meant that there was no contribution from the LC optics hence the improvement in the final form is purely due to aberration correction.

Typical initial and corrected images are shown in Fig. 7.10. The mirror was flattened using the white light source and the simplex program then run. Some alteration in the bias of the initial simplex was needed, namely a further increase in the piston coefficient. The flat had drifted somewhat before these frames were taken.
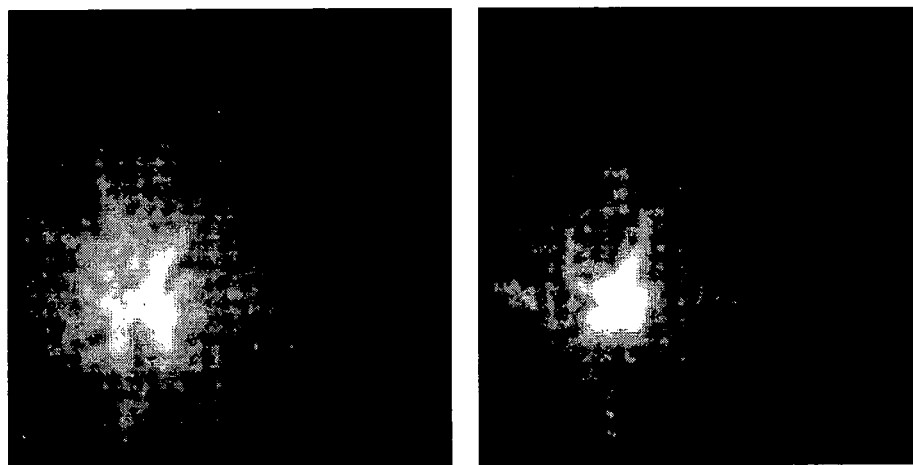
(a) Initial image. Max. int = 4551   (b) Corrected form Max. int = 13288

Figure 7.10: Results for white light correction using the simplex algorithm. NOTE: The intensity ranges of the images are different.

Fig. 7.11 shows how the structure of the PSF has been improved. The peak intensity has risen with a reduction in the FWHM and external structure around the central peak.
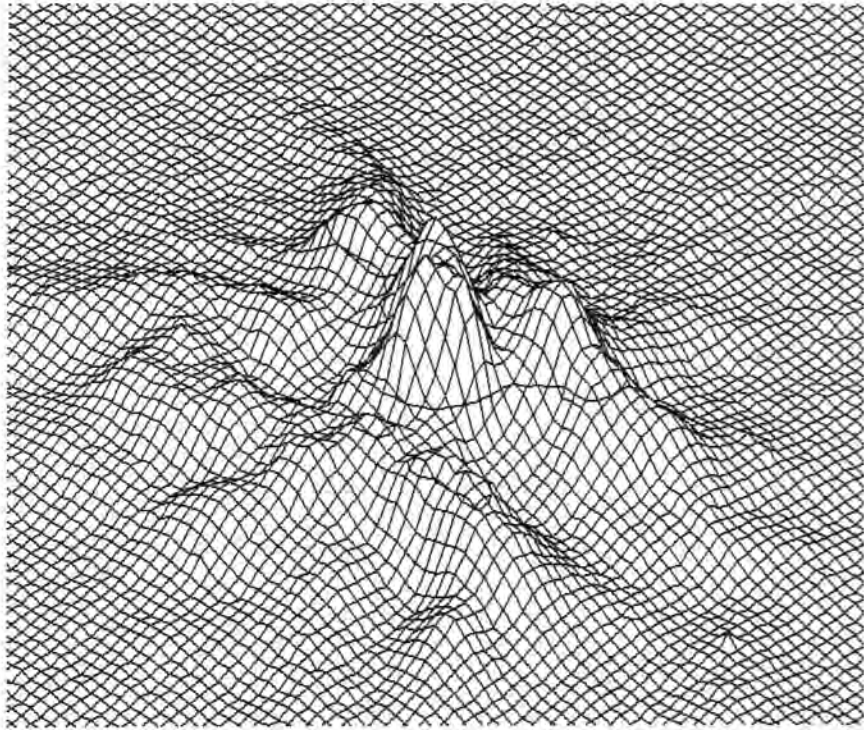
(a) PSF for the flattened mirror
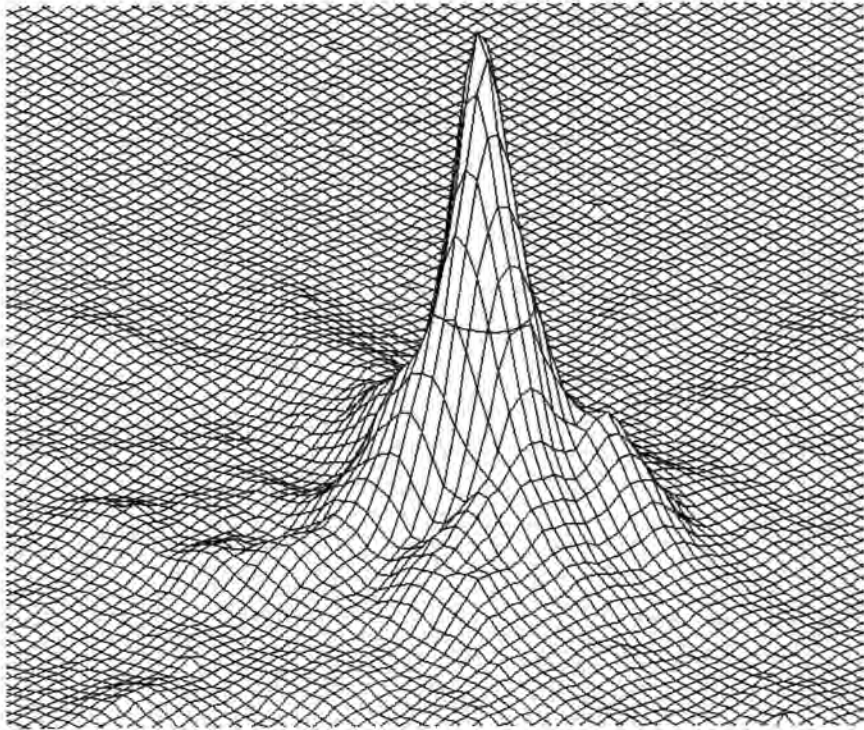
(b) Result after NCPE correction. FWHM 0.054"x 0.042"

Figure 7.11: The improvement in the PSF is clearly visible when comparing the above images. Much the the structure around the peak has been reduced. The process was terminated after 1500 iterations.

7.5.2 Results using simulated annealing

A similar set of experiments was performed using the simulated annealing algorithm in conjunction with a MF. The performance was comparable with that of the simplex case. Some of the optics were altered for the LC experiment which explains the difference in the PSF scales. The algorithm was tried using the annealing schedule detailed earlier with $\alpha = 0.9$. A rapid quench was run and then the time expanded at each temperature interval to include 10 and then 20 iterations. The metric used was S_4 with $n = 2$ as this proved to be the most reliable.

Results under laser illumination

The initial PSF had a peak intensity of 10342. The algorithm was allowed a of total 1500 iterations before the nudge and 500 subsequently. The starting temperature was found simply by trial and error. The results are shown in Figs. 7.12, 7.13 and 7.14. The PSF on the left of the figures is the one of interest, the other form is the reflection.

| (a) PSF | (b) Merit Function | (c) Intensity profile |
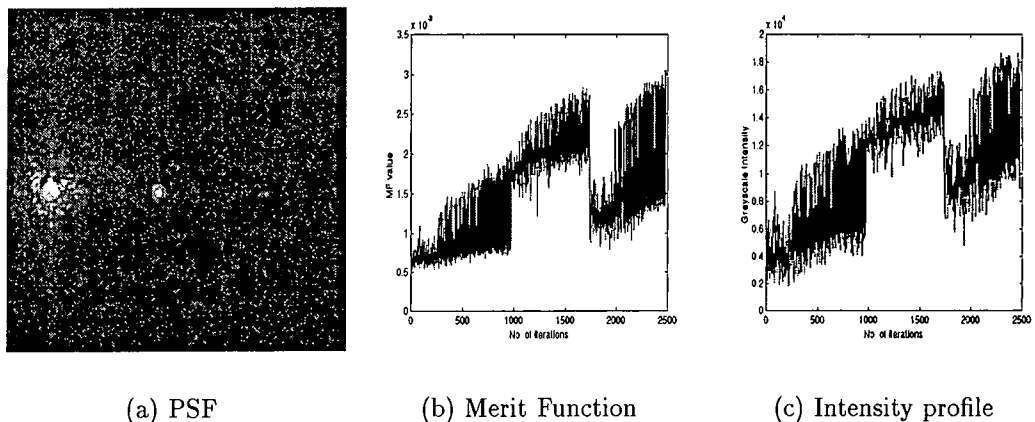
Figure 7.12: Simulated Annealing with Rapid Quench. Maximum intensity of 17834.

A slightly better improvement could be achieved by allowing 10 iterations per temperature decrease, Fig. 7.13.

(a) PSF   (b) Merit Function   (c) Intensity profile
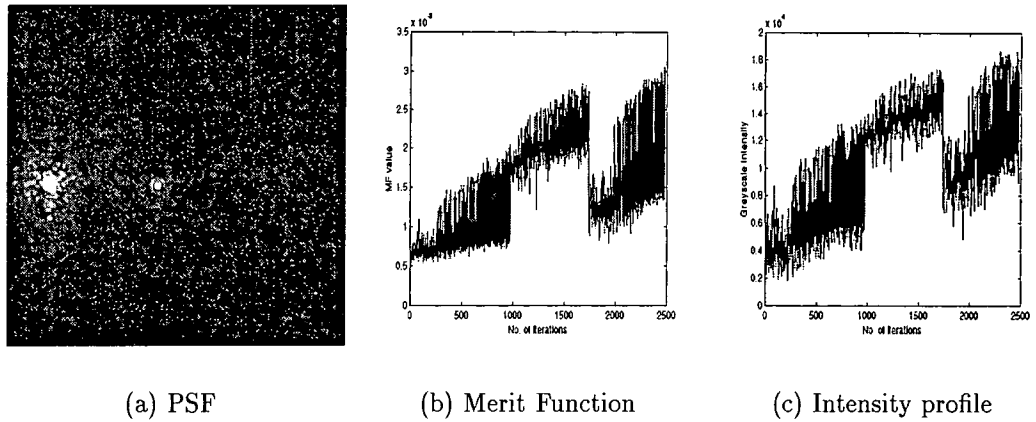
Figure 7.13: Simulated Annealing with 10 iterations per temperature decrease. Maximum intensity of 19290.

(a) PSF   (b) Merit Function   (c) Intensity profile
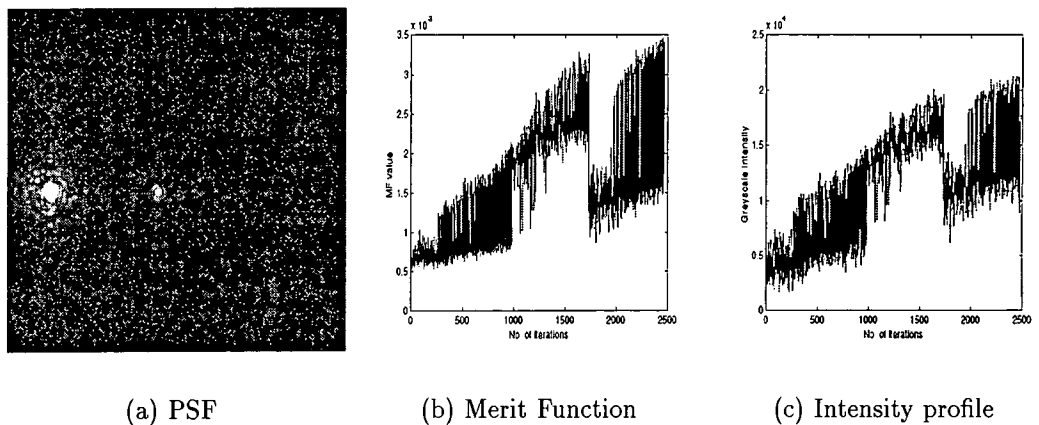
Figure 7.14: 20 iterations per decrease. Maximum intensity of 20935.

As can be seen the best results were achieved when the algorithm was allowed a longer time at each temperature. The rapid quench gave similar results to the simplex case when run under the same initial conditions.

Performance with a white light source

As with the downhill simplex the routine was run with a white light flat. The initial and final PSFs are shown in Fig. 7.15. 20 iterations were allowed per temperature. The improvement in the intensity of approximately 23% is comparable with that of the simplex result shown in Section 7.5.1.
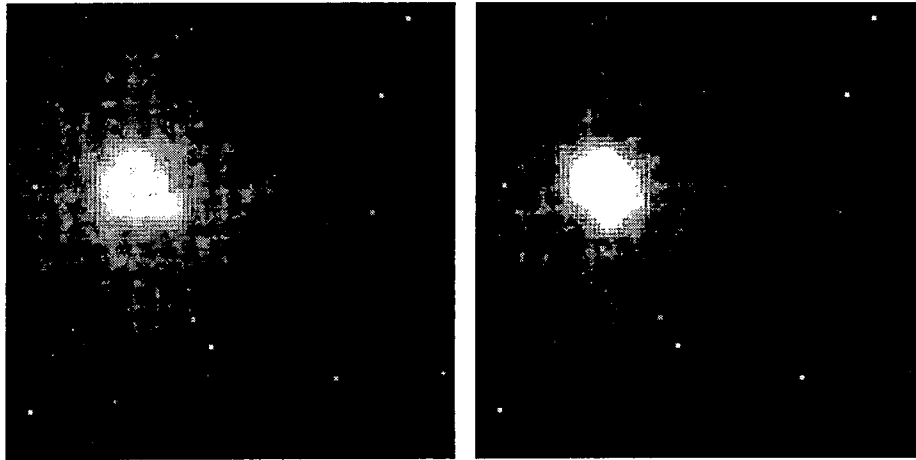
(a) Initial image. Maximum Intensity = 11181

(b) Corrected form. Maximum Intensity = 13759

Figure 7.15: Results for white light correction using simulated annealing.

The rise of the merit function and the intensity are shown in Fig. 7.16. The nudge is clearly visible around 2250 iterations. It was found that more iterations were required to improve the white light situation this is invariably due to piston issues.
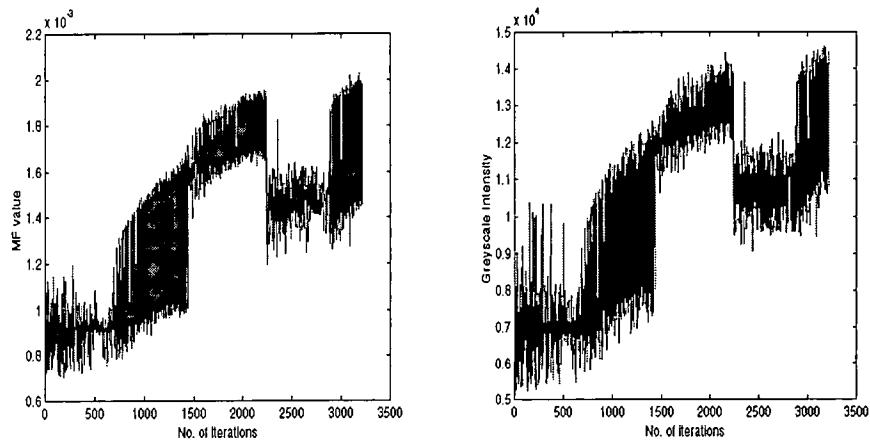
(a) Evolution of the MF, $S_4, n = 2$

(b) Variation in the Strehl Ratio

Figure 7.16: Evolution plots for simulated annealing.

7.6   Summary

The results have shown the need for some form of correction for system misalignments in ELECTRA. The benefit of such a method is that it does not require any extra optics which could themselves introduce further aberrations, simply the addition of a few programs to the system control software.

The limiting factor in the speed of operation was the slow frame rate of the SBIG CCD. Upon system installation at the William Hershel telescope this camera will be superseded by a camera having an increased bandwidth by a factor 3 to 4.

Improvement was shown for both laser and white light sources. With the laser source a regular doubling of the peak intensity was achieved, attributable to extra aberrations in the LC optics[2]. When the white light was used, peak intensity gains of the order of 20% were typically recorded. A slight adjustment was necessary for the white light, namely an increase in the piston perturbation. As mentioned previously the results for the white light are of more use and more indicative of the potential system improvement.

---

[2]The LC optics refers to external optics installed for another experiment not the Meadowlark LC-SLM as described in Chapter 5

Chapter 8

Summary and Conclusion

Image sharpening through the use of an image metric is a relatively neglected technique in the adaptive optics fraternity. This thesis has aimed to highlight the versatility and effectiveness of such a technique. This chapter summarises the results achieved and then discusses avenues of further work.

8.1 Summary

Chapter 2 gave a broad overview of the various means by which AO is implemented and listed on-line systems around the world. Chapter 3 detailed the relevant diffraction theory and discussed techniques of system correction in use. Chapter 4 was a brief foray into the vast field of optimisation theory.

Point and Extended Source Correction with the LC-SLM

The application of image sharpening to static aberration correction introduced by a glass plate was presented in Chapter 5. Zygo interferometer analysis of the plate showed only a significant contribution for the first 10 Zernike modes, the amplitudes of which were within the 1.1μm corrective range of the LC-SLM.

Diffraction limited imaging from uncorrected Strehl ratios in the 30% region were regularly achieved with a variety of image metrics. Some metrics such as

$$S_3 = \int |I(x,y) - I_0(x,y)|^n \, dx \, dy \quad \text{and} \quad S_5 = - \int I \ln I \, dx \, dy$$

were found to be unsuitable due the need for a corrected image or exhibited poor convergence.

The camera used at the time did not allow for zonal adjustment of the LC-SLM pixels. A slight improvement was seen of the order of 4% but this is well

below that achieved when a whole phase screen was written to the device.

When used with an extended object the full correcting range of the LC-SLM was exploited. The spatial frequency response of the correction was limited by the size of the LC pixels. Nevertheless analysis of the spatial frequency spectrum of the images showed that the full corrective bandwidth was being utilised.

A typical correction took on the order of 90 seconds mainly due to the need to average several frames to reduce noise. The calculation of the merit function was a small computational overhead in comparison. The rise time of the LC was not a factor.

The use of search algorithms

Various search strategies were then examined in Chapter 4 as a means of providing zonal correction for the 76 segment ELECTRA mirror. Without the additional problems induced by noise all the algorithms examined showed that mirror alignment giving in excess of the diffraction limit (taken to be the Rayleigh criterion, SR=80%) in the far field was achievable. The difference was in the number of iterations required. Although the Powell strategy at first glance appears the best in that it had quickest convergence, the overall execution time was comparable to that of the simplex and simulated annealing algorithms. Powell's routine required the use of several bracketing and one dimensional minimisation subroutines which collectively slowed the program execution. In comparison the simplex and simulated annealing algorithms are self contained programs consisting of 150 lines of C code. The use of median and loop minimisation reduced the iterations required to the extent that the iteration requirements of the simplex and simulated annealing approaches became comparable to that of Powell (with a full array minimisation).

Use within the ELECTRA system

Before this work was undertaken, the ELECTRA and the forthcoming NAOMI system would not have had any means of correcting NCPE. The need had been identified by the measurement technique described in Section 7.2 but no solution was proposed. Results have been presented for NCPE correction using both a white light and laser source which solves this problem.

The results with the white light source are of more interest than those with monochromatic light. Primarily due to the nature of starlight and secondly the lack of any extra optics. The result given for the annealing algorithm in Section 7.5.2 shows that peak intensity gains of 23% are obtainable. The result for the

simplex correction in Section 7.5.1 shows the effect of segment drift over the space of a few hours.

In practice it is envisaged that the white light flattening program would be available at the WHT so any algorithm would be used to complement this. With the increase in the frame rate of the new science camera, further iterations may be added into the system if required.

Both the simplex and simulated annealing algorithms have been written into the ELECTRA software in preparation for use at the telescope. The routines were also used for laboratory simulations of dual-conjugate generation of atmospheric turbulence with LC-SLMs [91].

8.2 Conclusion

The basic premise for this work has been to investigate alternative methods of AO correction with the emphasis on implementation and simplicity. Although image sharpening has been used on the ELECTRA apparatus other schemes would be equally applicable.

1. Science path aberration could be measured by another WFS , such as a Shack-Hartmann sensor mounted close to the camera. This would have the advantage that a quick diagnosis would be possible but would require extra optics and alignment. Bench space at the GHRIL platform is limited.

2. Phase Diversity. Application of this technique would provide an elegant solution but the problems would be the requirements to measure simultaneous images and provide the necessary computing power to find the right modal amplitudes.

With the ELECTRA system a possible improvement would be to write a modal correction to the mirror through the use of an image metric. This could correct the non-common path astigmatism. The form of the other aberrations is not known at this time but is thought to lie higher than Zernike mode 35. If so, an image sharpening correction could then be applied to compensate for this. The simulation and experiments did not have this initial knowledge and the worst case of knowing nothing about the system errors was assumed. The rationale being to test the algorithms performance without any insight.

Choice of Image Metric and Search Strategy

All the metrics tried with the exception of the two described in Section 8.1 had good convergence properties and provided an accurate indirect measure of the wavefront aberration (refer to Section 5.3.2). If image sharpening is going to be employed with an extended object imaging system then more elaborate metrics than those described in the thesis may require investigation. Image measure such as the MTF or associated power spectra may be a way forward.

The choice of which merit function to use with which search strategy was not critical. The only exception being the use of a bucket MF with Powell's algorithm. Powell's routine did induce large changes in the mirror states and this is further proved by the higher rms. errors due to modulo -λ piston issues. In general there was a variation in the number of iterations required but the final mirror state was not dependant on the metric.

To conclude: This thesis has proved that the use of an image metric in association with a search strategy can align systems with a huge number of degrees of freedom. When dealing with photon starved AO systems well aligned optics is a must and this technique has shown the room for system improvement. For lower order systems such as bimorph or membrane mirrors image sharpening may prove very attractive. The use of a DM to optimise light into an optical fibre, for example, could be easily implemented. Complex optical systems outside the field of AO could benefit from say the inclusion of a LC-SLM running under image sharpening control.

8.3 Future work

The following are suggestions for future work on wavefront correction using image metrics and search algorithms:

1. Optimization theory is constantly being developed. The thesis has not considered the use of genetic algorithms as a search technique. This involves using a series of sets of possible solutions to search the space. Each solution is then tested for it's 'fitness' by determining the merit function. The unsuitable solutions are not used again (they 'die') and the fittest solutions are combined and also randomly adapted ('mutated'). In this way, a search procedure mimics the process of evolution. Genetic algorithms have been use in the design of diffractive optical elements and achromatic doublets.

2. Search algorithms are extremely computer intensive. As computing powers increase, the methods described here will become suitable for slowly evolving turbulence. This thesis has only considered static or extremely slow turbulence.

3. This thesis has involved the use of simulation and experimental work. Further work in the theoretical analysis of image sharpening especially on the uniqueness of the optimum solutions would be useful.

Appendix A

The Meadowlark Hex-69 LC-SLM

The liquid crystal spatial light modulator used in Chapter 5 is manufactured by Meadowlark Optics of Colorado, USA. The device used in this thesis has 69 individually addressable pixels although a 127 pixel device is commercially available from the same company. The actual device is shown in Fig. A.1.

Figure A.1: The Meadowlark Hex-69 liquid crystal spatial light modulator.

The device uses a nematic liquid crystal which allows for continuous phase control with a write time of about 50 milliseconds. The device is easily controlled from the parallel printer port on a standard MS-DOS PC. Software was supplied by the manufacturer which allowed for individual pixel control. It was necessary for future work to develop code which allowed direct writing of Zernike modes. This was initially in the form of a standalone MS-DOS executable program and was eventually incorporated into the LabWindows environment.

The main drawback with LC-SLMs is their slow write time. Love [92] has shown that the bandwidths possible with nematic liquid crystals are approaching that needed for full astronomical AO compensation. A closed loop AO system

using a Meadowlark Hex69 has been demonstrated by Gourlay [93] although without the necessary bandwidth.

The active area is shown in Fig. A.2. The pixels are hexagonal in nature arranged in concentric circles around the centre.
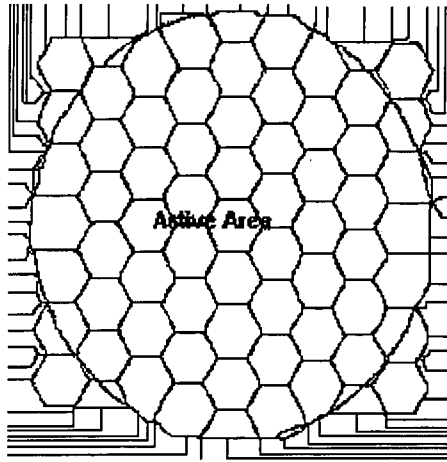
Figure A.2: The active area on the Hex69 showing the hexagonal pixels and the electrode structure.

The relevant device parameters are listed in the following Table A.1.

Parameter	Specification
Active area	14.7mm diameter
Pixel size	Hexagonal, max.dia 2.08mm^2
Interpixel spacing	20μm
Total stroke	1.1μm
Cell thickness	5.5μm
Birefringence	0.2
Bandwidth	20Hz
Transmittance	90% (without polarisers)

Table A.1: Technical specifications of the Hex69 LC-SLM.

For phase modulation, a polariser is necessary, orientated with its transmission axis vertical, the Hex69 being mounted using the post shown in Fig. A.1. The beam was such that it filled the full aperture of the active area thus the wavefront control was maximised. Fig. A.3 shows the pixel phase maps for the first 15 Zernike modes. Experimental maps in the left column and theoretical profiles on the right.
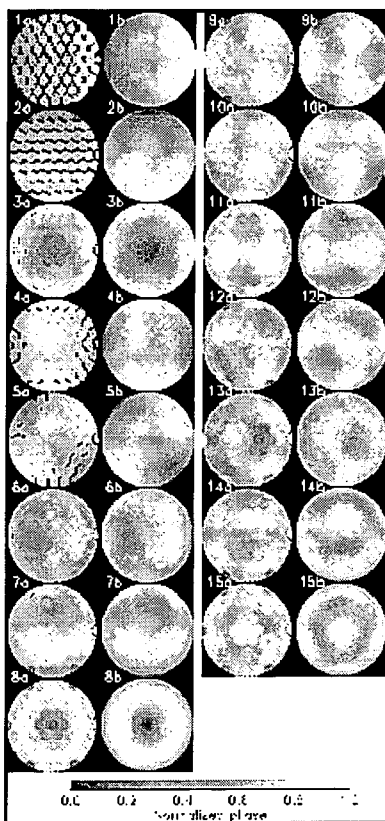
Figure A.3: Zernike mode generation using the Hex69. Photograph courtesy of G Love, University of Durham.

Bibliography

[1] K. J. Dodson, G. V. Mehle, and E. P. Kasl. Recent developments in hybrid mirror technology for the next generation space telescope. In *ICO XVIII - Optics for the Next Millenium*, San Francisco, August 1999. SPIE.

[2] J. H. Burge. Ultra-lightweight, actively controlled mirrors for space. In *ICO XVIII - Optics for the Next Millenium*, San Francisco, August 1999. SPIE.

[3] H. W. Babcock. *Publ. Astron. Soc. Pac*, 65(229), 1953.

[4] A. Labeyrie. Attainment of diffraction -limited resolution in large telescopes by fourier analysing speckle patterns in star images. *Astron. Astrophys*, 6, 1970.

[5] V. I. Tartarski. *Wave Propagation in a Turbulent Atmosphere*. Dover, New York, 1961.

[6] A. Kolmogorov. *Turbulence – Classic Papers in Statistical Theory*. Interscience Publishers Inc., New York, 1961.

[7] D. L. Fried. Statistics of a geometric representation of wavefront distortion. *J. Opt. Soc. Am.*, 55(11):1427, 1977.

[8] R. N. Wilson and L. Noethe. Closed-loop active optics - its advantages and limitations for correction of wind-buffet deformations of large flexible mirrors. In *Active Telescope Systems*, volume 1114. SPIE, 1989.

[9] R. K. Tyson. *Principles of Adaptive optics*. Academic Press, New York, 1991.

[10] R. K. Tyson. *Adaptive Optics Engineering Handbook*. marcel Dekker Inc, New York, 2000.

[11] J. Geary, M. Yoo, P. Davila, A. Wirth, A. Jankevics, M. Ruda, and R. Zielinski. Comparison of wavefront sensor techniques. *Proc. Soc. Photo-Opt. Inst. Eng (SPIE)*, 1762:58, 1992.

[12] J. W. Hardy. Active optics: A new technology for the control of light. *Proc. IEEE*, 66:651, 1978.

[13] J. D. Armitage and A. Lohmann. *Optica Acta*, 12(185):252, 1965.

[14] P. M. Birch, J. Gourlay, G. D. Love, and A. Purvis. Real-time optical aberration correction with a ferroelectric liquid-crystal spatial light modulator. *Appl. Optics*, 37(11):2164, 1998.

[15] R. N. Smartt. *Japan J. Appl. Phys*, 14(14), 1975.

[16] F. Roddier. Curvature sensing and compensation: a new concept in adaptive optics. *Appl. Opt.*, 27:1223, 1988.

[17] F. Roddier, C. Roddier, and N. Roddier. Curvature sensing: a new wavefront sensing technique. *Proc. Soc. Photo-Opt. Inst. Eng (SPIE)*, 976:203, 1988.

[18] Q. Gong and S. Hsu. Aberration measurement using axial intensity. *Opt. Eng*, 33(4):1176, 1994.

[19] W. Southwell. Wavefront analyser using a maximum likelihood algorithm. *J. Opt. Soc. Am.*, 67(3), 1977.

[20] S. Robinson. On the problem of phase from intensity measurements. *J. Opt. Soc. Am*, 68(1):87, 1978.

[21] R. A. Gonsalves. Phase retrieval and diversity in adaptive optics. *Optical Engineering*, 21(5):829, 1982.

[22] H. Takami, N. Takato, M. Otsubo, T. Kanzawa, Y. Kamata, K. Nakashima, and M. Iye. Adaptive optics system for cassegrain focus of subaru 8.2-m telescope. In *Adaptive Optical System Technologies*, volume 3353. SPIE, 1998.

[23] R. M. Myers, A. Longmore, R. Humpreys, G. Gilmore, B. Gentiles, M. Wells, and R. Wilson. The uk adaptive optics program. *Proc. Soc. Photo-Opt. Inst. Eng (SPIE)*, 2534:48, 1995.

[24] M. Lloyd-Hart, J. R. P. Angel, D. G. Sandler, T. K. Barrett, P. C. McGuire, T. A. Rhoadarmer, D. G. Bruns, S. M. Miller, D. W. McCarthy, and M. Cheselka. Infrared adaptive optics system for the 6.5-m mmt: system status and prototype results. In *Adaptive Optical System Technologies*, volume 3353. SPIE, 1998.

[25] J. W. Hardy. *Proc. Soc. Photo-Opt. Inst. Eng (SPIE)*, 332:252, 1982.

[26] D. S. Acton, P. L. Wiznowich, P. J. Stomski, J. C. Shelton, O. Lai, and J. M. Brase. Laboratory calibration of the w.m. keck observatory adaptive optics facility. *Proc. Soc. Photo-Opt. Inst. Eng (SPIE)*, 3353:125, 1998.

[27] L. K. Saddlemyer, G. Herriot, J. P. Veran, and J. M. Fletcher. Design aspects of the reconstructor for the gemini adaptive optics system (altair). In *Adaptive Optical System Technologies*, volume 3353. SPIE, 1998.

[28] G. Herriot, S. Morris, S. Roberts, J. M. Fletcher, L. K. Saddlemyer, G. Singh, J. P. Veran, and E. H. Richardson. Innovations in gemini adaptive optics system design. In *Adaptive Optical System Technologies*, volume 3353. SPIE, 1998.

[29] R. G. Dekany. The palomar adaptive optics system. *Top. Mtg on Adap. Opt. in Opt. Soc. Am. Tech. Dig. Series*, 13(40), 1996.

[30] G. Rousset, J. L. Beuzit, N. Hubin, E. Gendron, P. Y. Madec, C. Boyer, J. P. Gaffard, J. C. Richard, M. Vittot, P. Gigan, and P. J. Lena. Performance and results of the come-on+ adaptive optics system at the eso 3.6-m telescope. In *Adaptive Optics in Astronomy*, volume 2201. SPIE, 1994.

[31] D. Bonaccini, F. J. Rigaut, A. Glindemann, G. Dudziak, J. M. Mariotti, and F. Paresce. Adaptive optics for eso vlt interferometer. In *Adaptive Optical System Technologies*, volume 3353. SPIE, 1998.

[32] J. E. Graves, M. J. Northcott, F. J. Roddier, C. A. Roddier, and L. M. Close. First light for hokupa'a: 36-element curvature ao system at uh. *Proc. Soc. Photo-Opt. Inst. Eng (SPIE)*, 3353:34, 1998.

[33] R. Fugate, D. L. Fried, G. A. Ameer, B. R. Boeke, and S. L. Browne. Measurement of atmospheric wavefront distortion using scattered light from a laser guide-star. *Nature*, 353:144, 1991.

[34] R. Fugate, J. M. Spinhirne, J. F. Moroney, B. R. Boeke, and R. A. Cleis. In *Laser Guide Star Adaptive Optics Workshop*, Albuquerque - NM, 1992. SPIE.

[35] M. Kasper, D. Looze, S. Hippler, T. Herbst, A. Glindemann, T. Ott, and A. Wirth. Alfa: Adaptive optics for the calar alto observatory optics, control system, and performance. *Experimental Astronomy*, 10(1):49, 2000.

[36] H. D. Bissinger, S. S. Oliver, and C. E. Max. Conceptual design for a user-friendly adaptive optics system at the lick observatory. *Top. Mtg on Adap. Opt. in Opt. Soc. Am. Tech. Dig. Series*, 13(37), 1996.

[37] D. T. Gavel and H. W. Friedman. Measurements of the lick observatory sodium laser guide star. *Proc. Soc. Photo-Opt. Inst. Eng (SPIE)*, 3353:254, 1998.

[38] J. C. Shelton and S. L. Baliunas. Results of adaptive optics at mt. wilson observatory. In *Active and Adaptive Optical Components and Systems II*, volume 1920. SPIE, 1993.

[39] W. Jiang, N. Ling, G. Tang, M. Li, F. Shen, C. Rao, Y. Zhu, and B. Xu. 61-element adaptive optical system for 1.2-m telescope of yunnan observatory. In *Adaptive Optical System Technologies*, volume 3353. SPIE, 1998.

[40] N. Savage. Bigger, cheaper telescope starts use. Laser Focus World, Feb. 2000.

[41] G. A. Chanan, J. E. Nelson, and T. S. Mast. Segment alignment of the keck telescope primary mirror. In *Advanced Technology Optical Telescopes III*, volume 628. SPIE, 1986.

[42] C. Kuhne. Displacement-induced image degradation of a very large segmented mirror. *Astron. Astrophys*, 194:328, 1987.

[43] M. G. Lofdahl, R. L. Kendrick, A. Harwit, K. E. Mitchell, A. L. Duncan, J. H. Seldin, R. G. Paxman, and D. S. Acton. A phase diversity experiment to measure piston misalignment on the segmented primary mirror of the keck ii telescope. In *Space Telescopes and Instruments*, volume 3356. SPIE, 1998.

[44] J. M. Rodriguez-Ramos and J. J. Fuensalida. Piston detection of a segmented mirror telescope using a curvature sensor: Preliminary results with numerical simulations. *Proc. Soc. Photo-Opt. Inst. Eng (SPIE)*, 2871:613, 1997.

[45] F. Bortoletto, C. Bonoli, and D. Fantinel. An active telescope secondary mirror control system. *Rev. of Sci. Instrum.*, 70(6):2856, 1999.

[46] M. Born and E. Wolf. *Principles of Optics*. Pergammon Press, New York, 1959.

[47] J. W. Goodman. *Introduction to Fourier Optics*. McGraw-Hill, New York, 1968.

[48] H. Stark. *Applications of Optical Fourier Transforms*. Academic Press, London, 1982.

[49] R. C. Smith and J. S. Marsh. Diffraction patterns of simple apertures. *J. Opt. Soc. Am.*, 64(6):798, 1974.

[50] R J Noll. Zernike polynomials and atmospheric turbulence. *J. Opt. Soc. Am.*, 66(3):207, 1976.

[51] J. Y. Wang. Optical resolution through a turbulent medium with adaptive phase compensations. *J. Opt. Soc. Am.*, 67(3):383, 1977.

[52] L. C. Bradley and J. Herrmann. Phase compensation for thermal blooming. *Applied Optics*, 13(2):331, 1973.

[53] J. Y. Wang and D. E. Silva. Wavefront interpretation with zernike polynomials. *Applied Optics*, 19(9):1510, 1980.

[54] V. N. Mahajan. Zernike polynomials and optical aberrations. *Eng. & Lab. Notes in Opt. & Phot. News*, 6(2):8060, 1995.

[55] V. N. Mahajan. Zernike polynomials and optical aberrations of systems with circular pupils. *Eng. & Lab. Notes in Opt. & Phot. News*, 5(8):8121, 1995.

[56] R. A. Muller and A. Buffington. Real-time correction of atmospherically degraded telescope images through image sharpening. *J. Opt. Soc. Am.*, 64(9):1200, 1974.

[57] J. P. Hamaker, J. D. O'Sullivan, and J. E. Noordam. Image sharpness, fourier optics and redundant-spacing interferometry. *J. Opt. Soc. Am.*, 67(8):1122, 1977.

[58] A. Buffington, F. S. Crawford, R. A. Muller, A. J. Schwemin, and R. G. Smits. Correction of atmospheric distortion with an image-sharpening telescope. *J. Opt. Soc. Am.*, 67(3):298, 1977.

[59] A. Buffington, F. S. Crawford, R. A. Muller, and C. D. Orth. First observatory results with an image-sharpening telescope. *J. Opt. Soc. Am.*, 67(3):304, 1977.

[60] T. R. O'Meara. The multi-dither principle in adaptive optics. *J. Opt. Soc. Am.*, 67(3):306, 1977.

[61] M. A. Vorontsov, G. W. Carhart, D. V. Pruidze, J. C. Ricklin, and D. G. Voelz. Image quality criteria for an adaptive imaging system based on statistical analysis of the speckle field. *J. Opt. Soc. Am. A*, 13(7):1456, 1996.

[62] M. A. Vorontsov, G. W. Carhart, D. V. Pruidze, J. C. Ricklin, and D. G. Voelz. Adaptive imaging system for phase-distorted extended source and multiple-distance objects. *Appl. Opt.*, 36(15):3319, 1997.

[63] R. T. Brigantic, M. C. Roggemann, K. W. Bauer, and B. M. Welsh. Image-quality metrics for characterising adaptive optics system performance. *Appl. Opt.*, 36(26):6583, 1997.

[64] R. E. Jacobsen. An evaluation of image quality metrics. *J. of Photo. Sci.*, 43:7, 1995.

[65] R. E. Jacobsen. Image quality metrics. *J. of Photo. Sci.*, 43:42, 1995.

[66] M. C. Roggemann, C. A. Stoudt, and B. M. Walsh. Image-spectrum signal-to-noise improvements by statistical frame selection for adaptive-optics imaging through atmospheric turbulence. *Optical Engineering*, 33(10):3254, 1994.

[67] J. Pearl. *Heuristics - Intelligent Search Strategies for Computer Problem Solving.* Addison Wesley, London, 1985.

[68] M. J. Fryer and J. V. Greenman. *Optimisation Theory.* Edward Arnold, London, 1987.

[69] D. M. Greig. *Optimisation.* Longman Group, New York, 1980.

[70] J. A. Nelder and R. Mead. A simplex method for function minimisation. *Computer Journal*, 7:308, 1965.

[71] L. Arnold. Optimized axial support topologies for thin telescope mirrors. *Optical Engineering*, 34(2):567, 1995.

[72] N. C. Mehta. Remote alignment of adaptive optical systems with far-field optimization. In *Propagation of High-Energy Laser Beams Through the Earth's Atmosphere*, volume 1408. SPIE, 1991.

[73] N. Metropolis, A. W. Rosenbluth, M. N. Rosenbluth, and A. H. Teller. Equations of state calculations by fast computing machines. *Journal of Chemical Physics*, 21:1087, 1953.

[74] W. H. Press, S. A. Teukolsky, W. T. Vetterling, and B.P. Flannery. *Numerical Recipes in C: Second Edition.* Cambridge University Press, Cambridge, 1992.

[75] S. Kirkpatrick, C. D. Gelatt, and M. P. Vecchi. Optimisation by simulated annealing. *Science*, 20:671, 1983.

[76] N. B. Nill and B. H. Bouzas. Objective image quality measure derived from digital image power spectra. *Optical Engineering*, 31(4):813, 1991.

[77] R. M. Myers, A. P. Doel, C. N. Dunlop, J. V. Major, R. M. Sharples, and A. J. Vick. An astronomical ao system for use on a 4m-class telescope at optical wavelengths. In *Astronomical Interferometry*, volume 2201. Proc. SPIE, 1994.

[78] A. P. Doel, C. N. Dunlop, J. V. Major, R. M. Myers, and R. M. Sharples. Martini - system operation and astronomical performance. In *Active and adaptive optical systems*, volume 1542. Proc. SPIE, 1991.

[79] A. Doel, D. Buscher, C. Dunlop, R. Sharples, and N. Andrews. Topical meetings on adaptive optics. *ESO Conf. and Workshop Proc.*, 54:69, 1995.

[80] R. Haynes, A. P. Doel, R. Content, J. R. Allington-Smith, and D. Lee. Teifu: a thousand element integral field unit for the wht fed by the electra ao system. In *Optical Astronomical Interferometry*, volume 3355. Proc. SPIE, 1998.

[81] M. P. Chang and D. F. Buscher. Monomode fiber interferometer for single telescopes. In *Astronomical Interferometry*, volume 3350. Proc. SPIE, 1998.

[82] D. S. Acton. Correction of static optical errors in a segmented adaptive optical system. *Applied Optics*, 34(34):7965, 1995.

[83] E. E. Bloemhof and R. G. Dekany. Metrology for the adaptive optics system at the palomar 200" telescope. In *Infrared Astronomical Instrumentation*, volume 3353. Proc. SPIE, 1998.

[84] A. Zadrozny, M. P. J. L. Chang, D. F. Buscher, R. M. Myers, A. P. Doel, C. N. Dunlop, and R. M. Sharples. First atmospheric compensation with a linearised high order adaptive mirror - electra. *ESO/OSA Topical Meeting on Astronomy with Adaptive Optics Present Results and Future Programs*, 1998.

[85] G. A. Chanan, J. E. Nelson, and T. S. Mast. Segment alignment for the keck telescope primary mirror. In *Advanced Technology Optical telescopes III*, volume 628. Proc. SPIE, 1986.

[86] N. C. Mehta and C. W. Allen. Remote alignment of segmented mirrors with far-field optimization. *Applied Optics*, 31(30):6510, 1992.

[87] N. C. Mehta and C. W. Allen. Segmented mirror alignment with far-field optimization in the presence of atmospheric turbulence. *Applied Optics*, 32(15):2664, 1993.

[88] N. C. Mehta and C. W. Allen. Dynamic compensation of atmospheric turbulence with far-field optimization. *J. Opt. Soc. Am.*, 11(1):434, 1994.

[89] E. Ribak, J. Adler, and S. G. Lipson. Telescope phasing and ground states of solid-on-solid models. *J. Phys. A: Math. Gen.*, 23:809, 1990.

[90] R. I. Levin and N. A. J. Lieven. Dynamic finite element model updating using simulated annealing and genetic algorithms. *Mechanical Systems and Signal Processing*, 12(1):91, 1998.

[91] M. T. Kelly. to be unpublished.

[92] G. D. Love. Wavefront control using a high quality nematic liquid crystal spatial light modulator. *Proc. Soc. Photo-Opt. Inst. Eng (SPIE)*, 2566:43, 1995.

[93] J. Gourlay, G. D. Love, P. M. Birch, R. M. Sharples, and A. Purvis. A real-time closed-loop liquid crystal adaptive optics system: First results. *Optics Communications*, 137(1):17, 1997.